Observational Probes of Cosmic Acceleration

David H. Weinberg[a,b,c], Michael Mortonson[b], Daniel J. Eisenstein[d,e], Christopher Hirata[f], Adam Riess[g], Eduardo Rozo[h]

[a] *Department of Astronomy, Ohio State University, Columbus, OH 43210*
[b] *Center for Cosmology and Astro-Particle Physics, Ohio State University, Columbus, OH 43210*
[c] *Institute for Advanced Study, Princeton, NJ 08540*
[d] *Steward Observatory, University of Arizona, Tucson, AZ*
[e] *Harvard College Observatory, 60 Garden St., Cambridge, MA 02138*
[f] *California Institute of Technology, Pasadena, CA*
[g] *Department of Physics and Astronomy, Johns Hopkins University, Baltimore, MD 21218*
[h] *Kavli Institute for Cosmological Physics, University of Chicago, Chicago, IL 60637*

Abstract

This is a partial draft of a review article in preparation for *Physics Reports*, provided to members of the WFIRST Science Definition Team for reference. We have included only those sections that are close to complete. However, even these sections are still subject to change, so we request that this draft not be circulated beyond the SDT. We plan to solicit comments on the full manuscript before it is submitted to the journal.

Keywords:

1. Introduction

Gravity pulls. Newton's *Principia* generalized this longstanding fact of human experience into a universal attractive force, providing compelling explanations of an extraordinary range of terrestrial and celestial phenomena. Newtonian attraction weakens with distance, but it never vanishes, and it never changes sign. Einstein's theory of General Relativity (GR) reproduces Newtonian gravity in the limit of weak spacetime curvature and low velocities. For a homogeneous universe filled with matter or radiation, GR predicts that the cosmic expansion will slow down over time, in accord with Newtonian intuition. In the late 1990s, however, two independent studies of distant supernovae found that the expansion of the universe has accelerated over the last five billion years (Riess et al., 1998; Perlmutter et al., 1999), a remarkable discovery that is now buttressed by multiple lines of independent evidence. On the scale of the cosmos, gravity repels.

Cosmic acceleration is the most profound puzzle in contemporary physics. Even the least exotic explanations demand the existence of a pervasive new component of the universe with unusual physical properties that lead to repulsive gravity. Alternatively, acceleration could be a sign that GR itself breaks down on cosmological scales. Cosmic accleration may be the crucial empirical clue that leads to understanding the interaction between gravity and the quantum vacuum, or reveals the existence of extra spatial dimensions, or sheds light on the nature of quantum gravity itself.

Because of these profound implications, cosmic acceleration has inspired a wide range of ambitious experimental efforts, which aim to measure the expansion history and growth of structure in the cosmos with percent-level precision or higher. In this article, we review the observational methods that underlie these efforts, with particular attention to techniques that are likely to see major advances over the next decade. We will emphasize the value of a balanced program that

pursues several of these methods in combination, both to cross-check systematic uncertainties and to take advantge of complementary information.

The remainder of this introduction briefly recaps the history of cosmic acceleration and current theories for its origin, then sets this article in the context of future experimental efforts and other reviews of the field. Section 2 describes the basic observables that can be used to probe cosmic acceleration, relates them to the underlying equations that govern the expansion history and the growth of structure, and introduces some of the parameters commonly used to define "generic" cosmic acceleration models. It concludes with an overview of the leading methods for measuring these observables. In Sections 3-6, we go through the four most well developed methods in detail: Type Ia supernovae, baryon acoustic oscillations (BAO), weak gravitational lensing, and clusters of galaxies. Section 7 summarizes several other potential probes, whose prospects are currently more difficult to assess. Informed by the discussions in these sections, §8 presents our principal new results: forecasts of the constraints on cosmic acceleration models that could be achieved by combining results from these methods, based on ambitious but feasible experiments like the ones endorsed by the Astro2010 Decadal Survey report, *New Worlds, New Horizons in Astronomy and Astrophysics*. We summarize the implications of our analyses in §9.

1.1. History

Just two years after the completion of General Relativity, Einstein (1917) introduced the first modern cosmological model. With little observational guidance, Einstein assumed (correctly) that the universe is homogeneous on large scales, and he proposed a matter-filled space with finite, positively curved, 3-sphere geometry. He also assumed (incorrectly) that the universe is static. Finding these two assumptions to be incompatible, Einstein modified the GR field equation to include the infamous "cosmological term," now usually known as the "cosmological constant" and denoted Λ. In effect, he added a new component whose repulsive gravity could balance the attractive gravity of the matter (though he did not describe his modification in these terms). In the 1920s, Friedmann (**?**) and Lemaitre (**?**) introduced GR-based cosmological models with an expanding or contracting universe, some of them including a cosmological constant, others not. In 1929, Hubble discovered direct evidence for the expansion of the universe (Hubble, 1929), thus removing the original motivation for the Λ term. In 1965, the discovery and interpretation of the cosmic microwave background (Penzias and Wilson, 1965; Dicke et al., 1965) provided the pivotal evidence for a hot big bang origin of the cosmos.

From the 1930s through the 1980s, a cosmological constant seemed unnecessary to explaining cosmological observations. The "cosmological constant problem" as it was defined in the 1980s was a theoretical one: why was the gravitational impact of the quantum vacuum vanishingly small compared to the "naturally" expected value (see §1.2)? In the late 1980s and early 1990s, however, a variety of indirect evidence began to accumulate in favor of a cosmological constant. Studies of large scale galaxy clustering, interpreted in the framework of cold dark matter models with inflationary initial conditions, implied a low matter density parameter $\Omega_m = \rho_m/\rho_{\rm crit} \approx 0.15 - 0.4$ (e.g., Maddox et al. 1990; Efstathiou et al. 1990), in agreement with direct dynamical estimates that assumed galaxies to be fair tracers of the mass distribution. Reconciling this result with the standard inflationary cosmology prediction of a spatially flat universe (Guth, 1981) required a new energy component with density parameter $1 - \Omega_m$. Open-universe inflation models were also considered, but explaining the homogeneity of the cosmic microwave background (CMB) in such models required speculative appeals to quantum gravity effects (e.g., Bucher et al. 1995) rather than the semi-classical explanation of traditional inflation.

By the mid-1990s, many cosmological simulation studies included both open-CDM models and Λ-CDM models, along with $\Omega_m = 1$ models incorporating tilted inflationary spectra, non-standard

radiation components, or massive neutrino components (e.g., ?). Once normalized to the observed level of CMB anisotropies, the large-scale structure predictions of open and flat-Λ models differed at the tens-of-percent level, with flat models generally yielding a more natural fit to the observations (e.g., Cole et al. 1997). Thus, the combination of CMB data, large-scale structure data, and inflationary theory led many cosmologists to consider models with a cosmological constant, and some to declare it as the preferred solution (e.g., Efstathiou et al. 1990; Krauss and Turner 1995; Ostriker and Steinhardt 1995).

Enter the supernovae. In the mid-1990s, two teams set out to measure the cosmic deceleration rate, and thereby determine the matter density parameter Ω_m, by discovering and monitoring high-redshift, Type Ia supernovae. The recognition that the peak luminosity of supernovae was tightly correlated with the shape of the light curve (Phillips, 1993; Riess et al., 1996) played a critical role in this strategy, reducing the intrinsic distance error per supernova to $\sim 10\%$. While the first analysis of a small sample indicated deceleration (Perlmutter et al., 1997), by 1999 the two teams had converged on a remarkable result: when compared to local Type Ia supernovae, the supernovae at $z \approx 0.5$ were fainter than expected in a matter-dominated universe with $\Omega_m \approx 0.2$ by about 0.2 mag, or 20% (Riess et al., 1998; Perlmutter et al., 1999). Even an empty, freely expanding universe was inconsistent with the observations. Both teams interpreted their measurements as evidence for an accelerating universe with a cosmological constant, consistent with a flat universe ($\Omega_{\rm tot} = 1$) having $\Omega_\Lambda \approx 0.7$.

Why was the supernova evidence for cosmic acceleration accepted so quickly by the community at large? First, the internal checks carried out by the two teams, and the agreement of their conclusions despite independent observations and many differences of methodology, seemed to rule out many forms of observational systematics, even relatively subtle effects of photometric calibration or selection bias. Second, the ground had been well prepared by the CMB and large scale structure data, which already provided substantial indirect evidence for a cosmological constant. This confluence of arguments favored the cosmological interpretation of the results over astrophysical explanations such as evolution of the supernova population or grey dust extinction that increased towards higher redshifts. Third, the supernova results were followed within a year by the results of balloon-borne CMB experiments that mapped the first acoustic peak and measured its angular location, providing strong evidence for spatial flatness (de Bernardis et al. 2000; Hanany et al. 2000; see Netterfield et al. 1997 for earlier ground-based measurements hinting at the same result). On its own, the acoustic peak only implied $\Omega_{\rm tot} \approx 1$, not a non-zero Ω_Λ, but it dovetailed perfectly with the estimates of Ω_m and Ω_Λ from large scale structure and supernovae. Furthermore, the acoustic peak measurement implied that the alternative to Λ was not an open universe but a strongly decelerating, $\Omega_m = 1$ universe, which disagreed with the supernova data by 0.5 magnitudes, a level much harder to explain with observational or astrophysical effects. Finally, the combination of spatial flatness and improving measurements of the Hubble constant (e.g., $H_0 = 71 \pm 6$ km s^{-1} Mpc^{-1}; Mould et al. 2000) provided an entirely independent argument for an energetically dominant accelerating component: a matter-dominated universe with $\Omega_{\rm tot} = 1$ would have age $t_0 = (2/3)H_0^{-1} \approx 9.5$ Gyr, too young to accommodate the 12-14 Gyr ages estimated for globular clusters (e.g., Chaboyer 1998).

A decade later, the web of observational evidence for cosmic acceleration is intricate and robust. A wide range of observations, including larger and better calibrated supernova samples over a wider redshift range, high-precision CMB data down to small angular scales, the baryon acoustic scale in galaxy clustering, weak lensing measurements of dark matter clustering, the abundance of massive clusters in X-ray and optical surveys, the level of structure in the Lyα forest, and precise measurements of H_0, are all consistent with an inflationary cold dark matter model with a cosmological

constant, commonly abbreviated as ΛCDM.[1] Explaining all of these data simultaneously *requires* an accelerating universe. Completely eliminating any one class of constraints (e.g., supernovae, or CMB, or H_0) would not change this conclusion, nor would doubling the estimated systematic errors on all of them. The question is no longer *whether* the universe is accelerating, but *why*.

1.2. Theories of Cosmic Acceleration

A cosmological constant is the mathematically simplest solution to the cosmic acceleration puzzle. While Einstein introduced his cosmological term as a modification to the curvature side of the field equation, it is now more common to interpret Λ as a new energy component, constant in space and time. For an ideal fluid with energy density u and pressure p, the effective gravitational source term in GR is $(u + 3p)/c^2$, reducing to the usual mass density $\rho = u/c^2$ if the fluid is non-relativistic. For a component whose energy density remains constant as the universe expands, the first law of thermodynamics implies that when a comoving volume element in the universe expands by a (physical) amount dV, the corresponding change in energy is related to the pressure via $-pdV = dU = udV$, making the gravitational source term $-2u/c^2$. A form of energy that is constant in space and time must have a repulsive gravitational effect.

According to quantum field theory, "empty" space is filled with a sea of virtual particles. It would be reasonable to interpret the cosmological constant as the gravitational signature of this quantum vacuum energy, much as the Lamb shift is a signature of its electromagnetic effects.[2] The problem is one of magnitude. Since virtual particles of any allowable mass can come into existence for short periods of time, the "natural" value for the quantum vacuum density is one Planck Mass per cubic Planck Length. This density is about 120 orders of magnitude larger than the cosmological constant suggested by observations: it would drive accelerated expansion with a timescale of $t_{\rm Planck} \approx 10^{-43}$ sec instead of $t_{\rm Hubble} \approx 10^{18}$ sec. Since the only "natural" number close to 10^{-120} is zero, it was generally assumed (prior to 1990) that a correct calculation of the quantum vacuum energy would eventually show it to be zero, or at least suppressed by an extremely large exponential factor (see review by Weinberg 1989). But the discovery of cosmic acceleration raises the possibility that the quantum vacuum really does act as a cosmological constant, and that its energy scale is 10^{-3} eV rather than 10^{28} eV for reasons that we do not yet understand. To date, there are no compelling theoretical arguments that explain either why the fundamental quantum vacuum energy might have this magnitude *or* why it might be zero.

The other basic puzzle concerning a cosmological constant is: Why now? The ratio of a constant vacuum energy density to the matter density scales as $a^3(t)$, so it has changed by a factor of $\sim 10^{27}$ since big bang nucleosynthesis and by a factor $\sim 10^{42}$ since the electroweak symmetry breaking epoch, which seems (based on our current understanding of physics) like the last opportunity for a major rebalancing of matter and energy components. It therefore seems remarkably coincidental for the vacuum energy density and the matter energy density to have the same order of magnitude today. In the late 1970s, Robert Dicke used a similar line of reasoning to argue for a spatially flat universe (**?**), an argument that provided much of the initial motivation for inflationary theory (Guth, 1981). However, while the universe appears to be impressively close to spatial flatness, the existence of two energy components with different $a(t)$ scalings means that Dicke's "coincidence problem" is still with us.

One possible solution to the coincidence problem is anthropic: if the vacuum energy assumes widely different values in different regions of the universe, then conscious observers will find them-

[1] Many of the relevant observational references will appear in subsequent sections on specific topics.

[2] This interpretation of the cosmological constant was first suggested in the late 1960s by **?**; for further discussion of the history see Peebles and Ratra (2003).

selves in regions of the universe where the vacuum energy is low enough to allow structure formation (Efstathiou, 1995; Martel et al., 1998). This type of explanation finds a natural home in "multiverse" models of eternal inflation, where different histories of spontaneous symmetry breaking lead to different values of physical constants in each non-inflating "bubble" (Linde, 1987), and it has gained new prominence in the context of string theory, which predicts a "landscape" of vacua arising from different compactifications of spatial dimensions (Susskind, 2003). One can attempt to derive an expectation value of the observed cosmological constant from such arguments (e.g., Martel et al. 1998), but the results are sensitive to the choice of parameters that are allowed to vary (Tegmark and Rees, 1998) and to the choice of measure on parameter space, so it is hard to take such "predictions" beyond a qualitative level. A variant on these ideas is that the effective value (and perhaps even the sign) of the cosmological constant varies in time, and that structure will form and observers arise during periods when its magnitude is anomalously low compared to its natural (presumably Planck-level) energy scale (**?**Griest, 2002).

A straightforward alternative to a cosmological constant is a field with negative pressure (and thus repulsive gravitational effect) whose energy density changes with time (Ratra and Peebles, 1988). In particular, a canonical scalar field ϕ with potential $V(\phi)$ has energy density and pressure

$$\begin{aligned} u_\phi &= \tfrac{1}{2}\tfrac{1}{\hbar c^3}\dot{\phi}^2 + V(\phi), \\ p_\phi &= \tfrac{1}{2}\tfrac{1}{\hbar c^3}\dot{\phi}^2 - V(\phi), \end{aligned} \tag{1}$$

so if the kinetic term is subdominant, then $p_\phi \approx -u_\phi$. A slowly rolling scalar field of this sort is analogous to the inflaton field hypothesized to drive inflation, but at an energy scale many, many orders of magnitude lower. In general, a scalar field has an equation-of-state parameter

$$w \equiv \frac{p}{u} \tag{2}$$

that is greater than -1 and varies in time, while a true cosmological constant has $w = -1$ at all times. Some forms of $V(\phi)$ allow attractor or "tracker" solutions in which the late-time evolution of ϕ is insensitive to the initial conditions (Ratra and Peebles, 1988; Steinhardt et al., 1999), and some allow u_ϕ to track the matter energy density at early times, ameliorating the coincidence problem (Skordis and Albrecht, 2002). Some choices give a nearly constant w that is different from -1, while others have $w \approx -1$ as an asymptotic state at either early or late times, referred to respectively as "thawing" or "freezing" solutions (Caldwell and Linder, 2005).

Scalar field models in which the energy density is dominated by $V(\phi)$ are popularly known as "quintessence" (**?**). A number of variations have been proposed in which the energy density of the field is dominated by kinetic, spin, or oscillatory degrees of freedom (**?**). Other models introduce non-canonical kinetic terms or couple the field to dark matter. In general different models differ in the evolution of $u_\phi(a)$ and $w(a)$, and some have other distinctive features such as large scale energy density fluctuations that can affect CMB anisotropies or the integrated Sachs-Wolfe effect.

The alternative to introducing a new energy component is to modify General Relativity itself on cosmological scales, for example by replacing the Ricci scalar R in the gravitational action with some higher order function $f(R)$, or by allowing gravity to "leak" into an extra dimension in a way that reduces its attractive effect at large scales (Dvali et al., 2000). GR modifications can alter the relation between the expansion history and the growth of matter clustering, and, as discussed in subsequent sections, searching for mismatches between observational probes of expansion and observational probes of structure growth is one generic approach to seeking signatures of modified gravity. To be consistent with tight constraints from solar system tests, modifications of gravity must generally be "shielded" on small scales, by mechanisms such as the "chameleon" effect (**?**)

or "Vainshtein screening" (**?**). These mechanisms can have the effect of introducing intermediate scale forces. GR modifications can also alter the relation between non-relativistic matter clustering and gravitational lensing, which in standard GR are controlled by two different potentials that are equal to each other for fluids without anisotropic stress.

The distinction between a new energy component and a modification of gravity may be ambiguous. The most obvious ambiguous case is the cosmological constant itself, which can be placed on either the "curvature" side or the "stress-energy" side of the Einstein field equation. More generally, many theories with $f(R)$ modifications of the gravitational action can be written in a mathematically equivalent form of GR plus a scalar field with specified properties. Relative to expectations for a cosmological constant or a simple scalar field model, models in which dark matter decays into dark energy can produce a mismatch between the histories of expansion and structure growth while maintaining GR. Thus, even perfect measurements of all relevant observables may not uniquely locate the explanation of cosmic acceleration in the gravitational or stress-energy sector.

While the term "dark energy" seems to presuppose a stress-energy explanation, in practice it has become a generic term for referring to the cosmic acceleration phenomenon. In particular, the phrase "dark energy experiments" has come to mean observational studies aimed at measuring acceleration and uncovering its cause, regardless of whether that cause is a new energy field or a modification of gravity. We will generally adopt this common usage of "dark energy" in this review, though where the distinction matters we will try to use "cosmic acceleration" as our generic term. It is important to keep in mind that we presently have strong observational evidence for accelerated cosmic expansion but no compelling evidence that the cause of this acceleration is really a new energy component.

The magnitude and coincidence problems are challenges for any explanation of cosmic acceleration, whether a cosmological constant, a scalar field, or a modification of GR. The coincidence problem seems like an important clue for identifying a correct solution, and some models at least reduce its severity by coupling the matter and dark energy densities in some way. Multiverse models with anthropic selection arguably offer a solution to the coincidence problem, because if the probability distribution of vacuum energy densities rises swiftly towards high values, then structure may generically form at a time when the matter and vacuum energy density values are similar, in that small subset of universes where structure forms at all. But sometimes a coincidence is just a coincidence. Essentially all current theories of cosmic acceleration have one or more adjustable parameters whose value is tuned to give the observed level of acceleration, and none of them yield this level as a "natural" expectation unless they have built it in ahead of time. These theories are designed to explain acceleration itself rather than emerging from independent theoretical considerations or experimental constraints. Conversely, a theory that provided a compelling account of the observed magnitude of acceleration — like GR's successful explanation of the precession of Mercury — would quickly jump to the top of the list of cosmic acceleration models.

1.3. Looking Forward

The deep mystery and fundamental implications of cosmic acceleration have inpsired numerous ambitious observational efforts to measure its history and, it is hoped, reveal its origin. The report of the Dark Energy Task Force (DETF; Albrecht et al. 2006) played a critical role in systematizing the field, by categorizing experimental approaches and providing a quantitative framework to compare their capabilities. The DETF categorized then-ongoing experiments as "Stage II" (following the "Stage I" discovery experiments) and the next generation as "Stage III," and it looked forward to a generation of more capable (and more expensive) "Stage IV" efforts that might begin observations around the second half of the coming decade. The DETF focused on the same four methods that

will be the primary focus of this review: Type Ia supernovae, baryon acoustic oscillations (BAO), weak gravitational lensing, and clusters of galaxies.

Four years on, the main "Stage II" experiments have completed their observations though not necessarily their final analyses. Prominent examples include the supernova and weak lensing programs of the CFHT Legacy survey (**?**), the ESSENCE supernova survey (**?**), BAO measurements from the Sloan Digital Sky Survey (SDSS; Eisenstein et al. 2005; Reid et al. 2010a), and the SDSS-II supernova survey (Frieman et al., 2008b). These have been complemented by extensive multi-wavelength studies of local and high-redshift supernovae such as the Carnegie Supernova Project (Hamuy et al., 2006; Freedman et al., 2009), by systematic searches for $z > 1$ supernovae with *Hubble Space Telescope* (Riess et al., 2007), by dark energy constraints from the evolution of X-ray or optically selected clusters (Mantz et al., 2010; Vikhlinin et al., 2009; Rozo et al., 2010), by improved measurements of the Hubble constant (Riess et al., 2009), and by CMB data from the WMAP satellite (Bennett et al., 2003) and from ground-based experiments that probe smaller angular scales. Most data remain consistent with a spatially flat universe and a cosmological constant with $\Omega_\Lambda = 1 - \Omega_m \approx 0.75$, with an uncertainty in the equation-of-state parameter w that is roughly ± 0.1 at the $1 - 2\sigma$ level. Substantial further improvement will in many cases require reduction in systematic errors as well as increased statistical power from larger data sets.

The clearest examples of "Stage III" experiments, now in the late construction or early operations phase, are the Dark Energy Survey (DES), Pan-STARRS[3], the Baryon Oscillation Spectroscopic Survey (BOSS) of SDSS-III, and the Hobby-Eberly Telescope Dark Energy Experiment (HETDEX). All four projects are being carried out by international, multi-institutional collaborations. Pan-STARRS and DES will both carry out large area, multi-band imaging surveys that go a factor of ten or more deeper (in flux) than the SDSS imaging survey (Abazajian et al., 2009), using, respectively, a 1.4-Gigapixel camera on the 1.8-m PS1 telescope on Haleakala in Hawaii and a 0.5-Gigapixel camera on the 4-m Blanco telescope on Cerro Tololo in Chile. These imaging surveys will be used to measure structure growth via weak lensing, to identify galaxy clusters and calibrate their masses via weak lensing, and to measure BAO in galaxy angular clustering using photometric redshifts. Each project also plans to carry out monitoring surveys over smaller areas to discover and measure thousands of Type Ia supernovae. Fully exploiting BAO requires spectroscopic redshifts, and BOSS will carry out a nearly cosmic-variance limited survey (over 10^4 deg^2) out to $z \approx 0.7$ using a 1000-fiber spectrograph to measure redshifts of 1.5 million luminous galaxies, and a pioneering quasar survey that will measure BAO at $z \approx 2.5$ by using the Lyα forest along 150,000 quasar sightlines to trace the underlying matter distribution. HETDEX plans a BAO survey of 10^6 Lyα-emitting galaxies at $z \approx 3$.

There are many other ambitious observational efforts that do not fit so neatly into the definition of a "Stage III dark energy experiment" but will nonetheless play an important role in "Stage III" constraints. A predecessor to BOSS, the WiggleZ project on the Anglo-Australian 3.9-m telescope, is carrying out a spectroscopic survey of 240,000 emission line galaxies out to $z = 1.0$. The Hyper Suprime-Cam on the Subaru telescope will have wide-area imaging capabilities comparable to DES and Pan-STARRS, and it is likely to devote substantial fractions of its time to weak lensing surveys. Other examples include intensive spectroscopic and photometric monitoring of supernova samples aimed at calibration and understanding of systematics, new *HST* searches for $z > 1$ supernovae, further improvements in H_0 determination, deeper X-ray and weak lensing studies of samples of

[3]Pan-STARRS, the Panoramic Survey Telescope and Rapid Response System, is the acronym of the facility rather than the project, but cosmological surveys are among its major goals. Pan-STARRS eventually hopes to use four coordinated telescopes, but the surveys currently underway use the first of these telescopes, referred to as PS1.

tens or hundreds of galaxy clusters, and new cluster searches via the Sunyaev-Zel'dovich (Sunyaev and Zeldovich, 1970) effect using the South Pole Telescope (SPT) or Atacama Cosmology Telescope (ACT). In addition, Stage III analyses will draw on CMB constraints from the Planck satellite.

The Astro2010 report identifies cosmic acceleration as one of the most pressing questions in contemporary astrophysics, and its highest priority recommendations for new ground-based and space-based facilities both have cosmic acceleration as a primary science theme.[4] On the ground, the Large Synoptic Survey Telescope (LSST), a wide-field 8.4-m optical telescope equipped with a 3.2-Gigapixel camera, would enable deep weak lensing and optical cluster surveys over much of the sky, synoptic surveys that would detect and measure tens of thousands of supernovae, and photometric-redshift BAO surveys extending to $z \approx 3$. BigBOSS (**?**), highlighted as an initiative that could be supported by the proposed "mid-scale innovation program," would use a highly multiplexed fiber spectrograph on the NOAO 4-m telescopes to carry out spectroscopic surveys of $\sim 10^8$ galaxies to $z \approx 1.6$ and Lyα forest BAO measurements at $z > 2$. Another potential ground-based method for large volume BAO surveys is radio "intensity mapping," which seeks to trace the large scale distribution of neutral hydrogen without resolving the scale of individual galaxies. In the longer run, the Square Kilometer Array (SKA) could enable a BAO survey of $\sim 10^9$ HI-selected galaxies and weak lensing measurements of $\sim 10^{10}$ star-forming galaxies using radio continuum shapes.

Space observations offer two critical advantages for cosmic acceleration studies: stable high resolution imaging over large areas, and vastly higher sensitivity at near-IR wavelengths. (For cluster studies, space observations are also the only route to X-ray measurements.) These advantages inspired the Supernova Acceleration Probe (SNAP; **?**), initially designed with a concentration on supernova measurements at $0.1 < z < 1.7$, and later expanded to include a wide area weak lensing survey as a major component. Following the National Research Council's Quarks to Cosmos report (**?**), NASA and the U.S. Department of Energy embarked on plans for a Joint Dark Energy Mission (JDEM), which has considered a variety of mission architectures for space-based supernova, weak lensing, and BAO surveys. The Astro2010 report endorsed as its highest priority space mission a Wide-Field Infrared Space Telescope (WFIRST), which would carry out imaging and dispersive prism spectroscopy in the near-IR to support all three methods. The suggested design of WFIRST, a 1.5-m telescope with a large near-IR focal plane array, is like that of the JDEM-Omega proposal (Gehrels, 2010), but the endorsed mission scope is considerably broader, including a planetary microlensing program and a guest observer program. On the European side, ESA has selected the Euclid[5] satellite as one of three "definition phase" medium-class missions for its Cosmic Vision 2015-2025 program, with the expectation that two of the three missions will be selected for flight. Euclid would carry out optical and near-IR imaging and near-IR slitless spectroscopy over half the sky, for weak lensing and BAO measurements. Given the funding hurdles and the organizational and technical challenges that these projects face, it is not clear whether there will be two independent missions, one mission (perhaps joint U.S.-European), or no mission at all. In any case, well ahead of either of these potential missions, the European X-ray satellite eRosita is expected to produce an all-sky catalog of $\sim 10^5$ X-ray selected clusters, with X-ray temperature measurements

[4]We will use the term "Astro2010 report" to refer collectively to *New Worlds, New Horizons* and to the panel reports that supported it. In particular, detailed discussion of these science themes and related facilities can be found in the individual reports of the Cosmology and Fundamental Physics (CFP) Science Frontiers Panel and the Electromagnetic Observations from Space (EOS), Optical and Infrared Astronomy from the Ground (OIR), and Radio, Millimeter, and Sub-Millimeter Astronomy from the Ground (RMS) Program Prioritization Panels. Information on all of these reports can be found at `http://sites.nationalacademies.org/bpa/BPA_049810`.

[5]Not an acronym.

and resolved profiles for the brighter clusters.

The completion of the Astro2010 Decadal Survey and the Euclid selection by ESA make this an opportune time to review the techniques and prospects for probing cosmic acceleration with ambitious observational programs. Our goal is, in some sense, an update of the DETF report (Albrecht et al., 2006), incorporating the many developments in the field over the last few years and (the difference between a report and a review) emphasizing explanation rather than recommendation. We aim to complement other reviews of the field that differ in focus or in level of detail. To mention just a selection of these, we note that Frieman et al. (2008a) and Blanchard (2010) provide excellent overviews of the field, covering theory, current observations, and future experiments, Peebles and Ratra (2003) are especially good on history of the subject and on theoretical aspects of scalar field models, and Jain and Khoury (2010) review modified gravity models, discussing theoretical and observational aspects in great depth. Carroll (2003) and Linder (2003b, 2007) provide accessible and informative introductions at the less forbidding length of conference proceedings, and Linder (2010) provides a review aimed at a general scientific audience. The distinctive features of the present review are our in-depth discussion of individual observational methods and our new quantitative forecasts for how combinations of these methods can constrain parameters of cosmic acceleration theories.

To the extent that we have a consistent underlying theme, it is the importance of pursuing a balanced observational program. We do not believe that all methods or all implementations of methods are equal; some approaches have evident systematic limitations that will prevent them reaching the sub-percent accuracy level that is needed to make major contributions to the field over the next decade, while others would require prohibitively expensive investments to achieve the needed statistical precision. However, for a given level of community investment, we think there is more to be gained by doing a good job on the three or four most promising methods than by doing a perfect job on one at the expense of the others. A balanced approach offers crucial cross-checks against systematic errors, takes advantage of complementary information contained in different observables or complementary strengths in different redshift ranges, and holds the best chance of uncovering "surprises" that do not fit into the conventional categories of theoretical models. This philosophy will emerge most clearly in §3, where we present our quantitative forecasts. For understandable reasons, most articles and proposals (including some we have written ourselves) start from current knowledge and show the impact of adding a particular new experiment. We will instead start from a "fiducial program" that assumes ambitious but achievable advances in several different methods at once, then consider the impact of strengthening, weakening, or omitting its individual elements.

2. Observables, Parameterizations, and Methods

The two top-level questions about cosmic acceleration are:

1. Does acceleration arise from a breakdown of GR on cosmological scales or from a new energy component that exerts repulsive gravity within GR?
2. If acceleration is caused by a new energy component, is its energy density constant in space and time?

As already discussed in §1.2, the distinction between "modified gravity" and "new energy component" solutions may not be unambiguous. However, the cosmological constant hypothesis makes specific, testable predictions, and the combination of GR with relatively simple scalar field models predicts testable consistency relations between expansion and structure growth.

The answer to these questions, or a major step towards an answer, could come from a surprising direction: a theoretical breakthrough, a revealing discovery in accelerator experiments, a time-variation of a fundamental "constant," or an experimental failure of GR on terrestrial or solar system scales (see §**??** for brief discussion). However, "wait for a breakthrough" is an unsatisfying recipe for scientific progress, and there is one clear path forward: measure the history of expansion and the growth of structure with increasing precision over an increasing range of redshift and lengthscale.

2.1. Basic Equations

In GR, the expansion of a homogeneous and isotropic universe is governed by the Friedmann equation, which can be written in the form

$$\frac{H^2(z)}{H_0^2} = \Omega_m(1+z)^3 + \Omega_r(1+z)^4 + \Omega_k(1+z)^2 + \Omega_\phi \frac{u_\phi(z)}{u_\phi(z=0)}. \tag{3}$$

Here $H(z) \equiv \dot{a}/a$ is the Hubble parameter and Ω_m, Ω_r, and Ω_ϕ are the *present day* energy densities of matter, radiation, and a generic form of dark energy ϕ.[6] These are expressed as ratios to the critical energy density required for flat space geometry

$$\Omega_x = \frac{u_x}{\rho_{\rm crit} c^2}, \qquad \rho_{\rm crit} = \frac{3H_0^2}{8\pi G}. \tag{4}$$

At higher redshifts,

$$\Omega_m(z) \equiv \frac{\rho_m(z)}{\rho_{\rm crit}(z)} = \Omega_m(1+z)^3 \frac{H_0^2}{H^2(z)}, \tag{5}$$

where the second equality follows from the scaling $\rho_m(z) = \rho_m(z=0) \times (1+z)^3$ and from the definition of $\rho_{\rm crit}(z)$. In the formulation (3), the impact of curvature on expansion is expressed like that of a "dynamical" component with scaled energy density

$$\Omega_k \equiv 1 - \Omega_m - \Omega_r - \Omega_\phi, \tag{6}$$

with $\Omega_k = 0$ for a spatially flat universe.

As discussed in §**??**, BAO studies allow direct measurements of $H(z)$, and redshift-space distortions (§**??**) can effectively measure $H(z)/H_0$ by determining $\Omega_m(z)$. In most cases, however, observations constrain $H(z)$ indirectly by measuring the distance-redshift relation or the history of structure growth.

Hogg (1999) provides a compact and pedagogical summary of cosmological distance measures. The comoving line-of-sight distance to an object at redshift z is

$$D_C(z) = \frac{c}{H_0} \int_0^z dz' \frac{H_0}{H(z')} \ . \tag{7}$$

Defining a dimensional (length^{-2}) curvature parameter

$$K = -\Omega_k (c/H_0)^{-2} \tag{8}$$

[6] We will refer to values of these parameters at $z \neq 0$ as $\Omega_m(z)$, $\Omega_\phi(z)$, etc. When we *assume* a cosmological constant, we will replace Ω_ϕ by Ω_Λ.

allows us to write the comoving angular diameter distance,[7] relating an object's comoving size l to its angular size θ, as

$$D_A(z) = K^{-1/2} \sin\left(K^{1/2} D_C\right) \approx D_C \left[1 - \frac{1}{6} K D_C^2\right], \tag{9}$$

which applies for either sign of Ω_k and yields $D_A(z) = D_C(z)$ for $\Omega_k = 0$.[8] Note that positive space curvature ($\Omega_{\rm tot} > 1$) corresponds to negative Ω_k (and positive K), hence a smaller D_A and larger angular size than in a flat universe. If $u_\phi(z) > u_\phi(z=0)$, then compared to a cosmological constant model ($u_\phi = u_{\phi,0}$) with the same matter density and curvature, the Hubble parameter at $z > 0$ is higher (eq. 3), and distances to redshifts $z > 0$ are lower (eq. 9).

The luminosity distance relating an object's bolometric flux $f_{\rm bol}$ to its bolometric luminosity $L_{\rm bol}$ is

$$D_L = \sqrt{L_{\rm bol}/4\pi f_{\rm bol}} = D_A \times (1+z) \ . \tag{10}$$

The relation between luminosity and angular diameter distance is independent of cosmology, so the two measures contain the same information about $H(z)$ and Ω_k. For this reason, we will sometimes use $D(z)$ to stand in generically for either of these transverse distance measures. Some methods (e.g., counts of galaxy clusters) effectively probe the comoving volume element that relates solid angle and redshift intervals to comoving volume V_C. We will denote this quantity

$$dV_C(z) \equiv c H^{-1}(z) D_A^2(z) d\Omega \, dz. \tag{11}$$

On large scales, the gravitational evolution of fluctuations in pressureless dark matter follows linear perturbation theory, according to which

$$\delta(\mathbf{x}, t) \ \equiv \ \frac{\rho_m(\mathbf{x}, t) - \bar{\rho}_m}{\bar{\rho}_m} \ = \ \delta(\mathbf{x}, t_i) \times \frac{G(t)}{G(t_i)} \ , \tag{12}$$

where the linear growth function $G(t)$ obeys the differential equation

$$\ddot{G}_{\rm GR} + 2H(z)\dot{G}_{\rm GR} - \frac{3}{2}\Omega_m H_0^2 (1+z)^3 G_{\rm GR} = 0 \tag{13}$$

and the GR subscript denotes the fact that this equation applies in standard GR. The solution to this equation can only be written in integral form for specific forms of $H(z)$, and thus for specific dark energy models specifying $u_\phi(z)$. However, to a very good approximation the logarithmic growth rate of linear perturbations in GR is

$$f_{\rm GR}(z) \equiv \frac{d \ln G_{\rm GR}}{d \ln a} \approx [\Omega_m(z)]^\gamma \ , \tag{14}$$

where $\gamma \approx 0.55 - 0.6$ depends only weakly on cosmological parameters Peebles (1980); Lightman and Schechter (1990). Integrating this equation yields

$$\frac{G_{\rm GR}(z)}{G_{\rm GR}(z=0)} = \exp\left[-\int_0^z \frac{dz'}{1+z'} [\Omega_m(z')]^\gamma\right] \ , \tag{15}$$

[7] Note that Hogg 1999 refers to this quantity as the comoving transverse distance and uses D_A to denote the quantity relating *physical* size to angular size.

[8] Recall that $\sin(ix) = i \sinh(x)$.

where $\Omega_m(z)$ is given by equation (5). Linder (2005) shows that equation (15) is accurate to better than 0.5% for a wide variety of dark energy models if one adopts

$$\gamma = 0.55 + 0.05[1 + w(z = 1)] \tag{16}$$

(see also Wang and Steinhardt 1998; Weinberg 2005; Amendola et al. 2005). While the full solution of equation (13) should be used for high accuracy calculations, equation (15) is useful for intuition and for approximate calculations. Note in particular that if $u_\phi(z) > u_{\phi,0}$ then, relative to a cosmological constant model, $\Omega_m(z) \propto H^{-2}(z)$ is lower (eq. 5), so $G_{\rm GR}(z)/G_{\rm GR}(z = 0)$ is higher — i.e., there has been *less* growth of structure between redshift z and the present day because matter has been a smaller fraction of the total density over that time. It is often useful to refer the growth factor not to its $z = 0$ value but to the value at some high redshift when, in typical models, dark energy is dynamically negligible and $\Omega_m(z) \approx 1$. We will frequently use $z = 9$ as a reference epoch, in which case equation (15) becomes

$$\frac{G_{\rm GR}(z)}{G_{\rm GR}(z = 9)} = \exp\left[\int_z^9 \frac{dz'}{1 + z'}[\Omega_m(z')]^\gamma\right] . \tag{17}$$

In principle the age of the universe,

$$t(z) = \int_z^\infty \frac{dz'}{1 + z'} H^{-1}(z') , \tag{18}$$

is an observable that can probe the expansion history. The conflict between the ages of globular clusters and the value of t_0 in a decelerating universe is one of the significant arguments for cosmic acceleration, and some authors have employed ages of high-redshift galaxies as a constraint on dark energy models (e.g., **?**). However, we think that the systematic uncertainties in ages inferred from population synthesis will inevitably be too large to allow the percent-level measurements that are needed to make interesting further contributions to the field. Jimenez and Loeb (2002) have proposed using *differential* ages of galaxies at different redshifts to measure, in effect, $H(z)$. While this approach removes some of the uncertainties in the population synthesis models, it relies on identifying a population of galaxies at one redshift that is just an aged version of a population at a higher redshift, and it not clear that one can do this convincingly enough that one would believe a "surprising" dark energy result from this method.

2.2. Model Parameterizations

The properties of dark energy influence the observables — $H(z)$, $D(z)$, and $G(z)$ — through the history of $u_\phi(z)/u_{\phi,0}$ in the Friedmann equation (3). This history is usually framed in terms of the value and evolution of the equation-of-state parameter $w(z) = p_\phi(z)/u_\phi(z)$. Provided that the field ϕ is not transferring energy directly to or from other components (e.g., by decaying into dark matter), the first law of thermodynamics for a comoving volume implies

$$dU_\phi = d(u_\phi a^3) = -p_\phi dV = -p_\phi d(a^3) \tag{19}$$

$$\Longrightarrow \quad a^3 du_\phi + 3u_\phi a^2 da = -3w(z)u_\phi a^2 da \tag{20}$$

$$\Longrightarrow \quad d\ln u_\phi = -3[1 + w(z)]d\ln a = 3[1 + w(z)]d\ln(1 + z) , \tag{21}$$

where the last equality uses the definition $a = (1 + z)^{-1}$. Integrating both sides implies

$$\frac{u_\phi(z)}{u_\phi(z = 0)} = \exp\left[3\int_0^z [1 + w(z')]\frac{dz'}{1 + z'}\right] . \tag{22}$$

For a constant w independent of z we find

$$\frac{u_\phi(z)}{u_\phi(z=0)} = (1+z)^{3(1+w)}, \tag{23}$$

which yields the familiar results $u \propto (1+z)^3$ for pressureless matter and $u \propto (1+z)^4$ for radiation ($w = +\frac{1}{3}$), and which shows once again that a cosmological constant $u_\phi(z) =$ constant corresponds to $w = -1$.

The first obvious way to parameterize $w(z)$ is with a Taylor expansion $w(z) = w_0 + w'z + ...$, but this expansion becomes ill-behaved at high z. A more useful two-parameter model, introduced by Linder (2003a), is

$$w(a) = w_0 + w_a(1-a), \tag{24}$$

in which the value of w evolves linearly from $w_0 + w_a$ at small a (high z) to w_0 at $z = 0$. Observations usually provide the best constraint on w at some intermediate redshift, not at $z = 0$, so statistical errors on w_0 and w_a are highly correlated. This problem can be circumvented by recasting equation (24) in the equivalent form

$$w(a) = w_p + w_a(a_p - a) \tag{25}$$

and choosing the "pivot" expansion factor a_p so that the observational errors on w_p and w_a are uncorrelated (or at least weakly so). The value of a_p depends on what data sets are being considered, but in practice it is usually close to $z_p = a_p^{-1} - 1 \approx 0.4 - 0.5$ (see Table 5). The best-fit w_p is, approximately, the parameter of the constant-w model that would best reproduce the data. A cosmological constant would be statistically ruled out either if w_p were inconsistent with -1 or if w_a were inconsistent with zero. In practice, error bars on w_a are generally much larger than error bars on w_p, by a factor of $5 - 10$.

An alternative approach is to approximate $w(z)$ as a stepwise-constant function defined by its values in a number of discrete bins, perhaps with priors or constraints on the allowed values (e.g., $-1 \le w(z) \le 1$). For a given set of observations, this function can then be decomposed into orthogonal principal components (PCs), with the first PC being the one that is best constrained by the data, the second PC the next best constrained, and so forth. Variants of this approach have been widely adopted in recent investigations (e.g., **?**), including the report of the JDEM Figure-of-Merit Science Working Group (Albrecht et al., 2009). The PCA approach has the advantage of allowing quite general $w(z)$ histories to be represented, though in practice only a few PCs can be constrained well, and **?** have argued that the (w_p, w_a) parameterization has equal power for practical purposes. We will use both characterizations for our forecasts in §3.

Our equations so far have assumed that GR is correct. The alternative to dark energy is to modify GR in a way that produces accelerated expansion. One of the best-studied examples is DGP gravity (Dvali et al., 2000), which posits a five-dimensional gravitational field equation that leads to a Friedmann equation

$$H^2(z) = \frac{8\pi G}{3}\rho(z) \pm \frac{H}{cr_c} \tag{26}$$

for a spatially flat, homogeneous universe confined to a $3+1$-dimensional brane. Choosing the positive sign for the second term leads to an initially decelerating universe that transitions to accelerating, and ultimately exponential, expansion. Other modifications to the gravitational action will modify the Friedmann equation in different ways. Alternatively, one can simply postulate a modified Friedmann equation without specifying a complete gravitational theory, e.g., by replacing ρ on the r.h.s. of $H^2 \propto \rho$ with a parameterized function $H^2 \propto g(\rho)$ (Freese and Lewis, 2002;

Freese, 2005). Of course, there is no guarantee that such a function can in fact be derived from a self-consistent gravitational theory.

In addition to changing the Friedmann equation, a modified gravity model may alter the equation (13) that relates the growth of structure to the expansion history $H(z)$. Therefore, one general approach to testing modified gravity explanations is to search for inconsistency between observables that probe $H(z)$ or $D(z)$ and observables that also probe the growth function $G(z)$. Some methods effectively measure $G(z)/G(z=0)$, others measure $G(z)$ relative to an amplitude anchored in the CMB, and others measure the logarithmic growth index γ of equation (14). For "generic" parameters that describe departures from GR-predicted growth, we will use a parameter G_9 that characterizes an overall multiplicative offset of the growth factor and a parameter $\Delta\gamma$ that characterizes a change in the fluctuation growth rate. We define these parameters in §2.4 below, following our review of CMB anisotropy and large scale structure. It is also possible that modified gravity will cause $G(z)$ to be scale-dependent (see §**??**), or that it will alter the relation between gravitational lensing and the projected mass surface density (see §**??**), or that it will reveal its presence through a high-precision test on solar system or terrestrial scales (see §**??**).

The above considerations lead to the following general strategy for probing the physics of cosmic acceleration: use observations to constrain the functions $H(z)$, $D(z)$, and $G(z)$, and use these constraints in turn to constrain the history of $w(z)$ for dark energy models and to test for inconsistencies that could point to a modified gravity explanation. For pure $H(z)$ and $D(z)$ measurements, the "nuisance parameters" in such a strategy are the values of Ω_m and Ω_k, in addition to parameters related directly to the observational method itself (e.g., the absolute luminosity of supernovae). Assuming a standard radiation content, the value of $\Omega_\phi = 1-\Omega_m-\Omega_r-\Omega_k$ is fixed once Ω_m and Ω_k are known. The effects of Ω_m and Ω_k are separable both from their different redshift dependence in the Friedmann equation (3) and from the influence of Ω_k on transverse distances (eq. 9) via space curvature.

2.3. CMB Anisotropies and Large Scale Structure

CMB anisotropies have little direct constraining power on dark energy, but they play a critical role in cosmic acceleration studies because they often provide the strongest constraints on "nuisance parameters" such as Ω_m, Ω_k, and the high-redshift normalization of matter fluctuations. In particular, the amplitudes of the acoustic peaks in the CMB angular power spectrum depend sensitively (and differently) on the matter and baryon densities, and the locations of the peaks depend sensitively on spatial curvature. Using CMB constraints necessarily brings in additional nuisance parameters such as the spectral index n_s and curvature $dn_s/d\ln k$ of the scalar fluctuation spectrum, the amplitude and slope of the tensor (gravitational wave) fluctuation spectrum, the post-recombination optical depth τ, and the Hubble constant

$$h \equiv H_0/100 \text{ km s}^{-1} \text{ Mpc}^{-1}. \tag{27}$$

However, some of these parameters are themselves relevant to cosmic acceleration studies, and current CMB measurements yield tight constraints even after marginalizing over many parameters (e.g., Komatsu et al. 2011). The strength of these constraints depends significantly on the adopted parameter space — for example, current CMB data provide tight constraints on h if one assumes a flat universe with a cosmological constant, but these constraints are much weaker if Ω_k and w are free parameters.

CMB data are usually incorporated into dark energy constraints, or forecasts, by adding priors on parameters that are then marginalized over in the analysis. We will adopt this strategy in §3, using the level of precision forecast for the Planck satellite (**?**). However, it is worth noting

some rules of thumb. For practical purposes, Planck data will give near-perfect determinations of $\Omega_m h^2$ and $\Omega_b h^2$ from the heights of the acoustic peaks, where the h^2 dependence arises because it is the physical density that affects the acoustic features, not the density relative to the critical density. "Near-perfect" means that marginalizing over the expected uncertainties in $\Omega_m h^2$ and $\Omega_b h^2$ adds little to the error bars on dark energy parameters even from ambitious "Stage IV" experiments, relative to assuming that they are known perfectly.[9] Planck data will also give near-perfect determinations of the sound horizon s_* at recombination, which determines the physical scale of the acoustic peaks in the CMB and the scale of BAO in large scale structure. Since the angular scale of the acoustic peaks is precisely measured, Planck data should also yield a near-perfect determination of the angular diameter distance to the redshift of recombination, $D_* \equiv D_A(z_*)$. Finally, the amplitude of CMB anisotropies gives a near-perfect determination (after marginalizing over the optical depth τ, which is constrained by polarization data) of the amplitude of matter fluctuations at $z_{\rm rec}$, and thus throughout the era in which dark energy (or deviation from GR) is negligible. As emphasized by Hu (2005; an excellent source for more detailed discussion of CMB anisotropies in the context of dark energy constraints), these determinations all depend on the assumptions of a standard thermal and recombination history, but the CMB data themselves allow tests of these assumptions at the required level of accuracy. CMB data also allow tests of cosmic acceleration models via the integrated Sachs-Wolfe (ISW) effect, which we discuss briefly in §**??**.

If primordial matter fluctuations are Gaussian, as predicted by simple inflation models and supported by most observational investigations to date, then their statistical properties are fully specified by the power spectrum $P(k)$ or its Fourier transform, the two-point correlation function $\xi(r)$. Defining the Fourier transform of the density contrast[10]

$$\tilde{\delta}(\mathbf{k}) = \int d^3r e^{-i\mathbf{k}\cdot\mathbf{r}}\delta(\mathbf{r}), \qquad \delta(\mathbf{r}) = (2\pi)^{-3}\int d^3k e^{i\mathbf{k}\cdot\mathbf{r}}\tilde{\delta}(\mathbf{k}), \tag{28}$$

the power spectrum is defined by

$$\langle\tilde{\delta}(\mathbf{k})\tilde{\delta}(\mathbf{k}')\rangle = (2\pi)^3 P(k)\delta_D^3(\mathbf{k}-\mathbf{k}'), \tag{29}$$

where δ_D^3 is a 3-d Dirac-delta function and isotropy guarantees that $P(\mathbf{k})$ is a function of $k = |\mathbf{k}|$ alone. The power spectrum has units of volume, and it is often more intuitive to discuss the dimensionless quantity

$$\Delta^2(k) \equiv (2\pi)^{-3}\times 4\pi k^3 P(k) = \frac{d\sigma^2}{d\ln k}, \tag{30}$$

which is the contribution to the variance $\sigma^2 \equiv \langle\delta^2\rangle$ of the density contrast per logarithmic interval of k. The variance of the density field smoothed with a window $W_R(r)$ of scale R is

$$\sigma^2(R) = \int_0^\infty \frac{dk}{k}\Delta^2(k)\widetilde{W}_R^2(k), \tag{31}$$

where the Fourier transform of a top-hat window, $W_R(r) = (4\pi R^3/3)^{-1}\Theta(1-r/R)$, is

$$\widetilde{W}_R(k) = \frac{3}{k^3R^3}\left[\sin(kR) - kR\cos(kR)\right], \tag{32}$$

[9]However, the effects of *Planck*-level CMB uncertainties are not completely negligible. For the fiducial Stage IV program discussed in §3, fixing $\Omega_m h^2$ and $\Omega_b h^2$ instead of marginalizing increases the DETF Figure of Merit from 533 to ~ 700.

[10]A variety of Fourier conventions float around the cosmology literature. Here we adopt the same Fourier conventions and definitions as Dodelson (2003).

and the Fourier transform of a Gaussian window, $W_R(r) = (2\pi)^{-3/2} R^{-3} e^{-r^2/2R^2}$, is

$$\widetilde{W}_R(k) = e^{-k^2R^2/2}. \tag{33}$$

The correlation function is

$$\xi(r) \equiv \langle \delta(\mathbf{x})\delta(\mathbf{x}+\mathbf{r})\rangle = \int_0^\infty \frac{dk}{k}\Delta^2(k)\frac{\sin(kr)}{kr}. \tag{34}$$

In linear perturbation theory, the power spectrum amplitude is proportional to $G^2(z)$, and we will take $P_{\rm lin}(k)$ to refer to the $z = 0$ normalization when the redshift is not otherwise specified:

$$P_{\rm lin}(k,z) = \frac{G^2(z)}{G^2(z=0)}P_{\rm lin}(k). \tag{35}$$

We discuss the normalization of $G(z)$ and $P_{\rm lin}(k)$ more precisely in §2.4 below. The evolution of $P(k)$ remains close to linear theory for scales $k \ll k_{\rm nl}$, where

$$\int_0^{k_{\rm nl}} \frac{dk}{k}\Delta^2(k) = 1. \tag{36}$$

For realistic power spectra, non-linear evolution on small scales does not feed back to alter the linear evolution on large scales. However, the shape of the power spectrum does change on scales approaching $k_{\rm nl}$, in ways that can be calculated using N-body simulations (Heitmann et al., 2010) or several variants of cosmological perturbation theory (Carlson et al. 2009 and references therein). Non-linear evolution is a significant effect for weak lensing predictions and for the evolution of BAO, as we discuss in the corresponding sections below.

While there are many ways of characterizing the matter distribution in the non-linear regime, the two measures that matter the most for our purposes are the mass function and clustering bias of dark matter halos. There are several different algorithms for identifying halos in N-body simulations, all of them designed to pick out collapsed, gravitationally bound dark matter structures in approximate virial equilibrium. It is convenient to express the halo mass function in the form

$$\frac{dn}{d\ln M} = f(\sigma)\bar{\rho}_m \frac{d\ln\sigma^{-1}}{dM}, \tag{37}$$

where σ^2 is the variance of the linear density field smoothed with a top-hat filter of mass scale $M = \frac{4}{3}\pi R^3\bar{\rho}_m$ (eqs. 31 and 32). To a first approximation, the function $f(\sigma)$ is universal, and the effects of power spectrum shape, redshift (and thus power spectrum amplitude), and background cosmological model (e.g., Ω_m and Ω_Λ) enter only through determining $d\ln\sigma^{-1}/dM$ and $\bar{\rho}_m$. The state-of-the-art numerical investigation is that of Tinker et al. (2008), who fit a large number of N-body simulation results with the functional form

$$f(\sigma) = A\left[\left(\frac{\sigma}{b}\right)^{-a} + 1\right] e^{-c/\sigma^2}, \tag{38}$$

finding best-fit values $A = 0.186$, $a = 1.47$, $b = 2.57$, $c = 1.19$ for $z = 0$ halos, defined to be spherical regions centered on density peaks enclosing a mean interior overdensity of 200 times the cosmic mean density $\bar{\rho}_m$. (Different halo mass definitions lead to different coefficients.) A similar functional form was justified on analytic grounds by Sheth and Tormen (1999), following a chain

of argument that ultimately traces back to Press and Schechter (1974) and Bond et al. (1991). Discussions of the halo population frequently refer to the characteristic mass scale M_*, defined by

$$\sigma(M_*) = \delta_c = 1.686, \tag{39}$$

which sets the location of the exponential cutoff in the Press-Schechter mass function. Here δ_c is the linear theory overdensity at which a spherically symmetric perturbation would collapse.[11]

In detail, Tinker et al. (2008) find that $f(\sigma)$ depends on redshift at the 10-20% level, probably because of the dependence of halo mass profiles on $\Omega_m(z)$. At overdensities of ~ 200, the baryon fraction in group and cluster mass halos ($M > 10^{13} M_\odot$) is expected to be close to the cosmic mean ratio Ω_b/Ω_m, but in detail gas pressure, dissipation, and feedback from star formation and AGN can alter this fraction and change baryon density profiles relative to dark matter profiles. We discuss these issues further in §**??**.

Massive halos are more strongly clustered than the underlying matter distribution because they form near high peaks of the initial density field, which arise more frequently in regions where the background density is high (Kaiser, 1984; Bardeen et al., 1986). On large scales, the correlation function of halos of mass M is a scale-independent multiple of the matter correlation function $\xi_{hh}(r) = b_h^2(M)\xi_{mm}(r)$. The halo-mass cross-correlation in this regime is $\xi_{hm}(r) = b_h(M)\xi_{mm}(r)$, and similar scalings ($b_h^2$ and b_h) hold for the halo power spectrum and halo-mass cross spectrum at low k. Analytic arguments suggest a bias factor (Cole and Kaiser, 1989; Mo and White, 1996)

$$b_h(M) = 1 + \frac{[\sigma(M)/\delta_c]^2 - 1}{\delta_c}. \tag{40}$$

There have been numerous refinements to this formula based on analytic models and numerical calibrations. The state-of-the-art numerical study is that of Tinker et al. (2010).

Galaxies reside in dark matter halos, and they, too, are biased tracers of the underlying matter distribution. Here one must allow for the fact that different kinds of galaxies reside in different mass halos and that massive halos host multiple galaxies. More massive or more luminous galaxies are more strongly clustered because they reside in more massive halos that have higher $b_h(M)$. At low redshift, the large scale bias factor is $b_g \leq 1$ for galaxies below the characteristic cutoff L^* of the Schechter (1976) luminosity function, but it rises sharply at higher luminosities (Norberg et al., 2001; Zehavi et al., 2005, 2010).

For a galaxy sample defined by a threshold in optical or near-IR luminosity (or stellar mass), theoretical models and empirical studies (too numerous to list comprehensively, but our summary here is especially influenced by Kravtsov et al. 2004; Conroy et al. 2006; Zehavi et al. 2010) suggest the following approximate model. The minimum host halo mass is the one for which the comoving space density $n(M_{\rm min})$ of halos above $M_{\rm min}$ matches the space density $n(L)$ of galaxies above the luminosity threshold. Each halo above $M_{\rm min}$ hosts one central galaxy, and in addition each such halo hosts a mean number of satellite galaxies $\langle N_{\rm sat}\rangle = (M - M_{\rm min})/15M_{\rm min}$, with the actual number of satellites drawn from a Poisson distribution with this mean.[12] The large scale galaxy bias factor b_g is the average bias factor $b_h(M)$ of halos above $M_{\rm min}$, with the average weighted by

[11] See Gunn and Gott (1972), but note that their argument must be corrected to growing mode initial conditions, as is done in standard textbook treatments. The value $\delta_c = 1.686$ is derived for $\Omega_m = 1$, but the cosmology dependence is weak.

[12] To make the model more accurate, one should adjust $M_{\rm min}$ iteratively so that the *total* space density of galaxies, central+satellite, matches the observed $n(L)$, but this is usually a modest correction because the typical fraction of galaxies that are satellites is $5 - 20\%$.

the product of the halo space density and the average number of galaxies per halo. In addition to increasing b_g by giving more weight to high mass halos, satellite galaxies contribute to clustering on small scales, where pairs or groups of galaxies reside in a single halo (Seljak, 2000; Scoccimarro et al., 2001; Berlind and Weinberg, 2002). In detail, at high luminosities one must allow for scatter between galaxy luminosity and halo mass, which reduces the bias below that of the sharp threshold model described above. Furthermore, selecting galaxies by color or spectral type alters the relative fractions of central and satellite galaxies; redder, more passive galaxies are more strongly clustered because a larger fraction of them are satellites, and the reverse holds for bluer galaxies with active star formation.

On large scales, where $b_g^2 \Delta^2_{\rm lin}(k,z) \ll 1$, the galaxy power spectrum should have the same shape as the linear matter power spectrum, $P_{gg}(k,z) = b_g^2 P_{\rm lin}(k,z)$. However, scale-dependence of bias at the 10-20% level can persist to quite low k, especially for luminous, highly biased galaxy populations (Yoo et al., 2009). Combinations of CMB power spectrum measurements with galaxy power spectrum measurements can yield tighter cosmological parameter constraints than either one in isolation (e.g., Cole et al. (2005); Reid et al. (2010b)). In particular, this combination provides greater leverage on the Hubble constant h, since CMB-constrained models predict galaxy clustering in Mpc while galaxy redshift surveys measure distances in h^{-1} Mpc (or, equivalently, in km s^{-1}).

Another complicating factor in galaxy clustering measurements is redshift-space distortion (Kaiser 1987; see Hamilton (1997) for a comprehensive review), which arises because galaxy redshifts measure a combination of distance and peculiar velocity rather than true distance. On small scales, velocity dispersions in collapsed objects stretch structures along the line of sight. On large scales, coherent inflow to overdense regions compresses them in the line-of-sight direction, and coherent outflow from underdense regions stretches them along the line of sight. In linear perturbation theory, the divergence of the peculiar velocity field is related to the density contrast field by

$$\vec{\nabla} \cdot \mathbf{v}(\mathbf{x},z) = -(1+z)^{-1} H(z) \frac{d\ln G}{d\ln a} \delta(\mathbf{x},z) \approx -(1+z)^{-1} H(z) [\Omega_m(z)]^\gamma \delta(\mathbf{x},z). \quad (41)$$

The galaxy redshift-space power spectrum in linear theory is anisotropic, depending on the angle θ between the wavevector $\mathbf{k}$ and the observer's line of sight as

$$P_g(k,\mu) = b_g^2 (1+\beta\mu^2)^2 P(k), \quad (42)$$

where $P(k)$ is the real-space matter power spectrum, $\mu \equiv \cos\theta$, and

$$\beta \equiv \frac{1}{b_g} \frac{d\ln G}{d\ln a} \approx \frac{\Omega_m^\gamma}{b_g}. \quad (43)$$

A variety of non-linear effects, most notably the small scale dispersion and its correlation with large scale density, mean that equation (42) is rarely an adequate approximation in practice, even on quite large scales (Cole et al., 1994; Scoccimarro, 2004). In the galaxy correlation function, one can remove the effects of redshift-space distortion straightforwardly by projection, counting galaxy pairs as a function of projected separation rather than 3-d redshift-space separation. For the power spectrum, one can correct for redshift-space distortion, but the analysis is more model-dependent (see, e.g., Tegmark et al. 2004). However, redshift-space distortion can be an asset as well as a nuisance, since it provides a route to measuring $d\ln G/d\ln a$. We will discuss this idea in §**??** below.

2.4. Parameter Dependences and CMB Constraints

Figure 1 illustrates the four statistics discussed above, the CMB angular power spectrum, the matter variance $\Delta^2(k)$ computed from the linear theory power spectrum at $z = 0$, the $z = 0$

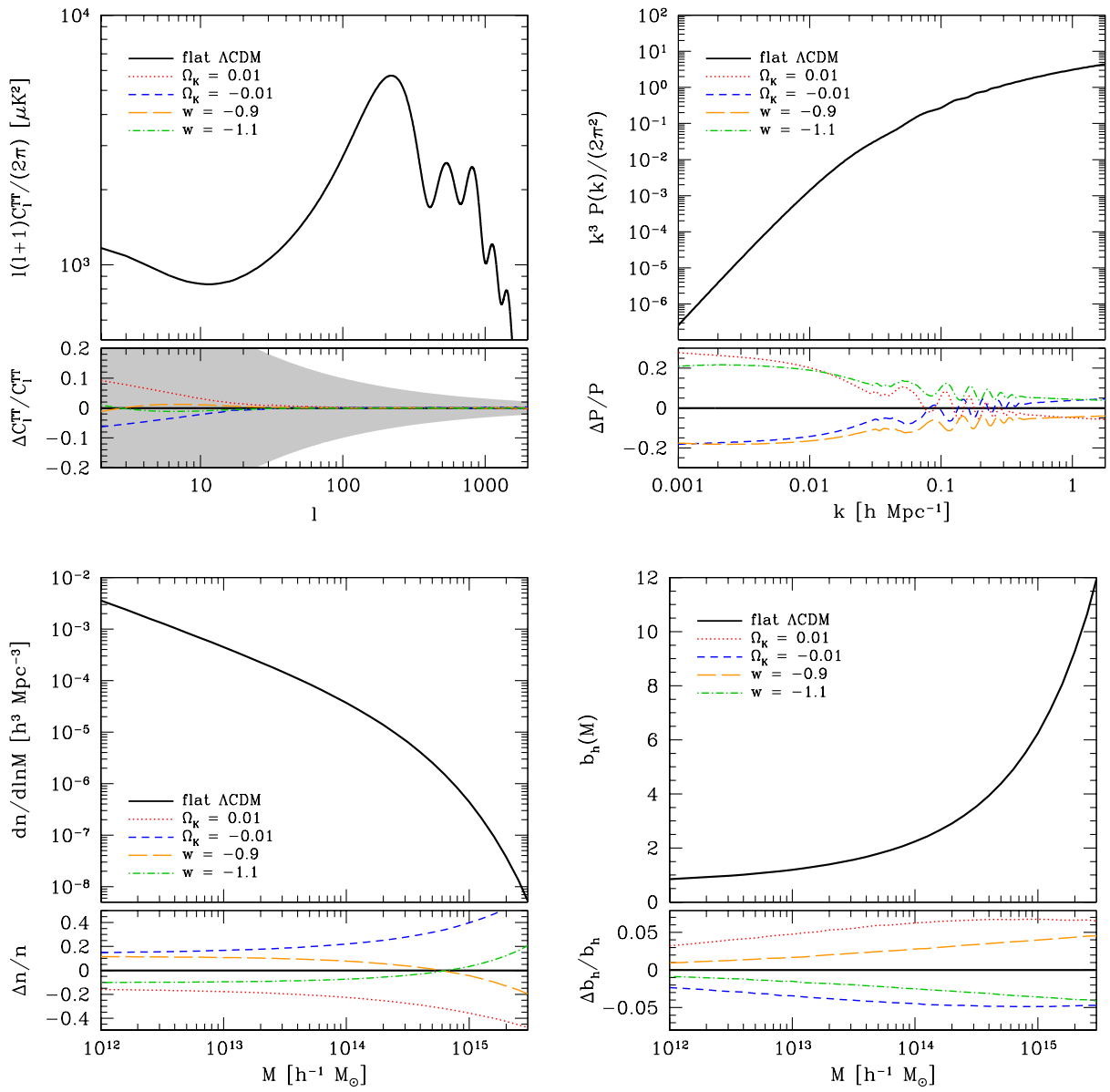

Figure 1 CMB angular power spectrum (upper left), variance of matter fluctuations (upper right), halo mass function (lower left), and halo bias factor (lower right). Solid curves in the main panels show predictions of the fiducial ΛCDM panel listed in Table 1. Curves in the lower panels show the fractional changes in these statistics induced by changing $1 + w$ to ± 0.1 or Ω_k to ± 0.01 (see legend). For each parameter change, we keep $\Omega_m h^2$, $\Omega_b h^2$, and D_* fixed by adjusting Ω_m, Ω_b, and h (see Table 1). These compensating changes keep deviations in the CMB spectrum minimal, much smaller than the cosmic variance errors indicated by the shaded region.

Table 1. Fiducial Model and Simple Variants

w	Ω_k	Ω_c	Ω_b	Ω_ϕ	h	σ_8
−1.0	**0.00**	**0.222**	**0.045**	**0.733**	**0.710**	**0.806**
−0.9	0.00	0.246	0.050	0.704	0.675	0.774
−1.1	0.00	0.201	0.041	0.758	0.746	0.837
−1.0	0.01	0.186	0.038	0.766	0.776	0.809
−1.0	−0.01	0.256	0.052	0.702	0.661	0.802

Note. — All models have $n_s = 0.963$, $\tau = 0.088$, $A_s(k = 0.002\,\mathrm{Mpc}^{-1}) = 2.43 \times 10^{-9}$.

halo mass function computed from equations (37) and (38), and the halo bias factor computed from equation (6) of Tinker et al. (2010) for overdensity 200 halos (relative to the mean matter density). Curves in the main panels show a fiducial model with the likelihood-weighted mean parameters for the seven-year WMAP CMB measurements (Larson et al., 2011) assuming a flat universe with a cosmological constant: $\Omega_c = 0.222$, $\Omega_b = 0.045$, $\Omega_\Lambda = 0.733$, $h = 0.71$, $n_s = 0.963$, $A_s(k = 0.002\,\mathrm{Mpc}^{-1}) = 2.43 \times 10^{-9}$, and post-recombination optical depth $\tau = 0.088$. (These parameters also assume no tensor fluctuations and $dn_s/d\ln k = 0$.) The CMB power spectrum shows the familiar pattern of acoustic peaks, with the angular scale of the first peak corresponding to the sound horizon at recombination divided by the angular diameter distance to the last scattering surface. The matter variance $\Delta^2(k)$ shows a slow change of slope starting at $k \approx 0.02h\,\mathrm{Mpc}^{-1}$, corresponding to the horizon scale at matter-radiation equality, and low amplitude wiggles at smaller scales produced by BAO. The halo mass function has an approximate power-law form at low masses changing slowly to an exponential cutoff for $M \gg M_* = 3 \times 10^{12} h^{-1}\,M_\odot$. The $b_h(M)$ relation is roughly flat for $M \lesssim 5M_*$ before rising steeply at higher masses. The h-dependences used for k, $dn/d\ln M$, and M reflect the dependences that typically arise when distances are estimated from redshifts and thus scale as h^{-1}.

In the lower panels, we show the fractional change in these statistics that arises when changing $1+w$ from 0 to ± 0.1 and when changing Ω_k from 0 to ± 0.01. With any parameter variation, there is the crucial question of what one holds fixed. For this figure, we have held fixed the parameter combinations that have the strongest impact on the CMB power spectrum: $\Omega_m h^2$ and $\Omega_b h^2$, which determine the heights of the acoustic peaks and the physical scale of the sound horizon, and $D_* = D_A(z_{\rm rec})$, which maps the physical scale of the peaks into the angular scale. We satisfy these constraints by allowing h and Ω_m to vary, maintaining $\Omega_k = 0$ for the w-variations and $w = -1$ for the Ω_k-variations, with n_s, A_s, and τ fixed to the fiducial model values. The parameter values for these variant models appear in Table 1.

From the CMB panel, we can see that the changes in the angular power spectrum induced by these parameter variations are small compared to the cosmic variance error at every l, since we have fixed the parameter combinations that mostly determine the CMB spectrum. The changes are coherent, of course, but even considering model fits to the entire CMB spectrum the w changes would be undetectable at the level of errors forecast for *Planck*, while the $\Omega_k = \pm 0.01$ models would be distinguishable from the fiducial model at about 1.5σ. The impact of these parameter changes

must instead be sought in other statistics at much lower redshifts. Changes to the matter variance are $\sim 5\%$ at small scales, growing to $\sim 20\%$ at large scales, with oscillations that reflect the shift in the BAO scale. Fractional changes to the halo space density at fixed mass can be much larger, especially at high masses where the abundance is exponentially rare. We caution, however, that the fractional change in mass at fixed abundance is much smaller, a point that we emphasize in §**??**. The impact of a change in w reverses sign at $M \approx 6 \times 10^{14} h^{-1}\, M_\odot \approx 200 M_*$, where the mass function begins to drop sharply. Changes in bias factor at fixed mass are $\sim 5\%$ at high masses and smaller at low masses.

Figure 2 shows the redshift evolution and parameter sensitivity of the Hubble parameter (eq. 3) and the angular diameter distance (eq. 9), for the same fiducial model and parameter variations used in Figure 1. The upper panels show $H(z)$ and $D_A(z)$ in absolute units, while the lower panels plot the combinations $H(z)/h$ and $hD_A(z)$. BAO studies measure in absolute units, but supernova studies effectively measure $hD_A(z)$ because they are calibrated in the local Hubble flow. Equivalently, supernova distances are in h^{-1} Mpc rather than Mpc. Weak lensing predictions depend on distance ratios rather than absolute distances, so in practice they also constrain $hD_A(z)$ rather than absolute $D_A(z)$.

In absolute units, model predictions diverge most strongly at $z = 0$, and the impact of $\Omega_k = \pm 0.01$ is larger than the impact of $1 + w = \pm 0.1$. The impact of the w change on $H(z)$ reverses sign at $z \approx 0.6$, a consequence of our CMB normalization. Changing w to -0.9 would on its own reduce the distance to z_*, and H_0 must therefore be lowered to keep D_* fixed. However, with $\Omega_m h^2$ fixed, lower H_0 implies a higher Ω_m, which raises the ratio $H(z)/H_0$, and at high redshift this effect wins out over the lower H_0. At $z > 2$, $D(z)$ remains sensitive to Ω_k but is insensitive to w, while the sensitivity of $H(z)$ to w is roughly flat for $1 < z < 3$. In h^{-1} Mpc units, models converge at $z = 0$ by definition, and the impact of $1 + w = \pm 0.1$ is generally larger than the impact of $\Omega_k = \pm 0.01$. The sensitivity of $hD(z)$ to parameter changes increases monotonically with increasing redshift, growing rapidly until $z = 0.5$ and flattening beyond $z = 1$.

For structure growth, the issues of normalization are more subtle. The normalization of the matter power spectrum is known better from CMB anisotropy at $z_{\rm rec}$ than it is from local measurements at $z = 0$, and this will be still more true in the Planck era. It therefore makes sense to anchor the normalization in the CMB, even though the value at $z = 0$ then depends on cosmological parameters. Figure 3 plots $(1 + z)G_{\rm GR}(z)$, where $G_{\rm GR}(z)$ obeys equation (13) and is normalized to to unity at $z = 9$. In most models, dark energy is dynamically negligible at $z > 9$, making the growth from the CMB era up to that epoch independent of dark energy. In an $\Omega_m = 1$ universe, $G_{\rm GR}(z) \propto (1+z)^{-1}$, so the plotted ratio falls below unity when $\Omega_m(z)$ starts to fall below one. For $\Omega_k = 0.01$, $\Omega_m(z)$ is below that in our fiducial model (see eqs. 3 and 5) both because of the Ω_k term in the Friedmann equation and because we lower $\Omega_m(z = 0)$ from 0.27 to 0.22 to keep D_* fixed, thus depressing $G_{\rm GR}(z)$ increasingly towards lower z. For $w = -0.9$, however, the depression of $\Omega_m(z)/\Omega_m(z = 0)$ from the Friedmann equation is countered by the higher value of $\Omega_m(z = 0) = 0.30$ adopted to fix D_*, so the depression of $G_{\rm GR}(z)$ is smaller, and it actually recovers towards the fiducial value as z approaches zero.

In practice, observations do not probe the growth factor itself but the amplitude of matter clustering, and in this case we must also account for the changing relation between the CMB power spectrum and the matter clustering normalization. The left panel of Figure 4 plots $\sigma_8(z) \times (1 + z)$, where $\sigma_8(z)$ is the rms linear theory density contrast in a sphere of comoving radius $8\,h^{-1}$ Mpc (eqs. 31 and 32). The right panel instead plots $\sigma_{11,\rm abs}(z) \times (1 + z)$, where $\sigma_{11,\rm abs}$ refers to a sphere of radius 11 Mpc (*not* h^{-1} Mpc). At high redshift these curves go flat as $\Omega_m(z)$ approaches one and the growth rate approaches $G(z) \propto (1 + z)^{-1}$. In the CMB-matched models considered here, the impact of w or Ω_k changes is complex, since changing these parameters alters the best-fit values

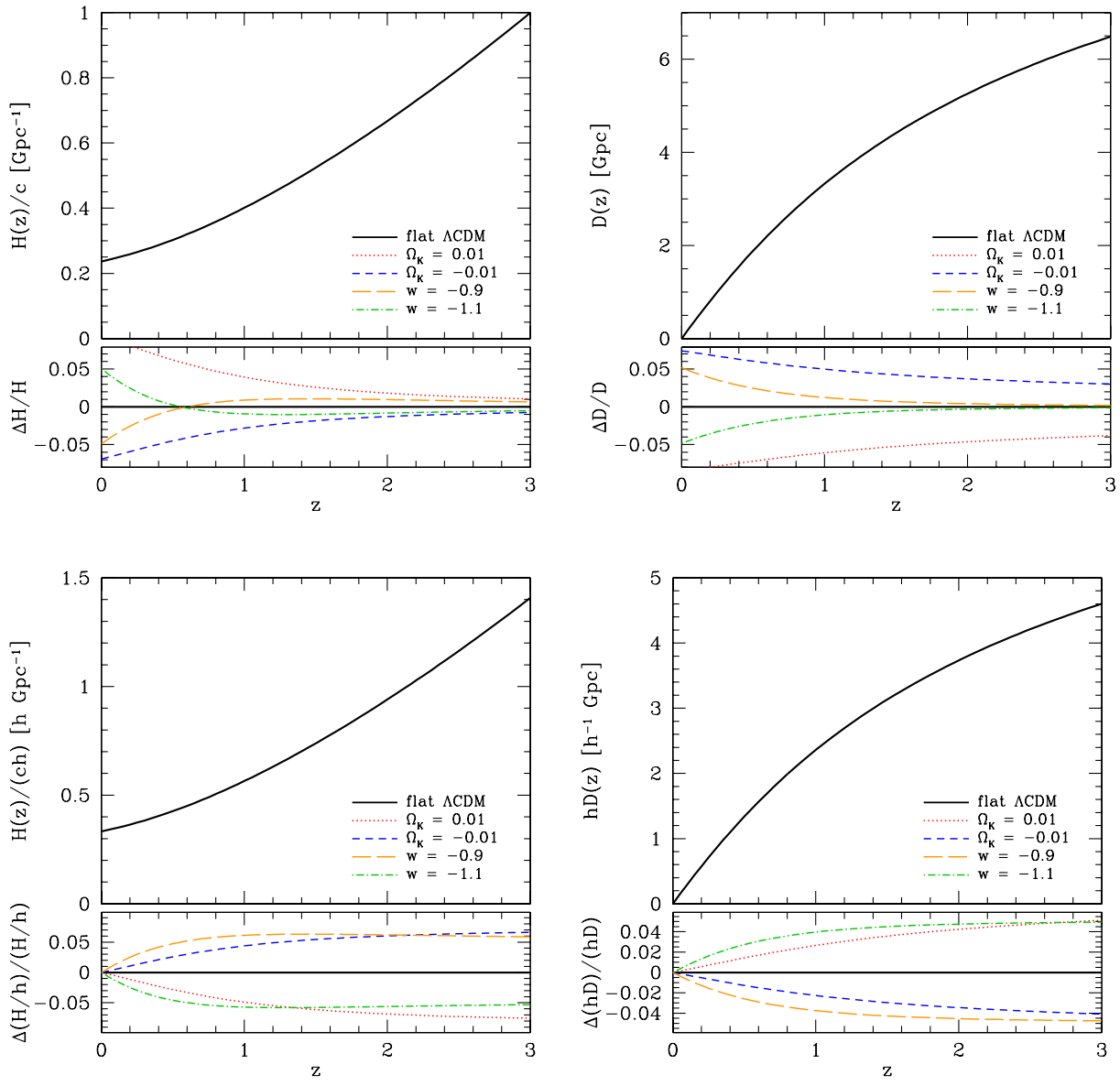

Figure 2 Evolution of the Hubble parameter (left) and the comoving angular diameter distance (right) for the fiducial ΛCDM model and for the variant models shown in Figure 1. Upper panels are in absolute units, relevant for BAO, while lower panels show distances in h^{-1} Gpc, relevant for supernovae or weak lensing.

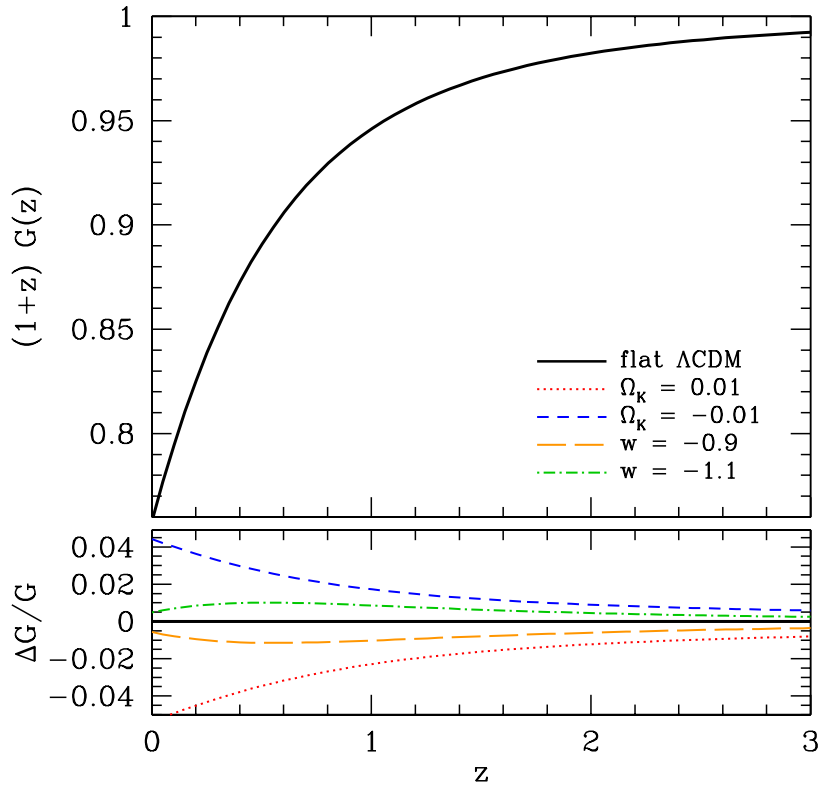

Figure 3 Evolution of the linear growth factor for the models shown in Figure 2, assuming GR. The scaling in the upper panel removes the $(1 + z)$ evolution that would arise in an $\Omega_m = 1$ universe and normalizes $G_{\rm GR}(z)$ to one at $z = 9$.

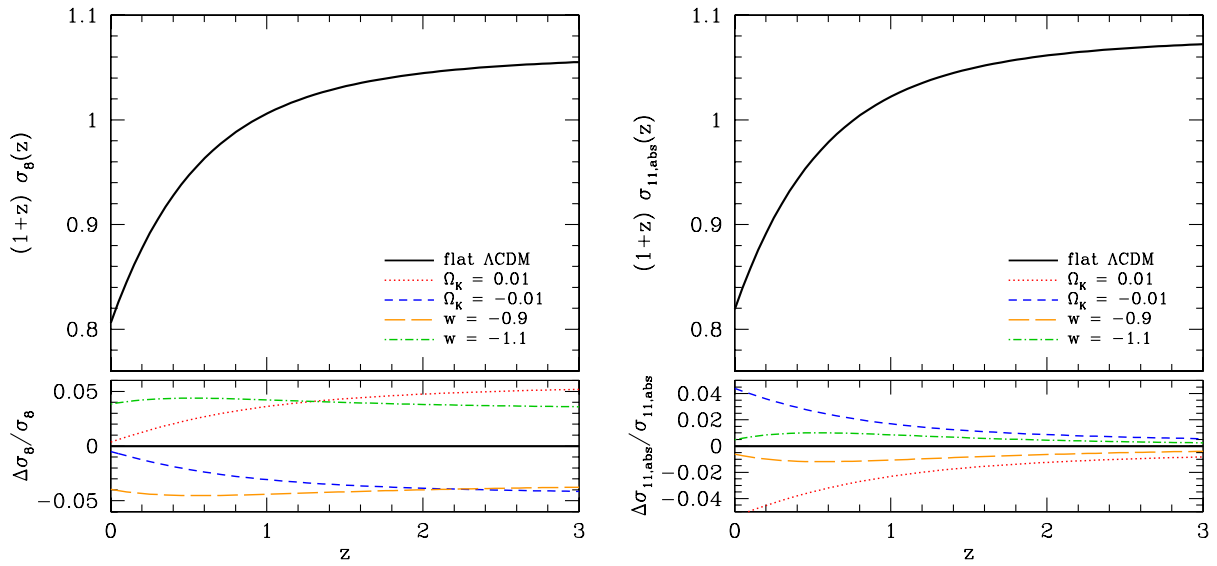

Figure 4 Evolution of the matter fluctuation amplitude for the models shown in Figure 3, characterized by the rms linear fluctuation in comoving spheres of radius $8\,h^{-1}$ Mpc (left) or 11 Mpc (right). All models are normalized to the WMAP7 CMB fluctuation amplitude.

of Ω_m and h as well as changing the growth factor directly through equation (15). The values of $\sigma_8(z)$ change by $4-5\%$ at all z for $1+w=\pm0.1$, but thse changes mostly track the changes in h. In absolute units, $\sigma_{11,\rm abs}(z)$, the changes are $\lesssim 1\%$. For $\Omega_k=\pm0.01$, $\sigma_8(z)$ changes by 4-5% at high z but converges nearly to the fiducial value at $z=0$, while $\sigma_{11,\rm abs}(z)$ shows only 1% differences at high z but diverges at low z.

All of these models have the WMAP7 (Larson et al., 2011) normalization of the power spectrum of inflationary fluctuations, $A_s=2.43\times10^{-9}$ at comoving scale $k=0.002\,{\rm Mpc}^{-1}$ at $z=z_{\rm rec}=1089$. The primary uncertainty in this normalization is the degeneracy with the electron optical depth τ, since late-time scattering suppresses the amplitude of the primary CMB anisotropies by a factor $e^{-\tau}$ on the scales that determine the normalization. The WMAP7 constraints are $\tau=0.088\pm0.015$ (1σ), so the associated uncertainty in the matter fluctuation amplitude is 1.5%. (Recall that the power spectrum amplitude is $\propto\sigma_8^2$, so its fractional error is a factor of two larger.) For Planck, the forecast uncertainty in τ is 0.005 if reionization is nearly instantaneous, making a 0.5% uncertainty in matter fluctuation amplitude once other cosmological parameters, including $w(z)$, are specified. This uncertainty is small but not negligible compared to anticipated constraints on the low redshift matter fluctuation amplitude from future weak lensing measurements.

Following Albrecht et al. (2009), we parameterize departures from the GR growth rate by a change $\Delta\gamma$ of the growth index (eq. 14) and by an overall amplitude shift G_9 that is the ratio of the matter fluctuation amplitude at $z=9$ to the value that would be predicted by GR given the same cosmological parameters and $w(z)$ history.[13] Some caution is required in defining $\Delta\gamma$, since equations (14)-(16) are not exact, and their inaccuracies should not be defined as failures of GR! For precise calculations, therefore, we adopt the Albrecht et al. (2009) expressions for growth factor

[13] Albrecht et al. (2009) denote this quantity G_0 instead of G_9.

evolution:

$$f(z) = f_{\rm GR}(z)\,(1+\Delta\gamma\ln\Omega_m(z)) \quad (44)$$

$$G(z) = G_9\times G_{\rm GR}(z)\times\exp\left[\Delta\gamma\int_z^9\frac{dz'}{1+z'}f_{\rm GR}(z')\ln\Omega_m(z')\right], \quad (45)$$

where $G_{\rm GR}(z)$ and $f_{\rm GR}(z)$ follow the (exact) solution to equation (13).

For practical purposes, one can use our definition of growth parameters to calculate the normalized linear theory matter power spectrum at redshift z, given an assumed set of cosmological parameter values and a $w(z)$ history, as follows. First, use CAMB (Lewis et al., 2000) or some similar program to compute the normalized linear matter power spectrum at $z=9$. Then multiply the power spectrum by $G^2(z)/G^2_{\rm GR}(z=9)$, with $G(z)$ given by equation (45) and $G_{\rm GR}(z)/G_{\rm GR}(z=9)$ given by the exact solution to equation (13), or by the approximate integral solution (17), computing $H(z)$ and $\Omega_m(z)$ from equations (3) and (5) given the cosmological parameters and $w(z)$. For reference, we note that CAMB normalization with WMAP7 data yields, for a flat ΛCDM model,

$$\sigma_8(z=9)\times(1+9) = 1.118\left[\frac{A_s(k=0.002\,{\rm Mpc}^{-1})}{2.43\times10^{-9}}\right]^{1/2}(75.85h)^{(n_s-1)/2} \times\left(\frac{\Omega_b h^2}{0.023}\right)^{-0.340}\left(\frac{\Omega_m h^2}{0.13}\right)^{0.574}\left(\frac{h}{0.71}\right)^{0.674}. \quad (46)$$

This formula, similar to that in Hu and Jain (2004), is found by varying the parameters in CAMB calculations one at a time to evaluate logarithmic derivatives; spot checks indicate that it is accurate to 0.2% over the 2σ range of the WMAP7 errors, and for the range of w and Ω_k variations in Table 1. For other models, one can use this formula to get $\sigma_8(z=9)$ in GR, assuming that the effect of dark energy at $z>9$ is negligible, then multiply by $G(z)/G_{\rm GR}(z=9)$ to get $\sigma_8(z)$.

There are, of course, degeneracies between the modified gravity parameters G_9 and $\Delta\gamma$ and the $w(z)$ history, since both affect structure growth. However, if $w(z)$ is pinned down well by $D(z)$ and $H(z)$ measurements, then measurements of matter clustering can be used to constrain G_9 and $\Delta\gamma$. The clustering amplitude at a single redshift yields a degenerate combination of these two parameters, but measurements at multiple redshifts or direct measurements of the growth rate via redshift-space distortions can separate them in principle. Of course, there is no guarantee that a modified gravity prediction can be adequately described by G_9 and a constant $\Delta\gamma$, and one might more generally consider (in eq. 45), for example, a functional history $\gamma(z)$ analogous to $w(z)$. However, any constraints inconsistent with $G_9=1$, $\Delta\gamma=0$ after marginalizing over $w(z)$ and cosmological parameters would be suggestive evidence for a breakdown of GR. Even if the measurements themselves are convincing, one must be cautious in the interpretation, since apparent discrepancies could arise from $w(z)$ histories outside the families considered in marginalization or from other violations of the underlying assumptions. To give two examples, "early dark energy" that is dynamically significant at high redshift could cause an apparent $G_9<1$, and decay of dark matter into dark energy could cause an apparent $\Delta\gamma>0$, since the value of $\Omega_m(z)/\Omega_m(z=0)$ would be higher than in the standard picture. Modified gravity could also give scale-dependent growth, which would produce deviations in the matter power spectrum away from the expected shape.

2.5. Overview of Methods

We conclude our "background" material with a short overview of the methods we will describe in detail over the next four sections.

Observations show that Type Ia supernovae have a peak luminosity that is tightly correlated with the shape of their light curves — supernovae that rise and fall more slowly have higher peak luminosity. The intrinsic dispersion around this relation is only about 0.15 mag, allowing each well observed supernova to provide an estimated distance with a 1σ uncertainty of about 8%. Surveys that detect tens or hundreds of Type Ia supernovae and measure their light curves and redshifts can therefore measure the distance-redshift relation $D(z)$ with high precision. Because the supernova luminosity is calibrated mainly by local observations of systems whose distances are inferred from their redshifts, supernova surveys effectively measure $D(z)$ in units of h^{-1} Mpc, not in absolute units independent of H_0.

Baryon acoustic oscillations provide an entirely independent way of measuring cosmic distance. Sound waves propagating before recombination imprint a characteristic scale on matter clustering, which appears as a local enhancement in the correlation funtion at $r \approx 150$ Mpc. Imaging surveys can detect this feature in the angular clustering of galaxies in bins of photometric redshift, yielding the angular diameter distance $D(z_{\rm phot})$. A spectroscopic survey over the same volume resolves the BAO feature in the line-of-sight direction and thereby yields a more precise $D(z)$ measurement. Furthermore, measuring the BAO scale in the line-of-sight direction allows a direct determination of $H(z)$. Other tracers of the matter distribution can also be used to measure BAO. Because the BAO scale is known in absolute units (based on straightforward physical calculation and parameter values well measured from the CMB), the BAO method measures $D(z)$ in absolute units — Mpc not h^{-1} Mpc — so BAO and supernova measurements to the same redshift carry different information.

The shapes of distant galaxies are distorted by the weak gravitational lensing of matter fluctuations along the line of sight. The typical distortion is only $\sim 0.5\%$, much smaller than the $\sim 30\%$ dispersion of intrinsic galaxy ellipticities, but by measuring the correlation of ellipticities as a function of angular separation, averaged over many galaxy pairs, one can infer the power spectrum of the matter fluctuations producing the lensing. Alternatively, one can measure the average elongation of background, lensed galaxies as a function of projected separation from foreground lensing galaxies to infer the galaxy-mass correlation function of the foreground sample, which can be combined with measurements of galaxy clustering to infer the matter clustering. By measuring the projected matter power spectrum for background galaxy samples at different z, weak lensing can constrain the growth function $G(z)$. However, the strength of lensing also depends on distances to the sources and lenses, so in practice the weak lensing method constrains combinations of $G(z)$ and $D(z)$.

Clusters of galaxies trace the high end of the halo mass function, typically $M \geq 10^{14} M_\odot$. Observationally, one measures the number of clusters as a function of a mass proxy, which directly constraints $dn/(d\ln M\, dV_c)$, where $dn/d\ln M$ is the halo mass function (eq. 37) and dV_c is the comoving volume element at the redshift of interest (eq. 11). The mass function at high M is exponentially sensitive to the amplitude of matter fluctuations, and therefore to $G(z)$, though this information is mixed with that in the cosmology dependence of the volume element $dV_c \propto D_A^2 H^{-1}$. Clusters can be identified in optical/near-IR surveys that find peaks in the galaxy distribution and measure their richness, in wide-area X-ray surveys that find extended sources and measure their X-ray luminosity and temperature, or in Sunyaev-Zel'dovich (SZ) surveys that find localized CMB decrements and measure their depth. The critical step in any cluster cosmology investigation is calibrating the relation between halo mass and the survey's cluster observable — richness, luminosity, temperature, SZ decrement — so that the mass function can be inferred from (or constrained by) the distribution of observables. We will argue in §**??** that the most reliable route to such calibration is via weak lensing, making wide-area optical or near-IR imaging a necessary component of any high-precision cosmic acceleration studies with clusters.

The next four sections, omitted here, give detailed discussions of Type Ia supernovae, BAO, weak lensing, and cluster abundances as probes of cosmic acceleration, including discussions of the statistical and systematic uncertainties in each method. Another section briefly summarizes a number of alternative probes, including precision measurement of H_0, redshift-space distortions, the Alcock-Paczynski test, scale-dependence of the growth factor, weak lensing tests of gravitational potentials, the integrated Sachs-Wolfe effect, and precision gravity tests.

3. A Balanced Program on Cosmic Acceleration

Having discussed many observational methods individually, we now turn to what we might hope to learn from them in concert. To the extent that this report has an underlying editorial theme, it is the value of a balanced observational program that pursues multiple techniques at comparable levels of precision. In our view, there is much more to be gained by doing a good job on three or four methods than by doing a maximal job on one at the expense of the others. This is *not* a "try everything" philosophy — moving forward from where we are today, an observational method is interesting only if it has reasonable prospects of achieving percent- or sub-percent-level errors, both statistical and systematic, on observables such as $H(z)$, $D(z)$, and $G(z)$. The successes of cosmic acceleration studies to date have raised the field's entry bar impressively high.

A balanced strategy is important both for cross-checking of systematics and for taking advantage of complementary information. Regarding systematics, the next generation of cosmic accleeration experiments seek much higher precision than those carried out to date, so the risk of being limited or biased by systematic errors is much higher. Most methods allow internal checks for systematics — e.g., comparing distinct populations of SNe, measuring angular dependence and tracer dependence of BAO signals, testing for B-modes and redshift-scaling of WL — but conclusions about cosmic acceleration will be far more convincing if they are reached independently by methods with different systematic uncertainties. Two methods only provide a useful cross-check of systematics if they have comparable statistical precision; otherwise a result found only in the more sensitive method cannot be checked by the less sensitive method.

Regarding information content, we have already emphasized the complementarity of SN and BAO as distance determination methods. SN have unbeatable statistical power at $z \lesssim 0.6$, while BAO surveys that map a large fraction of the sky with adequate sampling can achieve higher precision at $z \gtrsim 0.8$. Overlapping SN and BAO measurements provide independent physical information because the former measure relative distances and the latter absolute distances (h^{-1} Mpc vs. Mpc), and the value of h is itself a powerful dark energy diagnostic in the context of CMB constraints (see Figure 2, §2.4, and Hu 2005). WL, clusters, and redshift-space distortions provide independent constraints on expansion history, at levels that can be competitive with SN and BAO, and they provide sensitivity to structure growth. Without structure probes, we would have little hope of clues that might locate the origin of acceleration in the gravitational sector rather than the stress-energy sector, and we would, more generally, reduce the odds of "surprises" that might push us beyond our current theories of cosmic acceleration.

The primary purpose of this section is to present quantitative forecasts for a program of Stage IV dark energy experiments and to investigate how the forecast constraints depend on the performance of the individual components of such a program. Our forecasts are analogous to those of the DETF (Albrecht et al., 2006), updated with a more focused idea of what a Stage IV program might look like, and updated in light of subsequent work on parameterized models and figures of merit for dark energy experiments, most directly that of the JDEM FoM Science Working Group (Albrecht et al., 2009). In §3.1 we summarize our assumptions about the fiducial program. In §3.2 we describe the methodology of our forecasts, in particular the construction of Fisher matrices for the fiducial program. In §3.3 we present results for the fiducial program and for variants in which one or more components of this program are made significantly better or worse. We also compare these results to forecasts of a "Stage III" program represented by experiments now underway or nearing their first observations.

We have elected to focus on SN, BAO, and WL as the components of these forecasts, for two reasons. First, it is more straightforward (though still not easy) to define the expected statistical and systematic errors for these methods than for others. Second, the most promising alternative

methods — clusters, redshift-space distortions, and the Alcock-Paczynksi effect — will be enabled by the *same* data sets obtained for WL and BAO studies. It is therefore reasonable to view these as auxiliary methods that may improve the return from these data sets (perhaps by substantial factors) rather than as drivers for the observational programs themselves.

3.1. A Fiducial Program

As discussed in §1.3, Astro2010 and the European Astronet report have placed high priority on ground- and space-based dark energy experiments. The "Stage III" experiments currently underway will already allow much stronger tests of cosmic acceleration models, and "Stage IV" facilities built over the next decade should advance the field much further still.

For SN studies, we anticipate that Stage IV efforts will be limited not by statistical errors but by systematics associated with photometric calibration, dust extinction, and evolution of the SN population. For our fiducial program, we assume that SN surveys will achieve net errors (statistical + systematic) of 0.01 mag for the mean distance modulus in each of four redshift bins, with $\Delta z = 0.2$ and a maximum redshift $z_{\rm max} = 0.8$. We treat the bin-to-bin errors as uncorrelated, though this is clearly an approximation to systematic errors that are correlated at nearby redshifts and gradually decorrelate as one considers differing redshift ranges and observed-frame wavelengths. Even with 0.15 mag errors per SN, achieving this level of statistical error requires only 225 SNe per bin, and we expect that the error per SN can be reduced by working at red/IR wavelengths and by selecting sub-populations based on host galaxy type, spectral properties, and light curve shape. For purely ground-based efforts, we consider our 0.01 mag floor for systematic errors to be optimistic, given the challenges of dust extinction corrections and photometric calibration. However, a space-based program at rest-frame near-IR wavelengths, enabled by WFIRST, could plausibly achieve better than 0.01 mag systematics. We suspect that it will be hard to push calibration and evolution systematics below 0.005 mag even with WFIRST, and pushing statistical errors below this level begins to place severe demands on spectroscopic capabilities, unless purely photometric information can be used to identify populations with scatter below 0.1 mag per SN. We consider the impact of increasing $z_{\rm max}$ beyond 0.8, but the power of the SN program depends much more strongly on the magnitude error than on the maximum redshift.

For BAO, the primary metric of statistical constraining power is the total comoving volume mapped spectroscopically with a sampling density high enough to keep shot-noise sub-dominant. There are several projects in the planning stages that could map significant fractions of the comoving volume available out to $z \approx 3$. These include the near-IR spectroscopic components of Euclid and WFIRST, ground-based optical facilities such as BigBOSS, DEspec, and SuMIRE PFS, and radio intensity-mapping experiments. For our fiducial program, we assume that these projects will collectively map 25% of the comoving volume out to $z = 3$, with errors a factor of 1.8 larger than the linear theory cosmic variance errors.[14] We specifically assume full redshift coverage from $z = 0 - 3$ with $f_{\rm sky} = 25\%$ sky fraction, but other combinations of redshift coverage and $f_{\rm sky}$ that have the same total comoving volume yield similar results. The factor 1.8 accounts for imperfect sampling (hence non-negligible shot-noise) and for non-linear degradation of the BAO signal. It approximates the effects of sampling with $nP = 2$ and correcting (through reconstruction, §**??**) 50% but not 100% of the non-linear Lagrangian displacement of tracers. We implicitly assume that theoretical systematics associated with location of the BAO peak will remain below this level, an assumption we consider reasonable but not incontrovertible based on the discussion in §**??**.

[14] This is equivalent to assuming linear theory cosmic variance over a fractional volume $25\%/1.8^2 = 7.7\%$.

For WL, the primary metric of statistical constraining power is the total number of galaxies that have well measured shapes and good enough photometric redshifts to allow accurate model predictions and removal of intrinsic alignment systematics. For our fiducial case, we assume a survey of $10^4\,\mathrm{deg}^2$ achieving an effective surface density of 23 galaxies per arcmin^2 with $z_{\rm med} = 0.84$, corresponding to $I_{\rm AB} < 25$ and $r_{\rm eff} > 0.25''$. The effective galaxy number is 8.3×10^8. Euclid could likely achieve a higher surface density, though perhaps with a smaller survey area[15]. WFIRST could plausibly reach this surface density and survey area with a 2-2.5 year WL campaign. LSST will survey a larger area, and it might or might not achieve this effective surface density, depending on how low a value of $r_{\rm eff}/r_{\rm PSF}$ it can work to before shape measurements are systematics dominated. We compute constraints from cosmic shear in 14 bins of photometric redshift and from the shear-ratio test described in §**??**. but we do not incorporate higher order lensing statistics or galaxy-shear cross-correlations. We include information up to multipole $l_{\rm max} = 3000$, beyond which statistical power becomes limited at this surface density and systematic uncertainties associated with non-linear evolution and baryonic effects become significant.

Forecasting the systematic uncertainties in Stage IV WL experiments is very much a shot in the dark. Systematic errors are already comparable to statistical errors in surveys of $100\,\mathrm{deg}^2$, so lowering them to the level of statistical errors in a $10^4\,\mathrm{deg}^2$ survey that has higher galaxy surface density requires more than an order of magnitude improvement. We therefore consider a "fiducial" and an "optimistic" case for WL systematics. For the fiducial case, we incorporate (and marginalize over) aggregate uncertainties of 2×10^{-3} in shear calibration and 2×10^{-3} in the mean photo-z, with errors in each redshift bin larger by $\sqrt{14}$ but uncorrelated across bins. We also incorporate intrinsic alignment uncertainty as described by Albrecht et al. (2009, §2h), which includes marginalization over both GI and II components (see §**??**). For our "optimistic" case we adopt no specific form of the systematic errors but simply assume that they will double the statistical errors throughout. At an order of magnitude level, we can see that the optimistic case corresponds to a global fractional error $\sigma \sim 2N_{\rm mode}^{-1/2} \sim 2f_{\rm sky}^{-1/2} l_{\rm max}^{-1} = 1.3 \times 10^{-3}$, significantly lower than the fiducial case assumption of 2×10^{-3} errors for shear and photo-z calibration (which, roughly speaking, combine in quadrature to make a 2.8×10^{-3} multiplicative uncertainty).

3.2. Forecasting Constraints

The fiducial program outlined above provides a baseline for evaluating improvement in the determination of the cosmological parameters relative to current constraints. We use a Fisher matrix analysis to quantify this improvement and to study the complementarity of the main probes of cosmic acceleration. Since our knowledge of the exact design of future surveys and the systematic errors they will face is inherently imperfect, we also consider the effect of varying the precision of each technique in our forecasts, including both pessimistic and optimistic cases for SN, BAO, and WL data.

Determining the impact of each probe on our understanding of cosmic acceleration requires metrics for evaluating progress. The precision with which the dark energy equation of state (and its possible time dependence) can be measured is a common choice; while not the only quantity of interest, it is clearly a central piece of the puzzle. The DETF report (Albrecht et al., 2006) defined a "figure of merit" (FoM) for dark energy experiments based on the phenomenological model of equation (24) with parameters w_0 and w_a, and this has since become a standard tool for comparison of forecasts and current constraints. The DETF FoM is proportional to the inverse of

[15] At least if exposures are deep enough to reach the 25σ detection threshold we think is necessary to achieve accurate shape measurements see §**??**

the area of the 95% C.L. error ellipse for w_0 and w_a, after marginalization over the uncertainty in other parameters including spatial curvature. Since the constant of proportionality varies widely in practice, here we make the simple choice that the figure of merit expressed in terms of the equation of state at the "pivot" redshift (eq. 25) is given by

$$\mathrm{FoM} = \frac{1}{\sigma(w_p)\sigma(w_a)} \ . \tag{47}$$

The FoM indicates how well an experiment determines the dark energy equation of state and its slope at the pivot redshift and therefore indicates the ability to detect deviations from the standard ΛCDM model with $w_p = -1$ and $w_a = 0$.

While the DETF FoM is relatively simple to evaluate for a particular experiment, it omits much of the information that will be available from future experiments, including some potentially important clues to the nature of cosmic acceleration. For example, the true dark energy dynamics may be considerably more complicated than what the two-parameter linear model can accommodate, so that constraints on w_0 and w_a may yield incomplete or misleading results. Additionally, the equation of state alone is insufficient to describe the full range of possible alternatives to the standard cosmological model. For example, modified gravity theories can mimic the effect of any particular equation of state evolution on the Hubble expansion rate and the distance-redshift relation while altering the rate of growth of large-scale structure (Song et al., 2007). Including such possibilities requires extra parameters that describe changes in the growth history that are independent of equation of state variations. Other standard parameters of the cosmological model, such as the spatial curvature and the Hubble constant, are important due to degeneracies with the effects of cosmic acceleration that can limit the precision of constraints on the dark energy equation of state.

To include more general variations of the equation of state as well as altered growth of structure from modifications to GR on large scales, we adopt the parameterization of the JDEM Figure-of-Merit Science Working Group (FoMSWG; Albrecht et al. 2009). The equation of state in this parameterization is allowed to vary independently in each of 36 bins of width $\Delta a = 0.025$ extending from the present to $a = 0.1$ ($z = 9$). Specifically, the equation of state has a constant value of w_i at $(1 - 0.025i) < a < [1 - 0.025(i-1)]$, for $i = 1, \ldots, 36$. At earlier times, the equation of state is assumed to be $w = -1$, although the impact of this assumption is typically quite small since dark energy accounts for a negligible fraction of the total density at $z > 9$ in most models. Modifications to the linear growth function of GR $G_{\rm GR}(z)$ are included through the parameters G_9 and $\Delta\gamma$ as defined in equations (44) and (45). These parameters describe the change relative to GR in the normalization of the growth of structure at $z = 9$ and in the growth rate at $z < 9$, respectively. Adding these to the binned w_i values and the standard ΛCDM parameters, the full set is

$$\mathbf{p} = (w_1, \ldots, w_{36}, \ln G_9, \Delta\gamma, \Omega_m h^2, \Omega_b h^2, \Omega_k h^2, \Omega_\phi h^2, \ln A_s, n_s, \Delta\mathcal{M}) \ , \tag{48}$$

where the primordial amplitude A_s is defined at $k = 0.05\,\mathrm{Mpc}^{-1}$. $\Delta\mathcal{M}$ is an overall offset in the absolute magnitude scale of Type Ia supernovae. The Hubble constant is determined by these parameters through $h^2 = \Omega_m h^2 + \Omega_k h^2 + \Omega_\phi h^2$. We compute our forecasts at the fiducial parameter values chosen by FoMSWG to match CMB constraints from the 5-year release of WMAP data (Komatsu et al., 2009); these are listed in Table 2. These parameters are similar but not identical to those of the model used in §2 (Table 1), which used WMAP7. Note that spatially flat ΛCDM and GR are assumed for the fiducial model.

We use a Fisher matrix analysis to estimate the constraints on these parameters from the fiducial program defined in §3.1 and its variations. The Fisher matrix for each experiment consists of a model of the covariance matrix for the observable quantities and derivatives of these quantities with

Table 2 Fiducial Model for Forecasts

w_1	...	w_{36}	$\ln G_9$	$\Delta\gamma$	$\Omega_m h^2$	$\Omega_b h^2$	$\Omega_k h^2$	$\Omega_\phi h^2$	$\ln A_s$	n_s	$\Delta\mathcal{M}$
-1	...	-1	0	0	0.1326	0.0227	0	0.3844	-19.9628	0.963	0

respect to the parameters. We compute the latter numerically with finite differences and confirm the results using analytic expressions when possible.

We model SN data as measurements of the average SN magnitude in each of several redshift bins. While our fiducial case assumes that the net magnitude error is uncorrelated from one bin to the next, we also consider the impact of including a correlated component of the error by defining the SN covariance matrix as

$$C^{\rm SN}_{\alpha\beta} = \sigma^2_{m,u} \left(\frac{0.2}{\Delta z}\right) \delta_{\alpha\beta} + \sigma^2_{m,c} \exp\left(-\frac{|z_\alpha - z_\beta|}{\Delta z_c}\right) , \tag{49}$$

where Δz is the bin width, $\sigma_{m,u}$ is the uncorrelated error in a bin of width $\Delta z = 0.2$, $\sigma_{m,c}$ is the correlated error with correlation length Δz_c, and the net error in each bin z_α is $\sigma_m = \sqrt{\sigma^2_{m,u} + \sigma^2_{m,c}}$. In general these errors are redshift dependent, but here we assume that they are constant for simplicity. For the fiducial forecasts we take $\sigma_{m,c} = 0$, so the covariance matrix is diagonal. The SN Fisher matrix is then computed as a sum over redshift bins

$$F^{\rm SN}_{ij} = \sum_{\alpha,\beta} \frac{\partial m(z_\alpha)}{\partial p_i} (C^{\rm SN}_{\alpha\beta})^{-1} \frac{\partial m(z_\beta)}{\partial p_j} , \tag{50}$$

where $m(z_\alpha) = 5\log[H_0\langle D_L(z_\alpha)\rangle] + \mathcal{M}$ is the average magnitude in the bin and the derivatives are taken with respect to the parameters of equation (48).

For BAO, we divide the observed volume into bins of equal width in $\ln(1+z)$, assumed to be uncorrelated, and compute the Fisher matrix

$$F^{\rm BAO}_{ij} = \sum_{\mu,\nu,\alpha} \frac{\partial r_\mu(z_\alpha)}{\partial p_i} [C^{\rm BAO}_{\mu\nu}(z_\alpha)]^{-1} \frac{\partial r_\nu(z_\alpha)}{\partial p_j} , \tag{51}$$

where $\mathbf{r}(z_\alpha) = (D(z_\alpha)/s_*, H(z_\alpha)s_*)$ and s_* is the sound horizon at recombination (see §2.3), for which we use the fitting formula from Hu (2005),

$$s_* \approx (144.4\,{\rm Mpc}) \left(\frac{\Omega_m h^2}{0.14}\right)^{-0.252} \left(\frac{\Omega_b h^2}{0.024}\right)^{-0.083} . \tag{52}$$

We estimate the covariance matrix in each redshift bin using the BAO forecast code by Seo and Eisenstein (2007), which provides estimates of the fractional error on distance and the Hubble expansion rate at each redshift (relative to s_*), $\sigma_{\ln(D/s_*)} = \sqrt{C^{\rm BAO}_{11}}/(D/s_*)$ and $\sigma_{\ln(Hs_*)} = \sqrt{C^{\rm BAO}_{22}}/(Hs_*)$, respectively, as well as the cross correlation $r = C^{\rm BAO}_{12}/\sqrt{C^{\rm BAO}_{11}C^{\rm BAO}_{22}}$. For our default forecasts, we start with the linear theory cosmic variance predictions, corresponding to the limit of perfect sampling of the density field within the observed volume and no degradation of the signal due to nonlinear effects. To approximate the effects of finite sampling and nonlinearity, we increase these errors by a factor of 1.8 for our fiducial forecasts, which leads to parameter constraints comparable to what would be expected with sampling $nP = 2$ and reconstruction that halves the effects of nonlinear evolution. In Table 3 we list the volume for $f_{\rm sky} = 0.25$ and fiducial

Table 3 BAO Forecasts for the Fiducial Program

$z_{\rm min}$	$z_{\rm max}$	$V_{f_{\rm sky}=0.25}$ $[({\rm Gpc}/h)^3]$	$\sigma_{\ln(D/s_*)}$ [%]	$\sigma_{\ln(Hs_*)}$ [%]	r
0.000	0.072	0.010	13.386	21.881	0.409
0.072	0.149	0.075	4.895	8.002	0.409
0.149	0.231	0.217	2.873	4.697	0.409
0.231	0.320	0.449	1.997	3.265	0.409
0.320	0.414	0.781	1.515	2.476	0.409
0.414	0.516	1.218	1.213	1.983	0.409
0.516	0.625	1.761	1.009	1.649	0.409
0.625	0.741	2.407	0.863	1.410	0.409
0.741	0.866	3.148	0.754	1.233	0.409
0.866	1.000	3.970	0.672	1.098	0.409
1.000	1.144	4.860	0.607	0.992	0.409
1.144	1.297	5.799	0.556	0.909	0.409
1.297	1.462	6.770	0.514	0.841	0.409
1.462	1.639	7.758	0.481	0.785	0.409
1.639	1.828	8.745	0.453	0.740	0.409
1.828	2.031	9.718	0.429	0.702	0.409
2.031	2.249	10.664	0.410	0.670	0.409
2.249	2.482	11.576	0.393	0.643	0.409
2.482	2.732	12.443	0.379	0.620	0.409
2.732	3.000	13.261	0.368	0.601	0.409

BAO covariance matrix elements for 20 redshift slices from $0 \leq z \leq 3$. The results we obtain are only weakly dependent on the number of redshift bins chosen to divide up the total volume.

The forecasts for the main SN, BAO, and WL probes are supplemented by the expected constraints from upcoming CMB measurements provided by the Planck satellite. We adopt the Fisher matrix $\mathbf{F}^{\rm CMB}$ constructed by FoMSWG, which includes cosmological constraints from the 70, 100, and 143 GHz channels of Planck with $f_{\rm sky} = 0.7$, assuming that data collected at other frequencies will be used for foreground removal. The noise level and beam size for each channel comes from the Planck Blue Book (pla, 2006). Information from secondary anisotropies of the CMB is not included in this Fisher matrix; in particular, constraints from the ISW effect are removed by requiring the angular diameter distance to the CMB to be matched exactly, as described in Albrecht et al. (2009). Additionally, the large-scale ($\ell < 30$) polarization angular power spectrum and temperature-polarization cross power spectrum, which mainly contribute to constraints on the optical depth to reionization τ, are excluded from the forecast and replaced by a Gaussian prior with width $\sigma_\tau = 0.01$. This prior accounts for uncertainty in τ due to limited knowledge of the redshift dependence of reionization, which is not included in the simplest models of the CMB anisotropies. Although τ does not appear in the parameter set for the Fisher matrices, marginalization over τ in the CMB constraints contributes to the uncertainty on the primordial power spectrum amplitude A_s, which in turn affects predictions for the growth of large-scale structure.

Combined constraints on cosmological parameters are obtained simply by adding the Fisher matrices of the individual probes, i.e. $\mathbf{F} = \mathbf{F}^{\rm SN} + \mathbf{F}^{\rm BAO} + \mathbf{F}^{\rm WL} + \mathbf{F}^{\rm CMB}$. Then the forecast for the parameter covariance is $\mathbf{C} = \mathbf{F}^{-1}$, and in particular the uncertainty on a given parameter p_i after marginalizing over the error on all other parameters is $\sqrt{[\mathbf{F}^{-1}]_{ii}}$.

Computing the Fisher matrix in the FoMSWG parameter space with a large number of inde-

pendent bins for $w(z)$ gives us the flexibility to project these forecasts onto a number of simpler parameterizations, including the w_0–w_a model for the purposes of computing the FoM. To change from the original parameter set $\mathbf{p}$ to some new set $\mathbf{q}$, we compute

$$\tilde{F}_{kl} = \sum_{i,j} \frac{\partial p_i}{\partial q_k} F_{ij} \frac{\partial p_j}{\partial q_l} \,, \tag{53}$$

which gives the Fisher matrix $\tilde{\mathbf{F}}$ for the new parameterization. In particular, projection from bins w_i to w_0 and w_a involves the derivatives $\partial w_i/\partial w_0 = 1$ and $\partial w_i/\partial w_a = z/(1+z)$. We also compute the pivot redshift z_p and the uncertainty in the equation of state at that redshift, w_p. Given the 2×2 covariance matrix C_{ij} for w_0 and w_a (marginalized over the other parameters), the pivot values are computed as (Albrecht et al., 2009)

$$\begin{aligned} z_p &= -\frac{C_{12}}{C_{12}+C_{22}} \,, \\ \sigma_{w_p} &= C_{11} - \frac{C_{12}^2}{C_{22}} \,, \end{aligned} \tag{54}$$

where the first index corresponds to w_0 and the second to w_a.

One drawback to the w_0–w_a parameterization is that constraints on $w(z)$ at high redshift are coupled to those at low redshift by the form of the model; for example, if observations determine the value of the equation of state at $z = 0$ and at $z = 0.1$, then it is completely determined at high redshift even in the absence of high redshift data. To specifically address questions related to the ability of dark energy probes to constrain dark energy at low redshift vs. high redshift, we define an alternative but equally simple parameterization in which $w(z)$ takes constant, independent values in each of two bins at $z \le 1$ and $z > 1$. The projection onto this parameterization using equation (53) requires the derivatives $\partial w_i/\partial w(z \le 1) = \Theta(1 - z_i)$ and $\partial w_i/\partial w(z > 1) = 1 - \Theta(1 - z_i)$, where $\Theta(x)$ is the Heaviside step function equal to 0 for $x < 0$ and 1 for $x \ge 0$.

Principal components (PCs) of the dark energy equation of state provide another way to determine which features of the equation of state evolution are best constrained by a given combination of experiments (Huterer and Starkman, 2003; Hu, 2002; Huterer and Cooray, 2005; Wang and Tegmark, 2005; Dick et al., 2006; Simpson and Bridle, 2006; de Putter and Linder, 2008; Tang et al., 2008; Crittenden et al., 2009; Mortonson et al., 2009b; Kitching and Amara, 2009; Maturi and Mignone, 2009).

We compute the PCs for each forecast case by taking the total Fisher matrix for the original parameter set (eq. 48) and marginalizing over all parameters other than the 36 binned values of w_i. If we call the Fisher matrix for the w_i parameters $\mathbf{F}^w$, then the PCs are found by diagonalizing $\mathbf{F}^w$:

$$\mathbf{F}^w = \mathbf{Q}\mathbf{\Lambda}\mathbf{Q}^T \,, \tag{55}$$

where $\mathbf{Q}$ is an orthogonal matrix whose columns are eigenvectors of $\mathbf{F}^w$ and $\mathbf{\Lambda}$ is a diagonal matrix containing the corresponding eigenvalues of $\mathbf{F}^w$. Up to an arbitary normalization factor, the eigenvectors are equal to the PC functions $\mathbf{e}_i = (e_i(z_1), e_i(z_2), ...)$ which describe how the binned values of $w(z)$ are weighted with redshift. Here we adopt the normalization of Albrecht et al. (2009),

$$\sum_{k=1}^{36} e_i(z_k) e_j(z_k) = \sum_{k=1}^{36} e_k(z_i) e_k(z_j) = (\Delta a)^{-1} \delta_{ij} \,, \tag{56}$$

where $\Delta a = 0.025$ is the bin width; this condition approximately corresponds to $\int_{0.1}^{1} da [e_i(a)]^2 = 1$ for $i = j$ in the limit of a large number of redshift bins. With this convention, the columns of $\mathbf{Q}$

are $(\Delta a)^{1/2}\,\mathbf{e}_i$. The PCs rotate the original set of parameters to a set of PC amplitudes $\mathbf{Q}^T(\mathbf{1}+\mathbf{w})$ with elements

$$\beta_i = (\Delta a)^{1/2} \sum_{j=1}^{36} e_i(z_j)(1+w_j)\,. \tag{57}$$

Combining equations (56) and (57), we can construct $w(z)$ in each redshift bin from a given set of PC amplitudes as

$$w_i = -1 + \sum_{j=1}^{36} \alpha_j e_j(z_i)\,, \tag{58}$$

where $\alpha_i \equiv (\Delta a)^{1/2}\beta_i$. The accuracy with which the α_i can be determined from the data is given by the eigenvalues of $\mathbf{F}^w$, $\sigma_i \equiv \sigma_{\alpha_i} = (\Delta a/\Lambda_{ii})^{1/2}$, and the PCs are numbered in order of increasing variance (i.e. $\sigma_{i+1} > \sigma_i$).

For constraints that are marginalized over the w_i parameters, we impose a weak prior on w_i as suggested by Albrecht et al. (2009) to reduce the dependence of forecasts for $\Delta\gamma$ on the poorly-constrained high redshift w_i values, since arbitrarily large fluctuations in $w(z)$ can alter the high redshift growth rate. We include a weak Gaussian prior with width $\sigma_{w_i} = \Delta w/\sqrt{\Delta a}$ by adding to the total Fisher matrix

$$F_{ij}^{\rm prior} = \begin{cases} \sigma_{w_i}^{-2}\,\delta_{ij}\,, & i \le 36\,, \\ 0\,, & i > 36\,, \end{cases} \tag{59}$$

assuming that the parameters are ordered as in equation (48) with $p_1 = w_1$, $p_2 = w_2$, etc. For most forecasts, we use a default prior width of $\Delta w = 10$ ($\sigma_{w_i} \approx 63$), which approximately corresponds to requiring that the average value of $|1+w|$ in all bins does not exceed 10. In the next section we also consider how constraints on certain parameters change with a narrower prior of $\Delta w = 1$. For priors wider than the default choice, the Fisher matrix computations are subject to numerical effects arising from the use of a finite number of w_i bins to approximate continuous variations in $w(z)$, so we do not present results with weaker priors than $\Delta w = 10$. Note that the construction of PCs of $w(z)$ as described above does not include such a prior on w_i.

Table 4 Key to forecast variations.

Any $\times 4$	Quadruple fiducial errors (divide Fisher matrix by 16).
Any $\times 2$	Double fiducial errors (divide Fisher matrix by 4).
Any/2	Halve fiducial errors (multiply Fisher matrix by 4).
SN-III	Stage III-like SN: total magnitude error of 0.03 per $\Delta z = 0.2$ bin over $0 \le z \le 0.8$.
SN$z_{\rm max}$	Increase max. redshift to $z_{\rm max} = 1.6$ (8 bins with $\Delta z = 0.2$ and 0.01 mag. error).
SN$z_{\rm min}$	Increase min. redshift to $z_{\rm min} = 0.2$ (3 bins with $\Delta z = 0.2$ and 0.01 mag. error).
SNcx	Correlated errors: $\sigma_{m,u} = \sigma_{m,c} = 0.007$, $\Delta z_c = 0.2$, with x bins over $0 \le z \le 0.8$.
BAO-III	Stage III-like BAO, approximating forecasts for BOSS LRGs+HETDEX: $(D/s_*, Hs_*)$ errors of $(1.0\%, 1.8\%)$ at $z = 0.35$, $(1.0\%, 1.7\%)$ at $z = 0.6$, and $(0.8\%, 0.8\%)$ at $z = 2.4$.
BAO$z_{\rm max}$	Reduce maximum redshift to $z_{\rm max} = 2$ (20 bins), retaining $f_{\rm sky} = 0.25$
WL-opt	"Optimistic" Stage IV case (total error= $2\times$ statistical).
WL-III	Stage III-like WL, approximating forecasts for DES:
CMB-W9	Fisher matrix forecast for 9-year WMAP data.

Table 5 Forecast uncertainties on parameters, varying a single probe at a time from the fiducial specifications. With the exception of $w(z > 1)$, a w_0–w_a model for the dark energy equation of state is assumed.

	Forecast case	z_p	σ_{w_p}	FoM	$\sigma_{w(z>1)}$	$10^3\,\sigma_{\Omega_k}$	$10^2\,\sigma_h$	$\sigma_{\Delta\gamma}$	$\sigma_{\ln G_9}$
1	[SN,BAO,WL,CMB]	0.51	0.015	533	0.052	0.55	0.61	0.034	0.015
2	[SN,BAO,WL-opt,CMB]	0.43	0.013	687	0.049	0.64	0.47	0.026	0.016
3	[BAO,WL,CMB]	0.63	0.017	321	0.054	0.56	0.99	0.034	0.015
4	[SN-III,BAO,WL,CMB]	0.61	0.017	351	0.054	0.56	0.91	0.034	0.015
5	[SN×4,BAO,WL,CMB]	0.62	0.017	338	0.054	0.56	0.94	0.034	0.015
6	[SN×2,BAO,WL,CMB]	0.59	0.016	385	0.053	0.56	0.83	0.034	0.015
7	[SN/2,BAO,WL,CMB]	0.38	0.011	903	0.050	0.55	0.37	0.034	0.015
8	[SN$z_{\max}$,BAO,WL,CMB]	0.46	0.012	690	0.051	0.55	0.47	0.034	0.015
9	[SN$z_{\min}$,BAO,WL,CMB]	0.61	0.017	356	0.053	0.56	0.90	0.034	0.015
10	[SNc4,BAO,WL,CMB]	0.51	0.015	534	0.052	0.55	0.60	0.034	0.015
11	[SNc8,BAO,WL,CMB]	0.48	0.014	604	0.051	0.55	0.54	0.034	0.015
12	[SNc16,BAO,WL,CMB]	0.47	0.014	632	0.051	0.55	0.52	0.034	0.015
13	[SN,WL,CMB]	0.30	0.025	107	0.32	2.2	0.79	0.039	0.023
14	[SN,BAO-III,WL,CMB]	0.38	0.021	224	0.12	1.2	0.68	0.035	0.017
15	[SN,BAO×4,WL,CMB]	0.35	0.023	180	0.15	1.2	0.74	0.037	0.018
16	[SN,BAO×2,WL,CMB]	0.42	0.020	289	0.088	0.76	0.69	0.035	0.016
17	[SN,BAO/2,WL,CMB]	0.53	0.010	1070	0.033	0.47	0.45	0.034	0.014
18	[SN,BAO$z_{\max}$,WL,CMB]	0.47	0.015	427	0.072	0.66	0.63	0.034	0.015
19	[SN,BAO,CMB]	0.47	0.017	427	0.059	0.78	0.64	—	—
20	[SN,BAO,WL-III,CMB]	0.47	0.017	432	0.059	0.77	0.63	0.15	0.048
21	[SN,BAO,WL×4,CMB]	0.48	0.017	439	0.058	0.75	0.63	0.13	0.031
22	[SN,BAO,WL×2,CMB]	0.49	0.016	467	0.056	0.68	0.63	0.065	0.020
23	[SN,BAO,WL/2,CMB]	0.52	0.013	671	0.048	0.45	0.55	0.018	0.012
24	[SN,BAO,WL]	0.37	0.022	293	0.076	7.9	1.3	0.037	6.70
25	[SN,BAO,WL,CMB-W9]	0.48	0.016	473	0.056	1.1	0.63	0.037	0.019

Table 6 Same as Table 5, but varying two or three probes at a time from the fiducial specifications.

	Forecast case	z_p	σ_{w_p}	FoM	$\sigma_{w(z>1)}$	$10^3\,\sigma_{\Omega_k}$	$10^2\,\sigma_h$	$\sigma_{\Delta\gamma}$	$\sigma_{\ln G_9}$
1	[SN,BAO,WL,CMB]	0.51	0.015	533	0.052	0.55	0.61	0.034	0.015
2	[SN-III,BAO-III,WL-III,CMB]	0.54	0.038	82	0.146	1.36	1.46	0.148	0.051
3	[SN-III,BAO-III,WL-III,CMB-W9]	0.45	0.048	58	0.181	2.42	1.49	0.149	0.064
4	[SN×4,BAO×4,WL×4,CMB]	0.57	0.051	42	0.183	1.34	2.40	0.128	0.033
5	[SN×2,BAO×2,WL×2,CMB]	0.54	0.027	151	0.096	0.85	1.20	0.065	0.021
6	[SN/2,BAO/2,WL/2,CMB]	0.49	0.008	1951	0.027	0.34	0.31	0.018	0.012
7	[SN-III,BAO-III,WL,CMB]	0.52	0.029	115	0.131	1.20	1.26	0.035	0.017
8	[SN×4,BAO×4,WL,CMB]	0.52	0.035	74	0.158	1.19	1.66	0.037	0.019
9	[SN×4,BAO×2,WL,CMB]	0.59	0.026	140	0.094	0.77	1.38	0.035	0.016
10	[SN×4,BAO/2,WL,CMB]	0.57	0.011	879	0.033	0.47	0.54	0.034	0.014
11	[SN×2,BAO×4,WL,CMB]	0.45	0.031	104	0.153	1.18	1.20	0.037	0.019
12	[SN×2,BAO×2,WL,CMB]	0.53	0.024	180	0.092	0.76	1.08	0.035	0.016
13	[SN×2,BAO/2,WL,CMB]	0.56	0.011	920	0.033	0.47	0.52	0.034	0.014
14	[SN/2,BAO×4,WL,CMB]	0.29	0.014	352	0.143	1.16	0.46	0.036	0.018
15	[SN/2,BAO×2,WL,CMB]	0.32	0.013	537	0.085	0.76	0.41	0.035	0.016
16	[SN/2,BAO/2,WL,CMB]	0.44	0.009	1522	0.032	0.47	0.32	0.034	0.014
17	[SN$z_{\max}$,BAO$z_{\max}$,WL,CMB]	0.44	0.013	554	0.070	0.66	0.50	0.034	0.015

Table 7 Continuation of Table 6.

	Forecast case	z_p	σ_{w_p}	FoM	$\sigma_{w(z>1)}$	$10^3\,\sigma_{\Omega_k}$	$10^2\,\sigma_h$	$\sigma_{\Delta\gamma}$	$\sigma_{\ln G_9}$
1	[SN,BAO,WL,CMB]	0.51	0.015	533	0.052	0.55	0.61	0.034	0.015
2	[SN,BAO-III,WL-III,CMB]	0.35	0.025	178	0.131	1.35	0.71	0.147	0.051
3	[SN,BAO×4,WL×4,CMB]	0.33	0.026	135	0.166	1.31	0.84	0.128	0.033
4	[SN,BAO×4,WL×2,CMB]	0.33	0.025	146	0.161	1.27	0.81	0.067	0.023
5	[SN,BAO×4,WL/2,CMB]	0.40	0.018	285	0.117	0.98	0.63	0.020	0.014
6	[SN,BAO×2,WL×4,CMB]	0.41	0.022	247	0.093	0.90	0.74	0.127	0.032
7	[SN,BAO×2,WL×2,CMB]	0.41	0.021	257	0.091	0.85	0.73	0.065	0.021
8	[SN,BAO×2,WL/2,CMB]	0.45	0.016	393	0.079	0.67	0.61	0.019	0.013
9	[SN,BAO/2,WL×4,CMB]	0.46	0.012	802	0.041	0.65	0.46	0.126	0.031
10	[SN,BAO/2,WL×2,CMB]	0.48	0.012	878	0.038	0.59	0.46	0.064	0.020
11	[SN,BAO/2,WL/2,CMB]	0.57	0.009	1405	0.028	0.34	0.42	0.018	0.012
12	[SN-III,BAO,WL-III,CMB]	0.59	0.020	273	0.061	0.77	0.99	0.146	0.048
13	[SN×4,BAO,WL×4,CMB]	0.61	0.020	263	0.060	0.75	1.05	0.126	0.031
14	[SN×4,BAO,WL×2,CMB]	0.61	0.019	284	0.058	0.68	1.02	0.065	0.021
15	[SN×4,BAO,WL/2,CMB]	0.59	0.014	472	0.049	0.45	0.77	0.018	0.012
16	[SN×2,BAO,WL×4,CMB]	0.57	0.019	307	0.060	0.75	0.90	0.126	0.031
17	[SN×2,BAO,WL×2,CMB]	0.58	0.018	329	0.057	0.68	0.88	0.065	0.020
18	[SN×2,BAO,WL/2,CMB]	0.58	0.014	518	0.049	0.45	0.70	0.018	0.012
19	[SN/2,BAO,WL×4,CMB]	0.35	0.013	753	0.056	0.74	0.38	0.126	0.031
20	[SN/2,BAO,WL×2,CMB]	0.36	0.012	800	0.054	0.67	0.38	0.065	0.020
21	[SN/2,BAO,WL/2,CMB]	0.41	0.010	1084	0.046	0.44	0.35	0.018	0.012

3.3. Results: Forecasts for the Fiducial Program and Variations

3.3.1. Constraints in simple $w(z)$ models

We begin with forecasts for which the 36 $w(z)$ bins are projected onto the simpler w_0–w_a parameter space. Tables 4–7 give the forecast 1σ uncertainties for the fiducial program and several variations. Each forecast case is labeled by a list of the Fisher matrices that are added together, and the basic variations we consider are simple rescalings of the *total* errors for each probe; for example, [SN/2,BAO×4,WL-opt,CMB] includes the fiducial SN data with the total error halved (i.e. the Fisher matrix multiplied by 4), 4 times the fiducial BAO errors, the optimistic version of the WL forecast, and the fiducial Planck CMB Fisher matrix. Note that /2 denotes a *more* powerful program and ×2 denotes a *less* powerful program. The key in Table 4 describes other types of variations of the fiducial probes. In some cases we omit a probe entirely, e.g. [SN,BAO,WL] sums the fiducial Fisher matrices of the three main probes but does not include the Planck CMB priors. Note that even though we assume a specific systematic error component in computing certain Fisher matrices (in particular, $\mathbf{F}^{\rm WL}$), the cases with rescaled errors simply multiply each Fisher matrix by a constant factor and thus do not distinguish between statistical and systematic contributions to the total error.

Constraints on the equation of state are given in Tables 5–7 by the DETF FoM and the error on w_p. The rule of thumb that $\sigma_{w_a} \equiv ({\rm FoM} \times \sigma_{w_p})^{-1} \approx 10\sigma_{w_p}$ holds at the $\sim 30\%$ level for most of the forecast variations we consider — i.e., at the best-constrained redshift, the value of w is typically determined a factor of ten better than the value of its derivative. The forecast tables also list the uncertainty in the high redshift equation of state $w(z > 1)$ for the alternative parameterization where $w(z)$ takes independent, constant values at $z \le 1$ and $z > 1$. Note that all of these $w(z)$ constraints are marginalized over uncertainties in G_9 and $\Delta\gamma$, so they do *not* assume that structure growth follows the GR prediction.

For the fiducial program outlined in §3.1, the DETF FoM is projected to be around 500–700, depending on whether the WL forecast uses the default systematic error model or the optimistic model. This is roughly an order of magnitude larger than the FoM forecasted for a combination of Stage III experiments (e.g. see Table 6, rows 2–3) and nearly two orders of magnitude larger than current, "Stage II" FoM values (~ 10). The equation of state in the w_0–w_a parameterization is best measured by the fiducial set of Stage IV experiments at a redshift $z_p \approx 0.5$ with a 1σ precision of $\sigma_{w_p} \approx 0.014$, and the time variation of $w(z)$ is determined to within $\sigma_{w_a} \approx 0.12$. The fiducial program also yields impressive constraints of 5.5×10^{-4} on Ω_k and 0.61 km s^{-1} Mpc^{-1} on H_0. Forecast 1σ errors for the modified gravity parameters are 0.034 on $\Delta\gamma$ and 0.015 on $\ln G_9$. We caution, however, that the Ω_k, H_0, and G_9 errors (but not the $\Delta\gamma$ error) are sensitive to our assumption of the w_0–w_a parameterization (see Figures 8–12 below). CMB constraints make a critical contribution — the FoM drops from 533 to 293 if they are omitted entirely (Table 5, line 24) — but the difference between *Planck* precision and anticipated WMAP9 precision is modest (line 25).

Figure 5 illustrates the key results of our forecasting investigation, highlighting many aspects of the interplay among the three observational probes. In the upper left panel, the solid curve shows how the FoM changes as the total SN errors vary from four times fiducial to half fiducial, keeping the other probes (BAO, WL, and CMB) fixed at their fiducial levels. Other curves show the effect of doubling WL or BAO errors or switching to the optimistic WL forecast. The lower panels show analogous results from varying the BAO or WL errors, while the upper right panel shows the effect of changing the maximum redshift of the SN program. Over the range of variations plotted in Figure 5, the FoM varies from barely 100 to over 1000.

One notable trend in the FoM scaling is that it is not uniform among the three main probes.

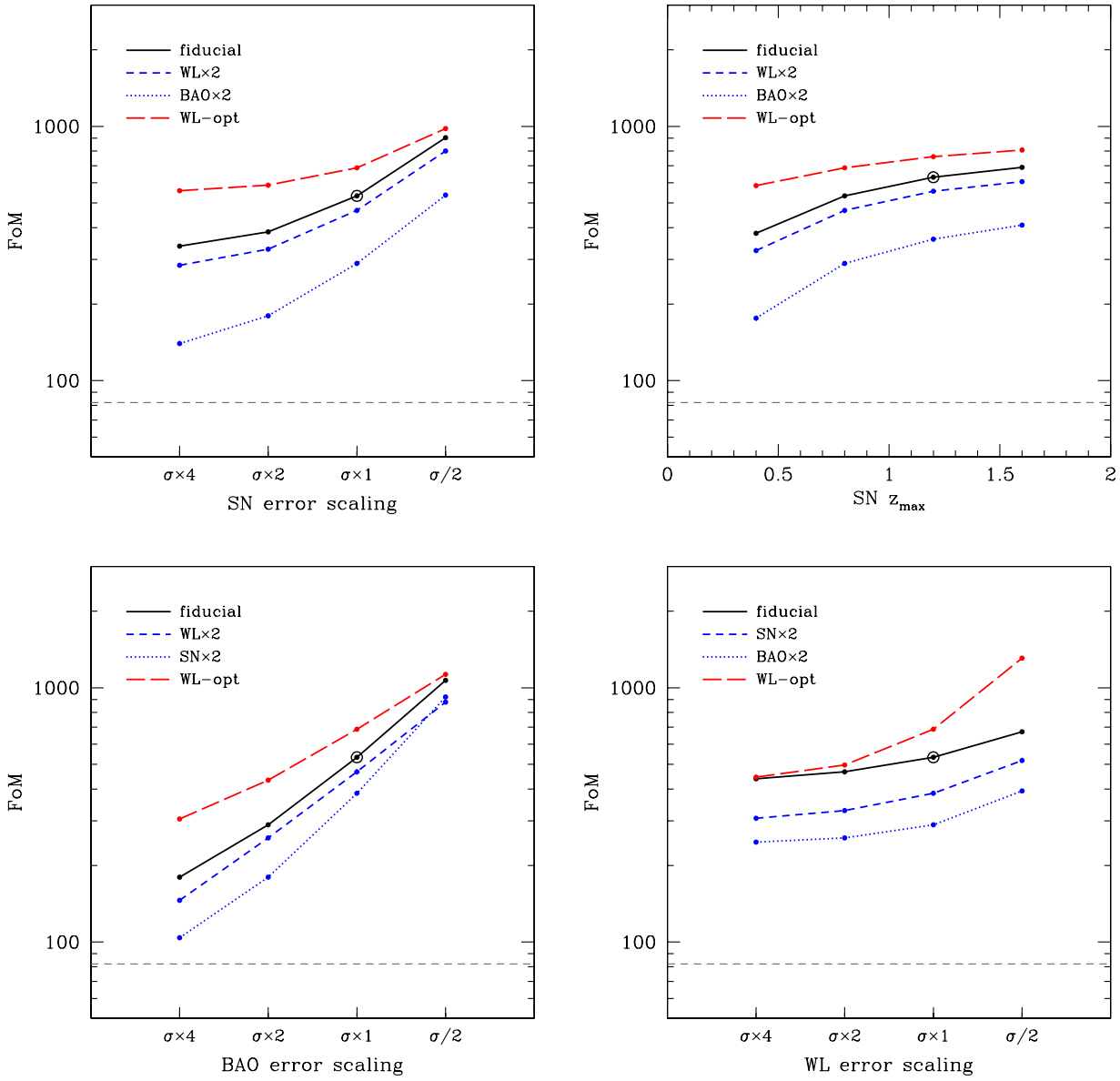

Figure 5 The DETF FoM, $(\sigma_{w_p}\sigma_{w_a})^{-1}$, for the fiducial program and simple variants. In each panel, the open circle marks the FoM of the fiducial program. In the upper left panel, the other points along the solid curve show the effect of scaling the error on the SN measurements by factors of 2 or 4 while keeping errors for other probes fixed at their fiducial values. Dotted, short-dashed, and long-dashed curves show the effect of, respectively, doubling the BAO errors, doubling the WL errors, or adopting in the optimistic WL forecasts in which systematic errors are simply twice the statistical errors. Other panels show analogous results, but instead of scaling the total SN error they scale the total BAO error (lower left), the total WL error (lower right), or the maximum redshift of the SN constraints (upper right). In each panel, the dashed gray line marks the forecast performance of Stage III probes (including Planck) with FoM=82.

Starting from the fiducial program, the effect of doubling or halving errors is greater for BAO than for SN, and greater for SN than for WL. This scaling implies that BAO data provide the greatest leverage in these forecasts. However, the hierarchy of the three probes is sensitive to the assumptions about each experiment; in particular, assuming the optimistic version of WL errors promotes WL from having the least leverage on the FoM to having the most leverage. More generally, the fact that varying the errors of any individual probe changes the FoM noticeably demonstrates the complementarity of the methods.

Unlike many previous FoM forecasts, we marginalize over the structure growth parameters $\Delta\gamma$ and $\ln G_9$, which tends to increase the uncertainties on w_0 and w_a. In most cases, the difference between the marginalized constraints and ones obtained under the assumption of GR ($\Delta\gamma = \ln G_9 = 0$) is small, but the difference is greater if WL contributes significantly to expansion history constraints; for example, for the fiducial program, the change in the FoM due to assuming GR is only $533 \rightarrow 621$, whereas with the WL-opt forecast the change is $687 \rightarrow 979$.

For SN observations, it is interesting to ask whether it is better to go after SNe at high redshifts or to focus on reducing the errors on SN data at low redshifts. Comparing the upper panels of Figure 5, we find that the benefit from reducing errors is typically greater than that from obtaining SNe beyond $z \sim 1$, at least for the FoM. For example, reducing the error per redshift bin from 0.01 mag (the fiducial value) to 0.005 mag raises the FoM by a factor of 1.69, but increasing the maximum redshift from 0.8 to 1.6 raises the FoM by only 1.29 (see Table 5). If BAO errors are doubled, the FoM drops substantially, but SN errors still have much greater leverage than SN maximum redshift. We have assumed in these forecasts that the error per redshift bin stays constant as the maximum SN redshift increases, but in reality higher redshift SNe are likely to have larger systematic errors associated with them, which would diminish the gains from high redshift SNe even more than indicated by the flattening of curves in Figure 5.

The weak dependence of $w(z)$ constraints on the maximum SN redshift extends to other parameters as well. Figure 6 compares the effect on 1σ errors of varying the maximum SN redshift to that of varying the maximum BAO redshift. For the w_0–w_a model, the errors on all parameters are relatively insensitive to changes in the maximum SN redshift at $z \gtrsim 1$, but the errors on w_a and Ω_k decrease by a factor of a few as the maximum BAO redshift increases from $z = 1$ to $z = 3$. Likewise, the high redshift equation of state $w(z > 1)$ can be determined much more precisely as BAO data extend to higher redshifts, but it depends little on the maximum SN redshift. For the fiducial Stage IV forecasts, only the Hubble constant error depends significantly on the depth of SN observations (assuming a w_0–w_a model). More pessimistic assumptions about the achievable BAO errors enhance the importance of high redshift SNe for determining w_p (dotted line in Figure 6), but the dependence of other parameters on $z_{\rm max}$ for the SN data remains weak.

3.3.2. Constraints on structure growth parameters

While the DETF FoM is a useful metric for studying the impact of variations in each of the dark energy probes, it does not tell the whole story. Deviations from the standard model might show up in other sectors of the parameter space; for example, a detection of non-GR values for the growth parameters $\Delta\gamma$ and G_9 could point to a modified gravity explanation for cosmic acceleration that would not be evident from measurements of $w(z)$ alone. Thus, even the less optimistic version of the WL experiment, which adds relatively little to the $w(z)$ constraints obtained by the combination of fiducial SN, BAO, and CMB forecasts, is a critical component of a program to study cosmic acceleration because of its unique role in determining the growth parameters $\Delta\gamma$ and G_9.

The impact of various experiments on the structure growth parameters is more evident if we extend the DETF FoM to include $\Delta\gamma$ in addition to w_0 and w_a. As shown in Figure 7, the scaling of this new FoM with respect to WL errors (and, to a lesser extent, BAO errors) is much steeper

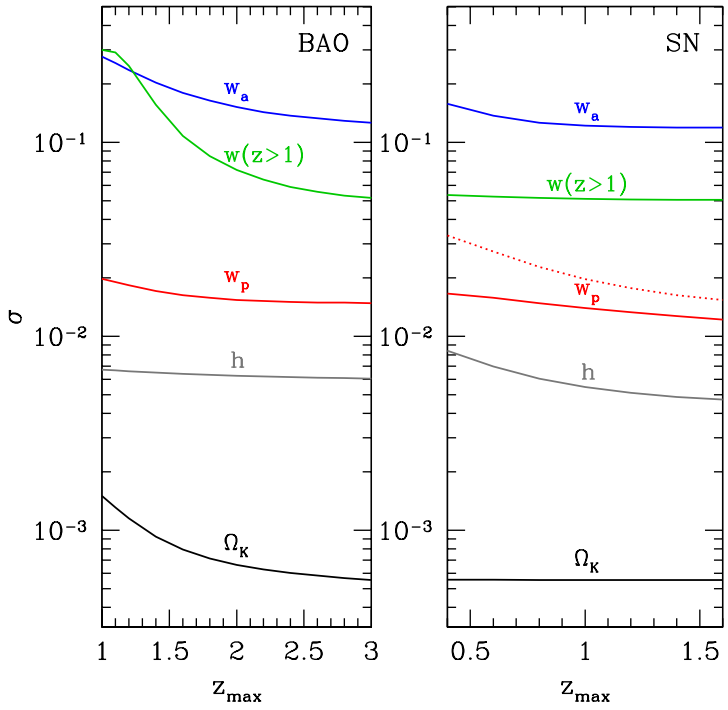

Figure 6 Variation of 1σ parameter errors with the maximum redshift for BAO (left) or SN data (right). For the solid curves, fiducial Stage IV forecasts are assumed for all other probes. The dotted curve in the right panel shows the scaling of $\sigma(w_p)$ with SN $z_{\rm max}$ assuming 4 times larger BAO errors (BAO×4). The plotted errors assume a w_0–w_a parametrization (except for $w(z>1)$).

than it is for the usual FoM (Figure 5). We do not show the scaling with SN errors or $z_{\rm max}$ since those assumptions do not affect the expected uncertainties for $\Delta\gamma$ and G_9 (see Table 5, lines 3–12). One could also consider versions of the FoM that include uncertainties in G_9 and that account for the correlations between the structure growth parameters and the dark energy equation of state.

The complementarity between the SN, BAO, and WL techniques is further demonstrated by the contours in Figures 8–10, which show the forecast 68% confidence level contours in the $w_{0.5}$–w_a and $\Delta\gamma$–$\ln G_9$ planes after marginalizing over other parameters. Instead of w_0 we plot $w_{0.5}$, the equation-of-state parameter at $z = 0.5$, because it is much less correlated with w_a for most of the forecast scenarios. In every panel, the blue ellipse shows the error contour of the fiducial forecast while other ellipses show the effect of varying the errors of the indicated method. The opposite orientation of ellipses in Figures 8 and 9 demonstrates the complementary sensitivity of SN and BAO to $w(z)$: the SN data are mainly sensitive to the equation of state at low redshift, whereas BAO data measure the equation of state at higher redshift. However, the sensitivity to the beyond-GR growth parameters comes entirely from WL data, which provide the only direct measurements of growth, and the strength of the $\Delta\gamma$ and G_9 constraints depends directly on the WL errors, as shown in Figure 10. Conversely, these constraints are very weakly sensitive to the SN or BAO errors (Figs. 8 and 9), showing that the uncertainties are dominated by the growth measurements themselves rather than residual uncertainty in the expansion history. Inspection of Table 5 shows that the $\Delta\gamma$ constraints are essentially linear in the WL errors, while the $\ln G_9$ constraints scale more slowly.

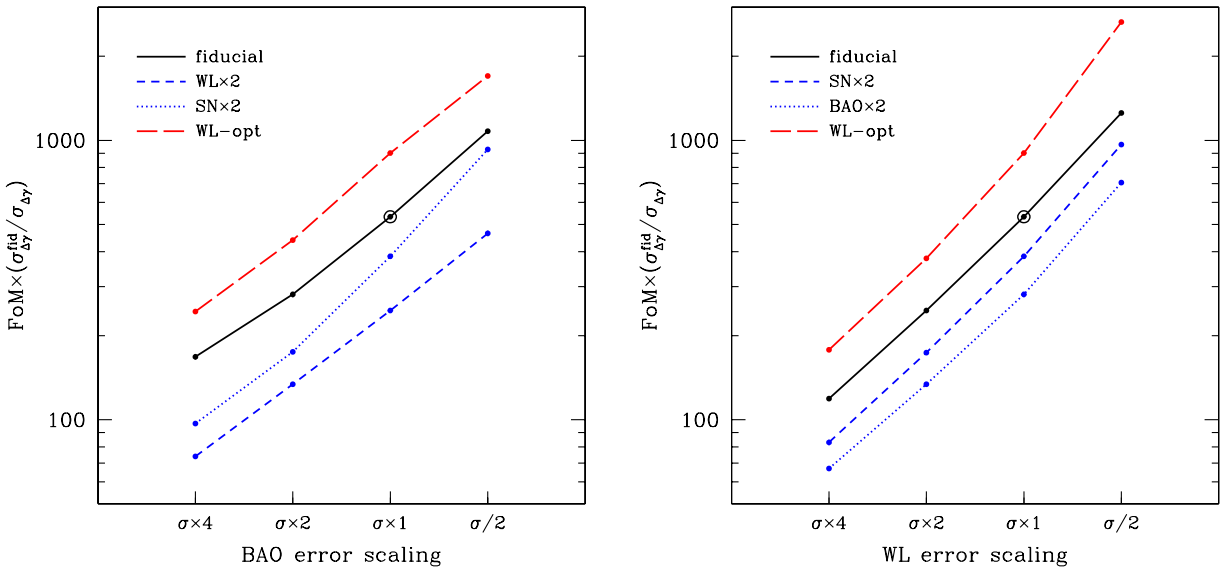

Figure 7 FoM scaling with BAO errors (left) and WL errors (right) including changes in the error on $\Delta\gamma$, normalized to the forecast uncertainty for the fiducial program, $\sigma^{\rm fid}_{\Delta\gamma} = 0.034$. The fiducial Stage IV forecast is marked by an open circle. For the Stage III forecast, FoM$\times(\sigma^{\rm fid}_{\Delta\gamma}/\sigma_{\Delta\gamma}) = 19$.

Although the w_0–w_a parameterization is flexible enough to describe a wide variety of expansion histories, it is too simple to account for all possibilities; in particular, $w(z)$ is restricted to functions that are smooth and monotonic over the entire history of the universe. Because many cosmological parameters are partially degenerate with the dark energy evolution, assumptions about the functional form of $w(z)$ can strongly affect the precision of constraints on other parameters. As an example of this model dependence, the right panels of Figures 8–10 show how the constraints on the growth parameters weaken (dashed curves) if one allows the 36 binned w_i values to vary independently instead of assuming that they conform to the w_0–w_a model. While $\Delta\gamma$ forecasts are only mildly affected by the choice of dark energy modeling, constraints on the $z = 9$ normalization parameter G_9 depend strongly on the form of $w(z)$. This dependence follows from the absence of data probing redshifts $3 \lesssim z < 9$ in the fiducial Stage IV program. In the w_0–w_a model, dark energy evolution is well determined even at high redshifts, since the two parameters of the model can be measured from data at $z < 3$, and thus the growth function at $z = 9$ is closely tied to the low redshift growth of structure measured by WL. However, allowing $w(z)$ to vary independently at high redshift where it is unconstrained by data decouples the low and high redshift growth histories, and therefore G_9 can no longer be determined precisely. In fact, the constraints on G_9 in that case depend greatly on the chosen prior on w_i (taken to be the default prior of $\sigma_{w_i} = 10/\sqrt{\Delta a}$ in Figures 8–10). One important consequence of this dependence on the $w(z)$ model is that an apparent breakdown of GR via $G_9 \neq 1$ might instead be a sign that the chosen dark energy parameterization is too restrictive.

3.3.3. Dependence on $w(z)$ model and binning of data

Other parameters are also affected to varying degrees by the choice of $w(z)$ model and the priors on the model parameters. Figure 11 shows how errors on Ω_k and h are affected by relaxing assumptions about dark energy evolution. For the fiducial program and minor variants, Ω_k is very

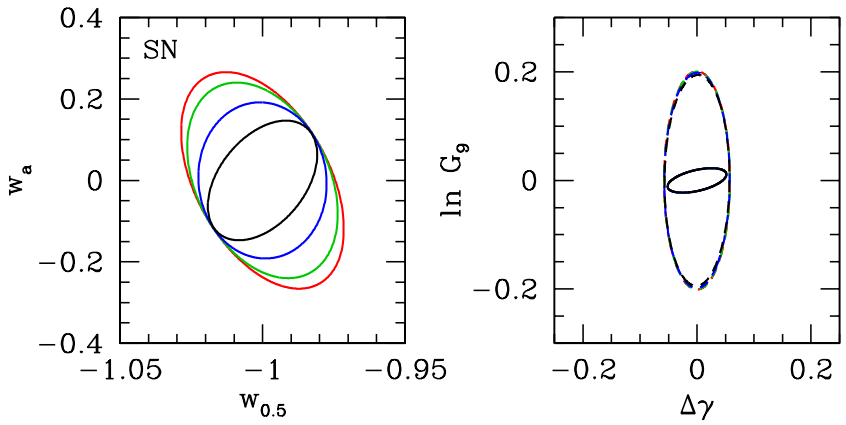

Figure 8 Forecasts (68% confidence levels) for dark energy and growth parameters, varying errors on SN data: fiducial×4 (red), ×2, (green), ×1 (blue), and /2 (black). In all cases, the fiducial forecasts are used for the other probes (BAO, WL, CMB). Contours in the left panel use the value of the equation of state at $z = 0.5$ (close to the typical pivot redshift), $w_{0.5} = w_0 + w_a/3$. Dashed contours in the right panel show the errors on growth parameters for the original, binned $w(z)$ parametrization, with the default priors corresponding to deviations of $\lesssim 10$ in the average value of w. Solid contours assume a w_0–w_a parametrization.

weakly correlated with w_0 and w_a, resulting in similar errors on curvature for the w_0–w_a and ΛCDM models. However, generalizing the dark energy parameterization to include independent variations in 36 redshift bins can degrade the precision of Ω_k measurements by an order of magnitude or more. In that case, the error on Ω_k is very sensitive to the chosen prior on the value of w_i in each bin, and it improves little as the BAO errors decrease. This dependence on priors reflects the fact that curvature is most correlated with the highest redshift w_i values, which are poorly constrained by the fiducial combination of data. Relative to curvature, constraints on the Hubble constant are affected more by the choice of dark energy parameterization but less by priors on w_i in the binned $w(z)$ model.

Figure 12 shows the dependence of σ_h on the precision of SN data for various dark energy parameterizations (σ_{Ω_k} is nearly independent of the SN errors for this range of variations around the fiducial forecast; see Table 5). In the left and right panels we compare forecasts with the same total number of SNe at $z < 0.8$ but divided into different numbers of redshift bins (4 and 16 for the left and right panels, respectively). Since it is unrealistic to expect that SN constraints in different redshift bins remain independent as the bin width decreases, we include the correlated error term in equation (49), with $\sigma_{m,u} = \sigma_{m,c} = 0.007$ and $\Delta z_c = 0.2$, so that the total error in each redshift bin of width 0.2 is 0.01 as in the fiducial SN forecast. These SN forecasts with redshift correlations correspond to the cases labeled "SNc4" and "SNc16" in Table 5. Note that parameter errors from the SNc4 forecasts are nearly the same as the default forecasts with four uncorrelated SN bins (e.g. compare rows 1 and 10 in Table 5).

If we assume a w_0–w_a model for dark energy, Hubble constant errors strongly depend on the precision of SN data. However, the left panel of Figure 12 shows that either decreasing or increasing the number of dark energy parameters can almost completely eliminate the dependence of σ_h on the SN data. In the case of the simpler ΛCDM model, the combination of the fiducial BAO, WL, and CMB forecasts is sufficient to precisely determine all of the model parameters, and adding information from SN data has a negligible effect on the parameter errors. Adding w_0 and w_a to

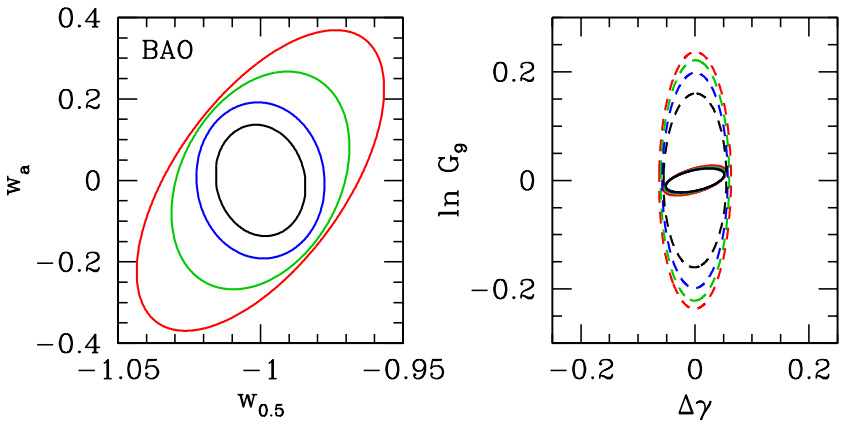

Figure 9 Same as Fig. 8, but varying BAO errors from fiducial×4 (red) to fiducial/2 (black).

the model introduces degeneracies between these dark energy parameters and other parameters, including h. Since constraints from SN data help to break these degeneracies, reducing SN errors can significantly improve measurement of the Hubble constant in the w_0–w_a model.

As one continues to add more dark energy parameters to the model, the degeneracies between these parameters and h increase, but another effect arises that diminishes the impact of SN data on σ_h. Measurement of the Hubble constant requires relating observed quantities at $z > 0$ (e.g. SN distances) to the expansion rate at $z = 0$. In the case of ΛCDM or the w_0–w_a model, the assumed dark energy evolution is simple enough that this relation between $z = 0$ and low-redshift observations is largely set by the model. However, when we specify $w(z)$ by a large number of independent bins in redshift, this relation must instead be determined by the data, which requires that the data have sufficient resolution in redshift near $z = 0$. For the default SN bins of width 0.2 in redshift, nearly 7 of the 36 w_i bins fall within the first bin at $0 < z < 0.2$. Consequently, changes in the lowest-redshift w_i value, which is strongly degenerate with h, have little effect on the SN data (Mortonson et al., 2009a). Dividing SNe into finer redshift bins makes it harder for variations in the lowest-redshift w_i to remain hidden in the SN data, thus restoring some of the sensitivity of SN data to the Hubble constant (see the right panel of Figure 12). Note that because BAO observations are tied to the distance scale of the CMB, they retain their sensitivity to h even in the absence of low-redshift constraints. For example, if we drop the 3 lowest-redshift BAO bins ($z < 0.231$) entirely from the fiducial forecast with binned $w(z)$ (see Table 3), then the change in σ_h as BAO errors change from half to four times the fiducial errors is $0.22 \rightarrow 0.44$, compared to $0.14 \rightarrow 0.42$ when the three lowest redshift bins are included. On the other hand, SN data only contribute to measurements of h in the most general dark energy parameterizations if they have a low redshift component that can be accurately compared with the sample of SNe at higher redshifts.

While fine binning in redshift is not *necessary* for BAO data to contribute to constraints on general dark energy models, it can help. Measurements of $H(z)$ and $D(z)$ in narrower bins are better able to constrain rapid variations in $w(z)$. They can also reduce uncertainty in the Hubble constant by a factor of 2–3, and in other parameters such as Ω_K, $\ln G_9$, and $\Delta\gamma$ by a smaller amount, relative to measurements in wide bins. However, in practice one cannot reduce the bin size indefinitely, since each bin must contain enough objects to be able to robustly identify and locate the BAO peak; for example, requiring that the bin be at least wide enough to contain pairs of objects separated by $\sim 100\,h^{-1}$ Mpc along the line of sight sets a lower limit of $\Delta z/(1+z) \gtrsim 0.03$.

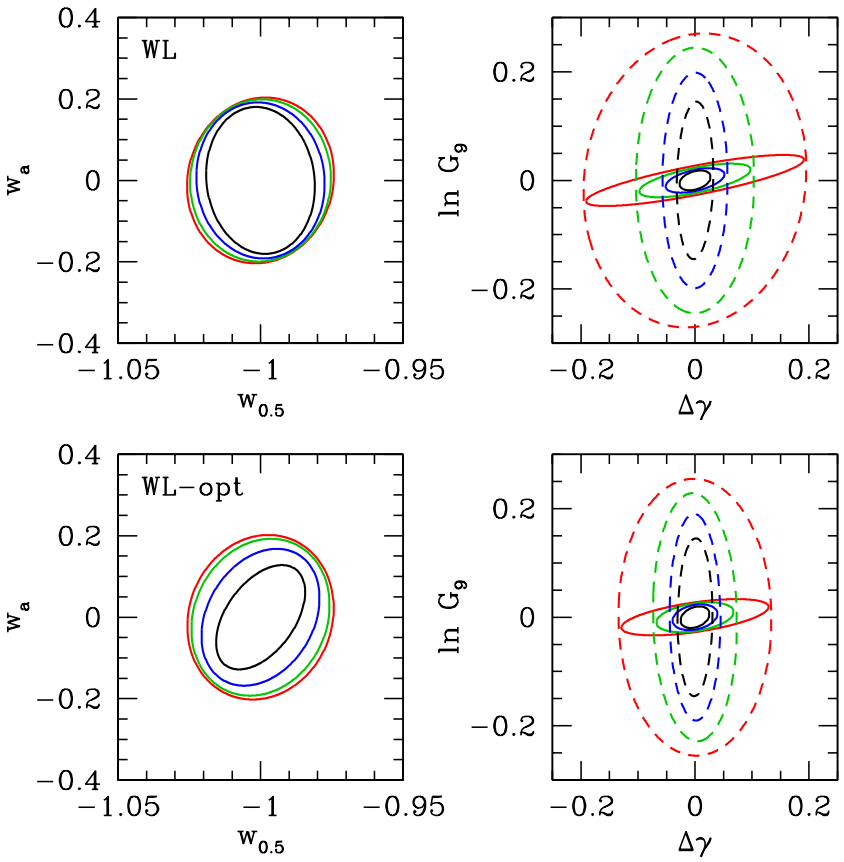

Figure 10 Same as Fig. 8, but varying WL errors from fiducial×4 (red) to fiducial/2 (black). Lower panels assume the optimistic WL forecasts.

We do not attempt to optimize the choice of bins for the simplified forecasts in this section, but we note that binning schemes in analyses of BAO data aimed at constraining general $w(z)$ variations should be chosen with care to avoid losing information about dark energy evolution and other parameters. Similar concerns are likely to apply for WL data as well.

3.3.4. Constraints on $w(z)$ in the general model

So far, in the context of general dark energy evolution we have only considered the forecast errors on parameters such as h and Ω_K that are partially degenerate with $w(z)$. But how accurately can $w(z)$ itself be measured when we do not restrict it to specific functional forms? Since the errors on w_i values in different bins are typically strongly correlated with each other, it is not very useful to simply give the expected w_i errors, marginalized over all other parameters. Instead, we can consider combinations of the w_i that are independent of one another and ask how well each of these combinations can be measured by the fiducial program of observations.

As mentioned in §2.2, many methods for combining $w(z)$ bins into independent (or nearly independent) components have been proposed. Here we adopt the principal component (PC) decomposition of the dark energy equation of state. Starting from the Fisher matrix for the combined acceleration probes, the PCs are computed by first marginalizing the Fisher matrix over everything except for the w_i parameters and then diagonalizing the remaining matrix, as described above in §3.2. The shapes of the three best-measured PCs for the fiducial program (with both fiducial and

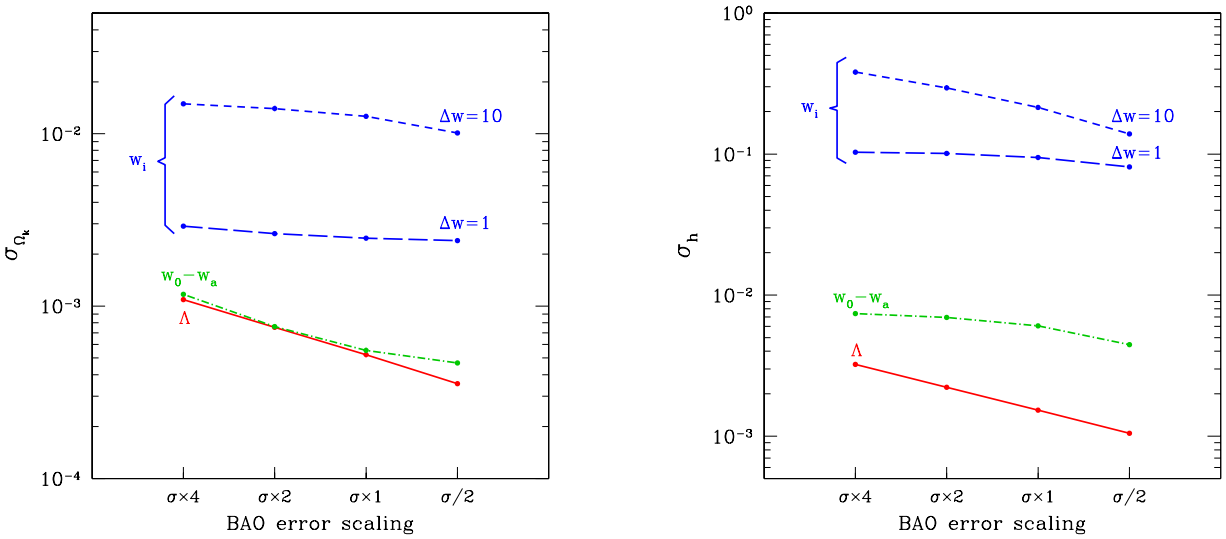

Figure 11 Dependence of σ_{Ω_k} (left) and σ_h (right) on BAO errors for various dark energy parametrizations and priors. For the w_i curves, the equation of state varies independently in 36 bins with Gaussian priors of width $\sigma_{w_i} = \Delta w/\sqrt{\Delta a}$. The fiducial versions of the Stage IV SN, WL, and CMB data are included in all cases.

optimistic WL assumptions) and some simple variations are plotted in Figure 13. In general, the structure of the PCs is similar in all cases; for example, the combination of w_i that is most tightly constrained is typically a single, broad peak at $z < 1$, while the next best-determined combination is the difference between $w(z \sim 0.2)$ and $w(z \sim 1)$. However, variations in the forecast assumptions slightly alter the shape of each PC and, in particular, shift the redshifts at which features in the PC shapes appear. Changes in the location of the peak in the first PC mirror the dependence of the pivot redshift z_p for the w_0–w_a model in Tables 5–7, with improved SN data decreasing the peak redshift and improved BAO data increasing it. The direction and magnitude of these shifts reflects the redshift range that a particular probe is most sensitive to and the degree to which that probe contributes to the total constraints on $w(z)$. Note that so far we have only considered the impact of forecast assumptions on the functional form of PCs, and not on the precision with which each PC can be measured. In general, altering the forecast model changes both the PC *shapes* and PC *errors*, which complicates the comparison among expected PC constraints from different sets of forecasts.

Comparing the top and bottom rows of panels in Figure 13, we see again the contrast between the fiducial WL forecast and the "WL-opt" forecast with reduced systematic errors. In the former case, decreasing WL errors by a factor of two has a negligible effect on the PC shapes relative to similar reductions in SN or BAO errors. However, when we take WL-opt as the baseline forecast the PCs depend more on the precision of WL measurements and less on that of the SN or BAO data.

The full set of PCs for the fiducial program is shown in Figure 14, and the forecast errors on the PC amplitudes are listed in Table 8. The best-measured, lowest-variance PCs vary smoothly with redshift, corresponding to averaging $w(z)$ over fairly broad ranges in z. There is a clear trend of increasingly high frequency oscillations for higher PCs. Visual inspection of Figure 14 shows that the sum of the number of peaks and the number of troughs in the PC is equal to the index of the

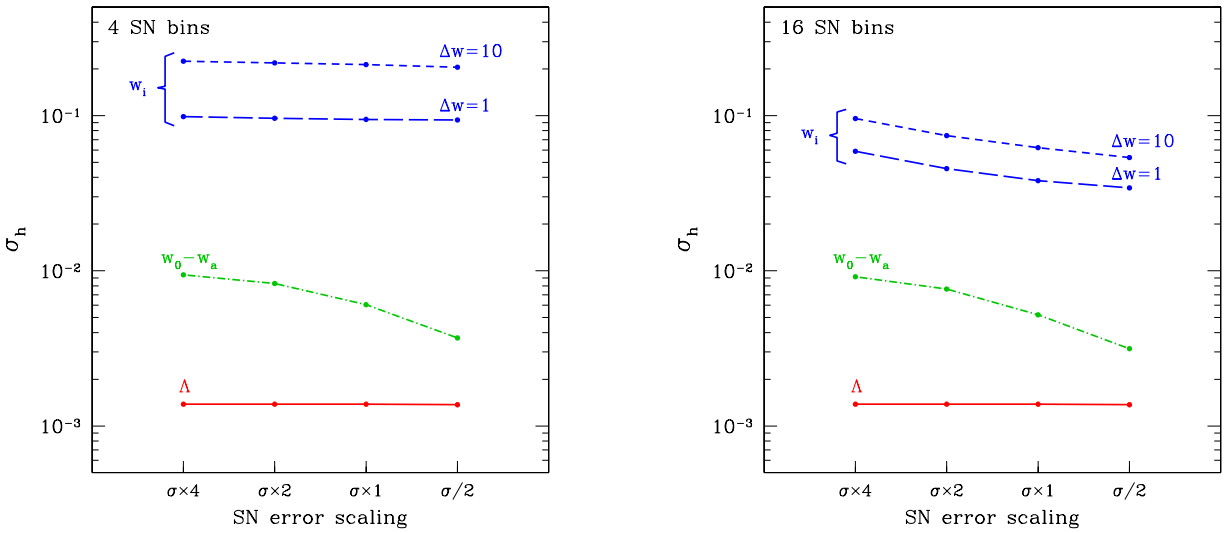

Figure 12 Dependence of σ_h on SN errors for various dark energy parametrizations and priors, including the fiducial BAO, WL, and CMB forecasts. Constraints in the left panel assume the "SNc4" forecast with 4 redshift bins at $z < 0.8$ including a correlated systematic error between bins with correlation length $\Delta z_c = 0.2$ (see eq. 49 and Table 4 for details). The right panel uses the "SNc16" forecast, which uses the same redshift correlation model but increases the number of bins at $z < 0.8$ to 16.

PC, a pattern that continues at least up to PC 12. Higher PCs often change sign between adjacent z bins. High frequency oscillations in $w(z)$ are poorly measured by any combination of cosmological data because the evolution of the dark energy *density*, which determines $H(z)$, depends on an integral of $w(z)$ (eq. 22), and $D(z)$ and $G(z)$ depend (approximately) on integrals of $H(z)$. Rapid oscillations in $w(z)$ tend to cancel out in these integrals. Many of the most poorly-measured PCs depend on the chosen BAO binning scheme, since narrower BAO bins can better sample rapid changes in $w(z)$. As an example, we show how the PCs of the fiducial program are affected by doubling the number of BAO bins in Figure 14.

The maximum redshift probed by SN, BAO, and WL data, primarily set by the highest-redshift BAO constraint at $z = 3$ in our forecasts, imprints a clear signature in the set of PCs in Figure 14. At high redshift, specifically $z > 3$ ($a < 0.25$), all but the six highest-variance PCs have almost no weight. Conversely, the last six PCs only vary significantly at high redshift and are nearly flat for $z < 3$; additionally, the errors on these PCs are many times larger than those of the first 30 PCs.[16] Thus, $w(z)$ variations above and below $z = 3$ are almost completely decoupled from each other in the fiducial forecasts, and the high-redshift variations are effectively unconstrained. CMB data limit the equation of state at $z > 3$ to some extent, for example, through comparison of the measured distance to the last scattering surface with the distance to $z = 3$ measured in BAO data. However, such constraints are very weak when split among several independent $w(z)$ bins at high redshift. Furthermore, since the dark energy density typically falls rapidly with increasing redshift, variations in $w(z)$ at high redshift are intrinsically less able to affect observable quantities than low-redshift variations, resulting in reduced sensitivity to the high-redshift equation of state

[16]Note that our w_i parameterization has exactly $(0.25 - 0.1)/0.025 = 6$ bins at $3 < z < 9$ and 30 bins at $z < 3$.

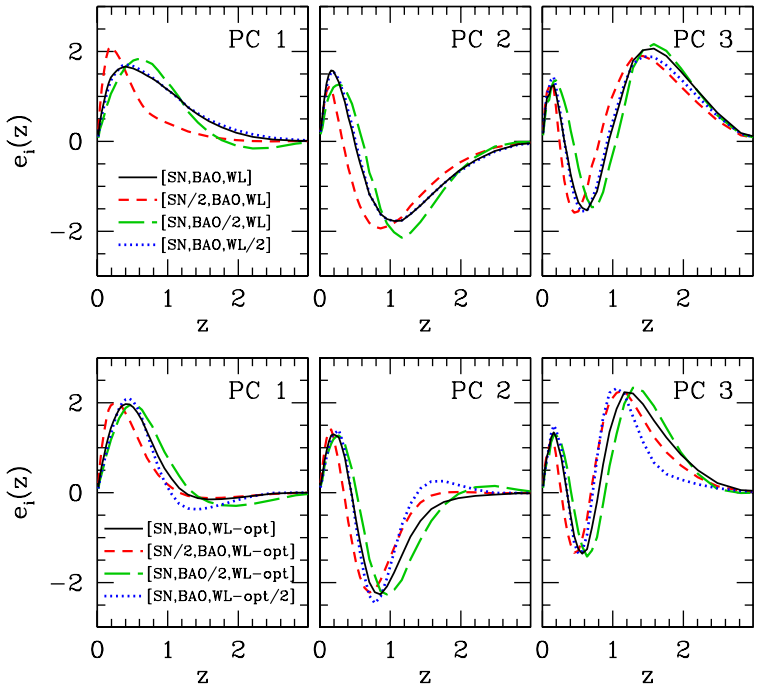

Figure 13 The three best-measured PCs for the fiducial program (solid curves) and from programs with SN, BAO, or WL errors halved (as labeled). The top row uses the fiducial version of the WL forecast, while the bottom row uses the optimistic WL forecast with reduced systematic errors. Although not indicated in the plot legends, all forecasts here include the default Planck CMB Fisher matrix. For all PCs shown here, $e_i(z)$ is nearly zero for $3 < z < 9$.

even in the presence of strong constraints at earlier epochs. Likewise, variations in $w(z)$ at even higher redshifts of $z > 9$, where we assume that w is fixed to -1, are unlikely to significantly affect constraints on $w(z)$ at low redshift.[17].

Figure 15 shows how the inverse variance σ_i^{-2} of the 10 best-measured $w(z)$ PCs increases relative to the fiducial program if we halve the errors on the SN, BAO, or WL data. Following Albrecht et al. (2009), when computing these ratios $\sigma_{(2)i}^{-2}/\sigma_{(1)i}^{-2}$ (where 1 denotes the fiducial program and 2 the improved program), we first limit PC variances to unity by making the substitution $\sigma_i^{-2} \to 1 + \sigma_i^{-2}$, so that uninteresting improvements in the most poorly-measured PCs do not count in favor of a particular forecast. We caution that, as noted earlier, the PC *shapes* themselves are changing as we change the errors assumed in the forecast, so $\sigma_{(2)i}^2$ and $\sigma_{(1)i}^2$ are not variances of identical $w(z)$ components. However, as shown in Figure 13, these changes are not drastic if we consider factor-of-two variations about our fiducial program.

The differences in σ_i^{-2} ratios among improvements in SN, BAO, and WL errors is striking. Relative to the fiducial program, reduced SN errors mainly contribute to knowledge of the first

[17]This partly depends on the choice of fiducial model at which the Fisher matrix used to construct the PCs is computed. Taking a fiducial model with a larger dark energy density at high redshift than in ΛCDM makes the low-redshift PC shapes more sensitive to assumptions about the high-redshift equation of state (e.g., de Putter and Linder (2008))

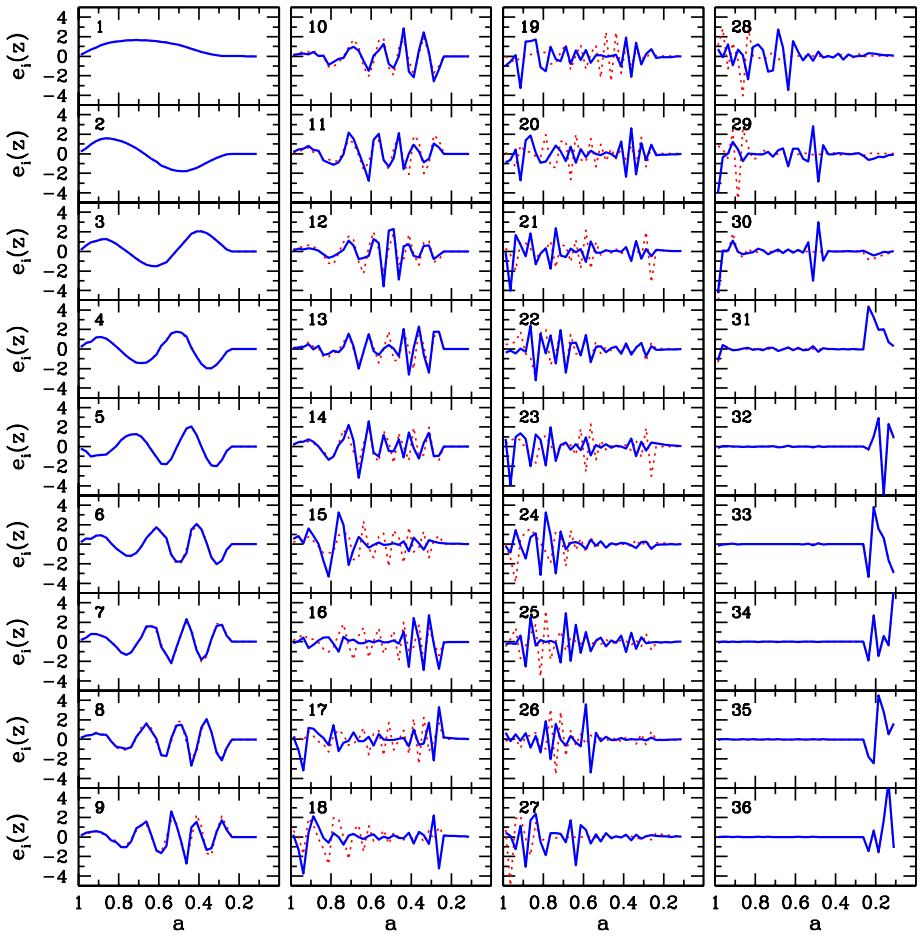

Figure 14 PCs for the fiducial program (solid blue curves). Dotted red curves double the number of bins used for BAO data from the default choice of 20 to 40.

Table 8 Errors on PC amplitudes for the fiducial program (shown in Fig. 14) and with the optimistic WL forecast.

i	$\sigma_i^{\rm fid}$	$\sigma_i^{\rm opt}$	i	$\sigma_i^{\rm fid}$	$\sigma_i^{\rm opt}$	i	$\sigma_i^{\rm fid}$	$\sigma_i^{\rm opt}$	i	$\sigma_i^{\rm fid}$	$\sigma_i^{\rm opt}$
1	0.011	0.009	10	0.138	0.109	19	0.398	0.311	28	1.263	0.760
2	0.019	0.015	11	0.147	0.134	20	0.417	0.353	29	1.685	0.871
3	0.029	0.021	12	0.170	0.142	21	0.551	0.403	30	2.406	2.073
4	0.042	0.029	13	0.182	0.157	22	0.570	0.429	31	6.117	5.827
5	0.056	0.039	14	0.189	0.178	23	0.571	0.472	32	12.17	18.88
6	0.070	0.051	15	0.238	0.218	24	0.630	0.580	33	16.02	24.98
7	0.087	0.065	16	0.249	0.239	25	0.736	0.585	34	24.86	45.88
8	0.101	0.078	17	0.292	0.262	26	0.925	0.594	35	61.03	96.81
9	0.118	0.096	18	0.318	0.283	27	1.035	0.646	36	71.88	114.5

few PCs. For the fiducial WL systematics, reducing WL errors helps to better measure several of the highest-variance PCs, but it makes little difference to the well measured PCs. Reducing BAO errors tightens constraints on nearly all of the PCs, with the greatest impact in the intermediate range between the SN and WL contributions. Assuming the optimistic WL errors gives much greater weight to WL improvements, which now produce the largest improvement in the first five PCs (right panel of Figure 15). The trends for reducing SN or BAO errors are similar to before, but the magnitude of their effect is smaller because they are competing with tighter WL constraints. The trends for the σ_i^{-2} ratios of the best-measured PCs mirror those shown for the DETF FoM in Figure 5. With the fiducial WL systematics, BAO measurements have the greatest leverage, followed by SN, and the impact of reducing WL errors is small. With the optimistic WL systematics, on the other hand, reducing WL errors makes the largest difference, followed by BAO, followed by SN.

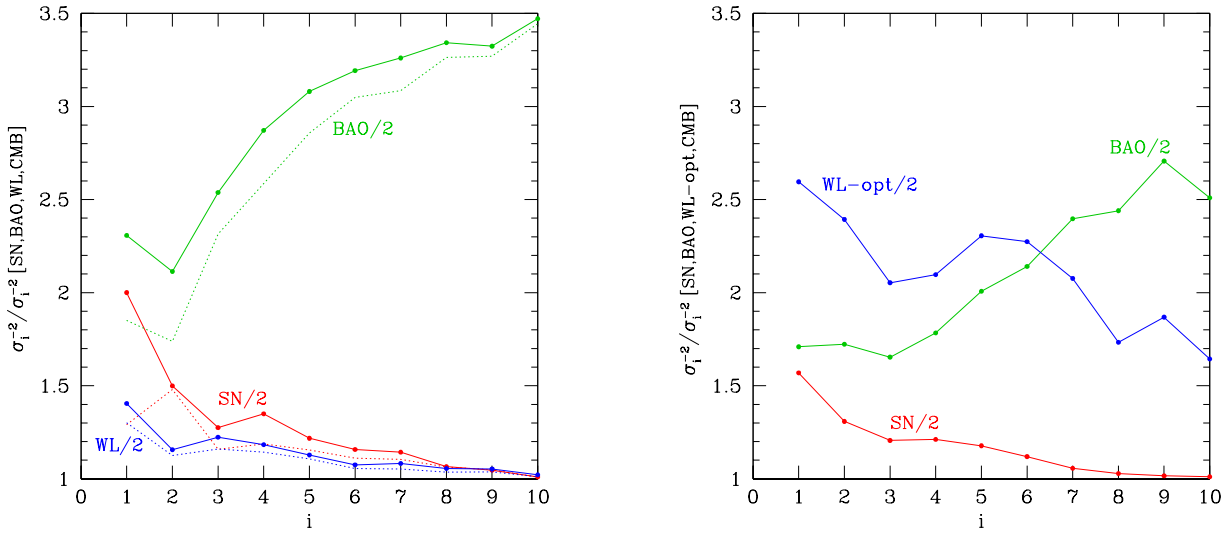

Figure 15 Ratios of inverse variances of PC amplitudes for variants of the fiducial program to the fiducial inverse variances (points and solid curves). Each variant divides SN, BAO, or WL errors by a factor of 2 while keeping other probes fixed at the fiducial errors. The left panel assumes the default WL forecast and the right panel assumes the optimistic version. Dotted curves in the left panel use $\hat{\sigma}_i$ instead of σ_i, which describes how well the amplitudes of the *fiducial* set of PCs are expected to be measured by some variant of the fiducial forecast.

Dotted curves in the left hand panel show the σ_i^{-2} ratios when we *fix* the PCs to be those of the fiducial program. In this case, the PC errors for the improved programs are no longer uncorrelated, but the correlation coefficient of errors among any pair of PCs is less than 0.5 in nearly all cases. Results are similar to before except for the first component (first two components for BAO). These, of course, show less improvement when they are fixed to be those of the fiducial program rather than shifting to be the components best determined by the improved data.

Other figures of merit for PC constraints have been defined in the literature, each of which may be useful for different purposes. These include the determinant of $\mathbf{F}^w$, which characterizes the total volume of parameter space allowed by a particular combination of experiments, in analogy to the DETF FoM for the w_0–w_a parameter space, and the sum of the inverse variances of the PCs, which is typically less sensitive to changes in the errors of the most weakly constrained PCs (Huterer

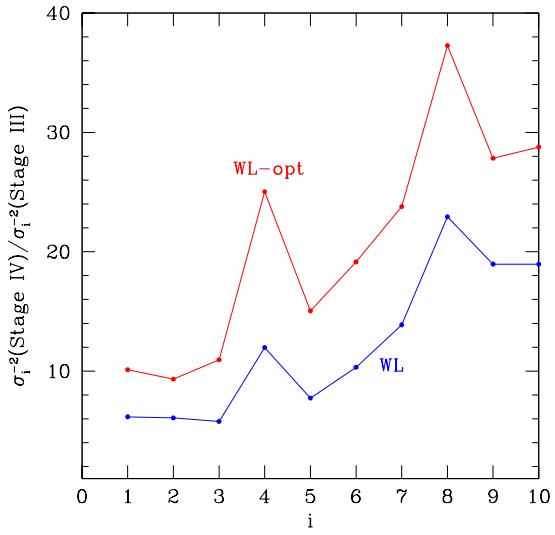

Figure 16 Ratios of inverse variances of PC amplitudes of Stage IV to those of Stage III, assuming either the fiducial or optimistic versions of the Stage IV WL forecast.

and Turner, 2001; Albrecht et al., 2006; Albrecht and Bernstein, 2007; Wang, 2008; Barnard et al., 2008; Albrecht et al., 2009; Crittenden et al., 2009; Amara and Kitching, 2010; Mortonson et al., 2010; Shapiro et al., 2010; Trotta et al., 2010; March et al., 2011).

Examples of these FoMs for the fiducial program and the variants considered in Figure 15 are listed in Table 9. Here we allow the PC basis to change with the forecast assumptions, so $\mathbf{F}^w$ is diagonal and $\det \mathbf{F}^w = \prod_{i=1}^{36} \sigma_i^{-2}$. As with the ratios of PC variances in Figure 15, we restrict the variances to be less than unity by replacing $\sigma_i^{-2} \to 1 + \sigma_i^{-2}$. The other FoM, computed as the sum of inverse variances, requires no such prior because PCs with large variances contribute negligibly to the sum. Note that the choice of PC FoM definition can affect decisions about whether one experiment or another is optimal; for example, halving WL errors (assuming fiducial systematics) relative to the fiducial model increases the $\det \mathbf{F}^w$ FoM more than halving SN errors, but the opposite is true for the sum of inverse variances, which favors improvements in the best-measured PCs and more closely tracks the DETF FoM. In this case, at least, we regard the latter measure as a better diagnostic, since the improvements for PCs that are poorly measured in any case seem unlikely to reveal departures from a cosmological constant or other simple dark energy models.

Table 9 Examples of PC FoMs for selected forecasts, with the DETF FoM for comparison.

Forecast case	$\log \prod_{i=1}^{36} \left(1 + \sigma_i^{-2}\right)^{1/2}$	$(\sum_{i=1}^{36} \sigma_i^{-2})^{1/2}$	$[\sigma(w_p)\sigma(w_a)]^{-1}$
[SN,BAO,WL,CMB]	21.1	116	533
[SN/2,BAO,WL,CMB]	21.6	153	903
[SN,BAO/2,WL,CMB]	27.9	181	1070
[SN,BAO,WL/2,CMB]	22.2	133	671
[SN,BAO,WL-opt,CMB]	23.7	150	687
[SN/2,BAO,WL-opt,CMB]	24.1	180	981
[SN,BAO/2,WL-opt,CMB]	29.5	201	1129
[SN,BAO,WL-opt/2,CMB]	26.5	235	1309

The disagreement between different PC FoMs in Table 9 highlights one of the difficulties with using PCs or related methods for evaluating the potential impact of future experiments. Forecasts for PCs provide a wealth of information in both the redshift-dependent shapes of the PCs and the expected errors on their amplitudes, but it is often difficult to interpret what this information implies about cosmic acceleration. Given a set of forecasts for PCs, one can easily compute the expected constraints on any specific model for $w(z)$ by expressing the model in terms of the PC amplitudes (eq. 57); this is a potentially useful application, but it makes very limited use of the available information.

More generally, we can use the forecast PC shapes and errors to try to visualize what types of $w(z)$ variations are allowed by a certain combination of experiments. One approach is to generate several random $w(z)$ curves that would be consistent with the forecast measurements. This method is easily implemented with the PCs because the errors on different PC amplitudes are uncorrelated. One can generate a random realization of $w(z)$ by simply drawing an amplitude α_i from a Gaussian distribution with mean zero and width σ_i, then using equation (58) to compute $w(z)$ corresponding to the randomly-drawn α_i values.

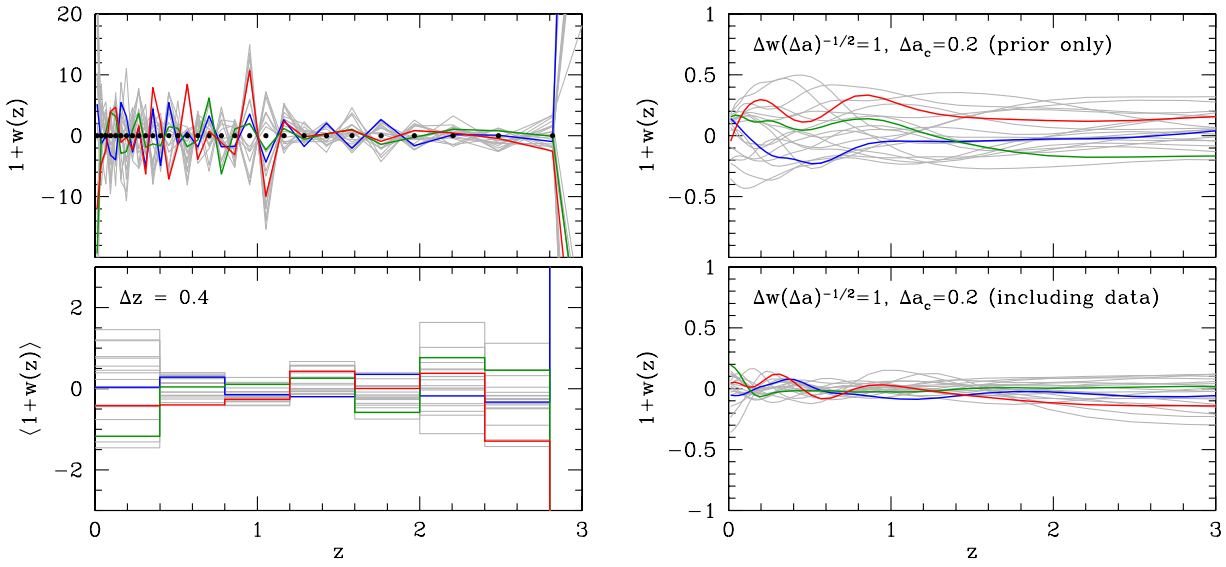

Figure 17 Reconstruction of $w(z)$ from PC constraints. *Left:* 20 randomly-generated models that would be indistinguishable from a cosmological constant using the fiducial program of experiments. Three of the 20 models are highlighted (in red, green, and blue) to more clearly show examples of the evolution with redshift. The lower panel shows the average of $1 + w(z)$ in bins of width $\Delta z = 0.4$ for the same models as in the upper panel. Points along the $w(z) = -1$ line in the upper panel mark the centers of the bins in which $w(z)$ is allowed to vary in our forecasts. *Right:* $w(z)$ reconstruction including a prior of the form in equation (61). The upper panel shows a random selection of models consistent with this prior, but without including any data, and the lower panel shows examples of models that are allowed by both the prior and the data assumed in the fiducial program.

In the upper left panel of Figure 17, we use this method to plot several $w(z)$ models using the fiducial program PC shapes and errors from Figure 14 and Table 8, respectively. We cut off the plot at $z = 3$, since $w(z)$ variations at higher redshifts are essentially unconstrained by the fiducial

experiments. Even at lower redshifts, though, the allowed $w(z)$ variations are enormous, with w_i values often changing by 10 or more from one bin to the next. (Recall that our prior corresponds to a Gaussian of width $\sigma_{w_i} \approx 63$ per bin, eq. 55.) Compared to the $\sim 1.5\%$ constraints on w_p in the w_0–w_a model, this forecast looks rather depressing. The consequence of allowing the equation of state to be a free function of redshift is that it is nearly impossible to say with any certainty what the value of w is at a specific redshift, because rapid oscillations in $w(z)$ have tiny effects on observables. The allowed range of variations would be even larger if we considered a model with finer Δa bins.

The large variations of $w(z)$ in Figure 17 are driven by the poorly constrained PCs, which have many oscillations in $w(z)$, peak-to-peak amplitudes $|\Delta w| \sim 4$, and normalization uncertainties $\sigma_i \sim 0.1 - 2.4$ (see Figure 14 and Table 8). The lower left panel of Figure 17 shows these $w(z)$ realizations averaged over bins of width $\Delta z = 0.4$, which vastly reduces the range of variations, especially at $z \sim 1$. However, the dispersion of $w(z)$ in the bins centered at $z = 0.6$ and $z = 1$ is still about 0.25.

Instead of averaging $w(z)$ over wide redshift bins, one can impose a theoretical prejudice for models with smoothly-varying equations of state by adding an off-diagonal prior to the Fisher matrix, imposing correlations among the w_i that are closely separated in redshift. Here we follow Crittenden et al. (2009), but we modify their method to use scale factor rather than redshift as the independent variable, adopting a correlation function

$$\xi(|a_i - a_j|) = \frac{(\Delta w)^2}{\pi \Delta a_c} \left[1 + \left(\frac{a_i - a_j}{\Delta a_c} \right)^2 \right]^{-1}, \tag{60}$$

where Δw sets the amplitude of allowed $w(z)$ variations and Δa_c is the correlation length. Following the calculation in Crittenden et al. (2009), the covariance matrix for the w_i bins, which is the inverse of the prior Fisher matrix for those parameters, is

$$[F_{ij}^{\rm prior}]^{-1}_{(i,j\le 36)} = \frac{(\Delta w)^2 \Delta a_c}{\pi \Delta a^2} \left[x_+ \tan^{-1} x_+ + x_- \tan^{-1} x_- - 2\bar{x} \tan^{-1} \bar{x} + \ln \left(\frac{1+\bar{x}^2}{\sqrt{(1+x_+^2)(1+x_-^2)}} \right) \right], \tag{61}$$

where $\bar{x} = |i-j|\Delta a/\Delta a_c$, $x_+ = (|i-j|+1)\Delta a/\Delta a_c$, and $x_- = (|i-j|-1)\Delta a/\Delta a_c$. In the limit $\Delta a_c \to 0$, this reduces to our default diagonal prior on the w_i parameters with width $\sigma_{w_i} = \Delta w/\sqrt{\Delta a}$.

The upper right panel of Figure 17 shows models randomly drawn from this prior with $\Delta w/\sqrt{\Delta a} = 1$ and $\Delta a_c = 0.2$. The influence of the correlation function is clearly evident in the smoother, lower-amplitude variations of $w(z)$ in these models, and yet the range of possible models is still much greater than for simpler parameterizations like w_0–w_a. Combining this prior with the assumed data set of the fiducial Stage IV program, we obtain the $w(z)$ realizations plotted in the lower right panel of Figure 17. Even more so than averaging $w(z)$ in wide redshift bins, including this type of prior significantly narrows the constraints on $w(z)$.

Our constraints on general $w(z)$ models account for the possibility of modified gravity by marginalizing over the structure growth parameters $\Delta\gamma$ and $\ln G_9$. If we instead restrict our analysis to GR by fixing $\Delta\gamma = \ln G_9 = 0$, the main effect is that the dark energy equation of state at high redshifts, $w(3 < z < 9)$, is better constrained since the CMB measurement of the power spectrum amplitude at $z \sim 1000$ can be more directly related to WL measurements of growth at lower redshifts. Because of the additional CMB constraint on the distance to the last scattering surface, $w(3 < z < 9)$ is strongly correlated with Ω_k, and therefore assuming GR considerably improves the

determination of spatial curvature in the binned $w(z)$ parameterization. For our fiducial forecasts, assuming $\Delta\gamma = \ln G_9 = 0$ lowers σ_{Ω_k} by a factor of ~ 5 ($0.0125 \to 0.0025$); note that this is still several times larger than the error in Ω_k for the simpler ΛCDM or w_0–w_a forecasts.

4. Conclusions

Appendix A. Acronym Glossary

ACT = Atacama Cosmology Telescope
ADEPT = Advanced Dark Energy Physics Telescope
BAO = Baryon Acoustic Oscillations
BOSS = Baryon Oscillation Spectroscopic Survey
CMB = Cosmic Microwave Background
DES = Dark Energy Survey
DESTINY = Dark Energy Space Telescope
DUNE = Dark Universe Explorer
ESA = European Space Agency
GR = General Relativity
HETDEX = Hobby-Eberly Telescope Dark Energy Experiment
JDEM = Joint Dark Energy Mission
JEDI = Joint Efficient Dark-energy Investigation
LASST = Large Area Synoptic Survey Telescope
LSST = Large Synoptic Survey Telescope
NASA = National Aeronautics and Space Administration
NOAO = National Optical Astronomy Observatories
Pan-STARRS = Panoramic Survey Telescope and Rapid Response System
SDSS = Sloan Digital Sky Survey
SKA = Square Kilometer Array
SNAP = Supernova Acceleration Probe
SPT = South Pole Telescope

References

, 2006. Planck: The scientific programme.

Abazajian, K. N., et al., 2009. The Seventh Data Release of the Sloan Digital Sky Survey. Astrophys. J. Suppl. 182, 543–558.

Albrecht, A., Bernstein, G., 2007. Evaluating dark energy probes using multidimensional dark energy parameters. Phys. Rev. D75, 103003.

Albrecht, A., et al., 2006. Report of the Dark Energy Task Force.

Albrecht, A., et al., 2009. Findings of the Joint Dark Energy Mission Figure of Merit Science Working Group.

Amara, A., Kitching, T., 2010. Figures of Merit for Testing Standard Models: Application to Dark Energy Experiments in Cosmology.

Amendola, L., Quercellini, C., Giallongo, E., 2005. Constraints on perfect fluid and scalar field dark energy models from future redshift surveys. Mon. Not. Roy. Astron. Soc. 357, 429–439.

Bardeen, J. M., Bond, J. R., Kaiser, N., Szalay, A. S., 1986. The Statistics of Peaks of Gaussian Random Fields. Astrophys. J. 304, 15–61.

Barnard, M., Abrahamse, A., Albrecht, A., Bozek, B., Yashar, M., 2008. A measure of the impact of future dark energy experiments based on discriminating power among quintessence models. Phys. Rev. D78, 043528.

Bennett, C. L., et al., 2003. First Year Wilkinson Microwave Anisotropy Probe (WMAP) Observations: Preliminary Maps and Basic Results. Astrophys. J. Suppl. 148, 1.

Berlind, A. A., Weinberg, D. H., 2002. The Halo Occupation Distribution: Towards an Empirical Determination of the Relation Between Galaxies and Mass. Astrophys. J. 575, 587–616.

Blanchard, A., 2010. Evidence for the Fifth Element Astrophysical status of Dark Energy. Astron. Astrophys. Rev. 18, 595–645.

Bond, J. R., Cole, S., Efstathiou, G., Kaiser, N., 1991. Excursion set mass functions for hierarchical Gaussian fluctuations. Astrophys. J. 379, 440.

Bucher, M., Goldhaber, A. S., Turok, N., 1995. An open universe from inflation. Phys. Rev. D52, 3314–3337.

Caldwell, R. R., Linder, E. V., 2005. The limits of quintessence. Phys. Rev. Lett. 95, 141301.

Carlson, J., White, M., Padmanabhan, N., 2009. A critical look at cosmological perturbation theory techniques. Phys. Rev. D80, 043531.

Carroll, S. M., 2003. Why is the universe accelerating? ECONF C0307282, TTH09.

Chaboyer, B., 1998. The Age of the Universe. Phys. Rept. 307, 23–30.

Cole, S., Fisher, K. B., Weinberg, D. H., 1994. Fourier analysis of redshift space distortions and the determination of Omega. Mon. Not. Roy. Astron. Soc. 267, 785.

Cole, S., Kaiser, N., Apr. 1989. Biased clustering in the cold dark matter cosmogony. MNRAS237, 1127–1146.

Cole, S., Weinberg, D. H., Frenk, C. S., Ratra, B., 1997. Large-scale structure in COBE-normalized cold dark matter cosmogonies. Mon. Not. Roy. Astron. Soc. 289, 37.

Cole, S., et al., 2005. The 2dF Galaxy Redshift Survey: Power-spectrum analysis of the final dataset and cosmological implications. Mon. Not. Roy. Astron. Soc. 362, 505–534.

Conroy, C., Wechsler, R. H., Kravtsov, A. V., 2006. Modeling Luminosity-Dependent Galaxy Clustering Through Cosmic Time. Astrophys. J. 647, 201–214.

Crittenden, R. G., Pogosian, L., Zhao, G.-B., 2009. Investigating dark energy experiments with principal components. JCAP 0912, 025.

de Bernardis, P., et al., 2000. A Flat Universe from High-Resolution Maps of the Cosmic Microwave Background Radiation. Nature 404, 955–959.

de Putter, R., Linder, E. V., 2008. To Bin or Not To Bin: Decorrelating the Cosmic Equation of State. Astropart. Phys. 29, 424–441.

Dick, J., Knox, L., Chu, M., 2006. Reduction of Cosmological Data for the Detection of Time-varying Dark Energy Density. JCAP 0607, 001.

Dicke, R. H., Peebles, P. J. E., Roll, P. G., Wilkinson, D. T., 1965. Cosmic Black-Body Radiation. Astrophys. J. 142, 414–419.

Dodelson, S., 2003. Modern cosmology.

Dvali, G. R., Gabadadze, G., Porrati, M., 2000. 4D gravity on a brane in 5D Minkowski space. Phys. Lett. B485, 208–214.

Efstathiou, G., Jun. 1995. An anthropic argument for a cosmological constant. MNRAS274, L73–L76.

Efstathiou, G., Sutherland, W. J., Maddox, S. J., 1990. The cosmological constant and cold dark matter. Nature 348, 705–707.

Einstein, A., 1917. Cosmological Considerations in the General Theory of Relativity. Sitzungsber. Preuss. Akad. Wiss. Berlin (Math. Phys.) 1917, 142–152.

Eisenstein, D. J., et al., 2005. Detection of the Baryon Acoustic Peak in the Large-Scale Correlation Function of SDSS Luminous Red Galaxies. Astrophys. J. 633, 560–574.

Freedman, W. L., et al., 2009. The Carnegie Supernova Project: First Near-Infrared Hubble Diagram to z 0.7. Astrophys. J. 704, 1036–1058.

Freese, K., 2005. Cardassian expansion: Dark energy density from modified Friedmann equations. New Astron. Rev. 49, 103–109.

Freese, K., Lewis, M., 2002. Cardassian Expansion: a Model in which the Universe is Flat, Matter Dominated, and Accelerating. Phys. Lett. B540, 1–8.

Frieman, J., Turner, M., Huterer, D., 2008a. Dark Energy and the Accelerating Universe. Ann. Rev. Astron. Astrophys. 46, 385–432.

Frieman, J. A., 1996. Weak Lensing and the Measurement of q0 from Type Ia Supernovae.

Frieman, J. A., et al., 2008b. The Sloan Digital Sky Survey-II Supernova Survey: Technical Summary. Astron. J. 135, 338–347.

Gehrels, N., 2010. The Joint Dark Energy Mission (JDEM) Omega.

Griest, K., 2002. Toward a possible solution to the cosmic coincidence problem. Phys. Rev. D66, 123501.

Gunn, J. E., Gott, III, J. R., 1972. On the infall of matter into cluster of galaxies and some effects on their evolution. Astrophys. J. 176, 1–19.

Guth, A. H., 1981. The Inflationary Universe: A Possible Solution to the Horizon and Flatness Problems. Phys. Rev. D23, 347–356.

Hamilton, A. J. S., 1997. Linear Redshift Distortions: A Review.

Hamuy, M., et al., 2006. The Carnegie Supernova Project: The Low-Redshift Survey. Publ. Astron. Soc. Pac. 118, 2–20.

Hanany, S., et al., 2000. MAXIMA-1: A Measurement of the Cosmic Microwave Background Anisotropy on angular scales of 10 arcminutes to 5 degrees. Astrophys. J. 545, L5.

Heitmann, K., White, M., Wagner, C., Habib, S., Higdon, D., 2010. The Coyote Universe I: Precision Determination of the Nonlinear Matter Power Spectrum. Astrophys. J. 715, 104–121.

Hogg, D. W., 1999. Distance measures in cosmology.

Hu, W., 2002. Dark Energy and Matter Evolution from Lensing Tomography. Phys. Rev. D66, 083515.

Hu, W., 2005. Dark Energy Probes in Light of the CMB. ASP Conf. Ser. 339, 215.

Hu, W., Jain, B., 2004. Joint Galaxy-Lensing Observables and the Dark Energy. Phys. Rev. D70, 043009.

Hubble, E., 1929. A relation between distance and radial velocity among extra–galactic nebulae. Proc. Nat. Acad. Sci. 15, 168–173.

Huterer, D., Cooray, A., 2005. Uncorrelated Estimates of Dark Energy Evolution. Phys. Rev. D71, 023506.

Huterer, D., Starkman, G., 2003. Parameterization of dark-energy properties: A principal- component approach. Phys. Rev. Lett. 90, 031301.

Huterer, D., Turner, M. S., 2001. Probing the dark energy: Methods and strategies. Phys. Rev. D64, 123527.

Jain, B., Khoury, J., 2010. Cosmological Tests of Gravity. Annals Phys. 325, 1479–1516.

Jimenez, R., Loeb, A., 2002. Constraining Cosmological Parameters Based on Relative Galaxy Ages. Astrophys. J. 573, 37–42.

Kaiser, N., 1984. On the Spatial correlations of Abell clusters. Astrophys. J. 284, L9–L12.

Kaiser, N., 1987. Clustering in real space and in redshift space. Mon. Not. Roy. Astron. Soc. 227, 1–27.

Kessler, R., et al., 2009. First-year Sloan Digital Sky Survey-II (SDSS-II) Supernova Results: Hubble Diagram and Cosmological Parameters. Astrophys. J. Suppl. 185, 32–84.

Kitching, T. D., Amara, A., 2009. Fisher Matrix Decomposition for Dark Energy Prediction.

Komatsu, E., et al., 2009. Five-Year Wilkinson Microwave Anisotropy Probe (WMAP) Observations:Cosmological Interpretation. Astrophys. J. Suppl. 180, 330–376.

Komatsu, E., et al., 2011. Seven-Year Wilkinson Microwave Anisotropy Probe (WMAP) Observations: Cosmological Interpretation. Astrophys. J. Suppl. 192, 18.

Krauss, L. M., Turner, M. S., 1995. The cosmological constant is back. Gen. Rel. Grav. 27, 1137–1144.

Kravtsov, A. V., et al., 2004. The Dark Side of the Halo Occupation Distribution. Astrophys. J. 609, 35–49.

Larson, D., et al., 2011. Seven-Year Wilkinson Microwave Anisotropy Probe (WMAP) Observations: Power Spectra and WMAP-Derived Parameters. Astrophys. J. Suppl. 192, 16.

Lewis, A., Challinor, A., Lasenby, A., 2000. Efficient Computation of CMB anisotropies in closed FRW models. Astrophys. J. 538, 473–476.

Lightman, A. P., Schechter, P. L., Dec. 1990. The Omega dependence of peculiar velocities induced by spherical density perturbations. ApJS74, 831–+.

Linde, A. D., 1987. Eternally existing self-reproducing inflationary universe. Physica Scripta Volume T 15, 169–175.

Linder, E. V., 2003a. Exploring the expansion history of the universe. Phys. Rev. Lett. 90, 091301.

Linder, E. V., 2003b. Mapping the Dark Energy Equation of State.

Linder, E. V., 2005. Cosmic growth history and expansion history. Phys. Rev. D72, 043529.

Linder, E. V., 2007. Theory Challenges of the Accelerating Universe. J. Phys. A40, 6697.

Linder, E. V., 2010. Frontiers of Dark Energy.

Maddox, S. J., Efstathiou, G., Sutherland, W. J., Loveday, J., 1990. Galaxy correlations on large scales. Mon. Not. Roy. Astron. Soc. 242, 43–49.

Mantz, A., Allen, S. W., Rapetti, D., Ebeling, H., 2010. The Observed Growth of Massive Galaxy Clusters I: Statistical Methods and Cosmological Constraints. Mon. Not. Roy. Astron. Soc. 406, 1759–1772.

March, M. C., Trotta, R., Amendola, L., Huterer, D., 2011. Robustness to systematics for future dark energy probes.

Martel, H., Shapiro, P. R., Weinberg, S., 1998. Likely Values of the Cosmological Constant. Astrophys. J. 492, 29.

Maturi, M., Mignone, C., 2009. An optimal basis system for cosmology: data analysis and new parameterisation. Astron. Astrophys. 508, 45M.

Mo, H. J., White, S. D. M., 1996. An Analytic model for the spatial clustering of dark matter halos. Mon. Not. Roy. Astron. Soc. 282, 347.

Mortonson, M., Hu, W., Huterer, D., 2009a. Hiding dark energy transitions at low redshift. Phys. Rev. D80, 067301.

Mortonson, M. J., Hu, W., Huterer, D., 2009b. Falsifying Paradigms for Cosmic Acceleration. Phys. Rev. D79, 023004.

Mortonson, M. J., Huterer, D., Hu, W., 2010. Figures of merit for present and future dark energy probes. Phys. Rev. D82, 063004.

Mould, J. R., et al., 2000. The HST Key Project on the Extragalactic Distance Scale. XXVIII. Combining the Constraints on the Hubble Constant. Astrophys. J. 529, 786–794.

Netterfield, C. B., Devlin, M. J., Jarosik, N., Page, L., Wollack, E. J., 1997. A Measurement of the Angular Power Spectrum of the Anisotropy in the Cosmic Microwave Background. Astrophys. J. 474, 47.

Norberg, P., et al., 2001. The 2dF Galaxy Redshift Survey: Luminosity dependence of galaxy clustering s. Mon. Not. Roy. Astron. Soc. 328, 64.

Ostriker, J. P., Steinhardt, P. J., 1995. The Observational case for a low density universe with a nonzero cosmological constant. Nature 377, 600–602.

Peebles, P. J. E., 1980. The large-scale structure of the universe.

Peebles, P. J. E., Ratra, B., 2003. The cosmological constant and dark energy. Rev. Mod. Phys. 75, 559–606.

Penzias, A. A., Wilson, R. W., 1965. A Measurement of excess antenna temperature at 4080- Mc/s. Astrophys. J. 142, 419–421.

Perlmutter, S., et al., 1997. Measurements of the Cosmological Parameters Omega and Lambda from the First 7 Supernovae at z ¿= 0.35. Astrophys. J. 483, 565.

Perlmutter, S., et al., 1999. Measurements of Omega and Lambda from 42 High-Redshift Supernovae. Astrophys. J. 517, 565–586.

Phillips, M. M., 1993. The absolute magnitudes of Type IA supernovae. Astrophys. J. 413, L105–L108.

Press, W. H., Schechter, P., 1974. Formation of galaxies and clusters of galaxies by selfsimilar gravitational condensation. Astrophys. J. 187, 425–438.

Ratra, B., Peebles, P. J. E., 1988. Cosmological Consequences of a Rolling Homogeneous Scalar Field. Phys. Rev. D37, 3406.

Reid, B. A., et al., 2010a. Baryon Acoustic Oscillations in the Sloan Digital Sky Survey Data Release 7 Galaxy Sample. Mon. Not. Roy. Astron. Soc. 401, 2148–2168.

Reid, B. A., et al., 2010b. Cosmological Constraints from the Clustering of the Sloan Digital Sky Survey DR7 Luminous Red Galaxies. Mon. Not. Roy. Astron. Soc. 404, 60–85.

Riess, A. G., Livio, M., 2006. The First Type Ia Supernovae: An Empirical Approach to Taming Evolutionary Effects In Dark Energy Surveys from SNe Ia at z¿2. Astrophys. J. 648, 884–889.

Riess, A. G., Press, W. H., Kirshner, R. P., 1996. A Precise distance indicator: Type Ia supernova multicolor light curve shapes. Astrophys. J. 473, 88.

Riess, A. G., et al., 1998. Observational Evidence from Supernovae for an Accelerating Universe and a Cosmological Constant. Astron. J. 116, 1009–1038.

Riess, A. G., et al., 2007. New Hubble Space Telescope Discoveries of Type Ia Supernovae at $z > 1$: Narrowing Constraints on the Early Behavior of Dark Energy. Astrophys. J. 659, 98–121.

Riess, A. G., et al., 2009. A Redetermination of the Hubble Constant with the Hubble Space Telescope from a Differential Distance Ladder. Astrophys. J. 699, 539–563.

Rozo, E., et al., 2010. Cosmological Constraints from the SDSS maxBCG Cluster Catalog. Astrophys. J. 708, 645–660.

Schechter, P., 1976. An analytic expression for the luminosity function for galaxies. Astrophys. J. 203, 297–306.

Schmidt, B. P., et al., 1998. The High-Z Supernova Search: Measuring Cosmic Deceleration and Global Cur vature of the Universe Using Type Ia Supernovae. Astrophys. J. 507, 46–63.

Scoccimarro, R., 2004. Redshift-Space Distortions, Pairwise Velocities and Nonlinearities. Phys. Rev. D70, 083007.

Scoccimarro, R., Sheth, R. K., Hui, L., Jain, B., 2001. How Many Galaxies Fit in a Halo? Constraints on Galaxy Formation Efficiency from Spatial Clustering. Astrophys. J. 546, 20–34.

Seljak, U., 2000. Analytic model for galaxy and dark matter clustering. Mon. Not. Roy. Astron. Soc. 318, 203.

Seo, H.-J., Eisenstein, D. J., 2007. Improved forecasts for the baryon acoustic oscillations and cosmological distance scale. Astrophys. J. 665, 14–24.

Shapiro, C., Dodelson, S., Hoyle, B., Samushia, L., Flaugher, B., 2010. Will Multiple Probes of Dark Energy find Modified Gravity? Phys. Rev. D82, 043520.

Sheth, R. K., Tormen, G., 1999. Large scale bias and the peak background split. Mon. Not. Roy. Astron. Soc. 308, 119.

Simpson, F., Bridle, S., 2006. The redshift sensitivities of dark energy surveys. Phys. Rev. D73, 083001.

Skordis, C., Albrecht, A., 2002. Planck-scale quintessence and the physics of structure formation. Phys. Rev. D66, 043523.

Song, Y.-S., Hu, W., Sawicki, I., 2007. The large scale structure of f(R) gravity. Phys. Rev. D75, 044004.

Steinhardt, P. J., Wang, L.-M., Zlatev, I., 1999. Cosmological tracking solutions. Phys. Rev. D59, 123504.

Stubbs, C. W., Tonry, J. L., 2006. Toward 1Calibration of Astronomical Telescopes and Detectors. Astrophys. J. 646, 1436–1444.

Sunyaev, R. A., Zeldovich, Y. B., Apr. 1970. Small-Scale Fluctuations of Relic Radiation. Ap & SS7, 3–19.

Susskind, L., 2003. The anthropic landscape of string theory.

Tang, J., Abdalla, F. B., Weller, J., 2008. Complementarity of Future Dark Energy Probes.

Tegmark, M., Rees, M. J., 1998. Why is the CMB fluctuation level 10^{-5}? Astrophys. J. 499, 526–532.

Tegmark, M., et al., 2004. The 3D power spectrum of galaxies from the SDSS. Astrophys. J. 606, 702–740.

Tinker, J. L., et al., 2008. Toward a halo mass function for precision cosmology: the limits of universality. Astrophys. J. 688, 709–728.

Tinker, J. L., et al., 2010. The Large Scale Bias of Dark Matter Halos: Numerical Calibration and Model Tests. Astrophys. J. 724, 878–886.

Trotta, R., Kunz, M., Liddle, A. R., 2010. Designing Decisive Detections.

Vikhlinin, A., et al., 2009. Chandra Cluster Cosmology Project III: Cosmological Parameter Constraints. Astrophys. J. 692, 1060–1074.

Wang, L.-M., Steinhardt, P. J., 1998. Cluster Abundance Constraints on Quintessence Models. Astrophys. J. 508, 483–490.

Wang, Y., 1999. Analytical Modeling of the Weak Lensing of Standard Candles. Astrophys. J. 525, 651.

Wang, Y., 2008. Figure of Merit for Dark Energy Constraints from Current Observational Data. Phys. Rev. D77, 123525.

Wang, Y., Tegmark, M., 2005. Uncorrelated Measurements of the Cosmic Expansion History and Dark Energy from Supernovae. Phys. Rev. D71, 103513.

Weinberg, D. H., 2005. Dark Energy: The Observational Challenge. New Astron. Rev. 49, 337–345.

Weinberg, S., 1989. The cosmological constant problem. Rev. Mod. Phys. 61, 1–23.

Yoo, J., Weinberg, D. H., Tinker, J. L., Zheng, Z., Warren, M. S., 2009. Extending Recovery of the Primordial Matter Power Spectrum. Astrophys. J. 698, 967–985.

Zehavi, I., et al., 2005. The Luminosity and Color Dependence of the Galaxy Correlation Function. Astrophys. J. 630, 1–27.

Zehavi, I., et al., 2010. Galaxy Clustering in the Completed SDSS Redshift Survey: The Dependence on Color and Luminosity.